Site U1591[1]

T.H. Druitt, S. Kutterolf, T.A. Ronge, S. Beethe, A. Bernard, C. Berthod, H. Chen, S. Chiyonobu, A. Clark, S. DeBari, T.I. Fernandez Perez, R. Gertisser, C. Hübscher, R.M. Johnston, C. Jones, K.B. Joshi, G. Kletetschka, O. Koukousioura, X. Li, M. Manga, M. McCanta, I. McIntosh, A. Morris, P. Nomikou, K. Pank, A. Peccia, P.N. Polymenakou, J. Preine, M. Tominaga, A. Woodhouse, and Y. Yamamoto[2]

Contents

Keywords

International Ocean Discovery Program, IODP, R/V *JOIDES Resolution*, Expedition 398, Hellenic Arc Volcanic Field, Earth Connections, Earth in Motion, Biosphere Frontiers, Site U1591, Santorini caldera, Aegean Sea, Christiana-Santorini-Kolumbo volcanic field, subduction zone, shallow-marine volcanism

Core descriptions

Supplementary material

References (RIS)

1. Background and objectives

Prior to arrival on site, a decision was made to replace the original primary site (proposed Site CSK-13A) by an alternate site (proposed Site CSK-20A); hence, the latter became Site U1591. This was done to pass through a slightly more complete suite of reflectors in the 800–900 ms two-way traveltime (TWT) interval.

Site U1591 is located ~8 km northwest of Christiani Island and ~20 km southwest of Santorini (Figure **F1**) at 514 meters below sea level (mbsl). It was drilled in three holes (U1591A–U1591C) to a maximum recovery depth of 902.7 meters below seafloor (mbsf) (all depths below seafloor are given using the core depth below seafloor, Method A [CSF-A], scale, except in **Operations** where the drilling depth below seafloor [DSF] scale is used). Average core recovery was similar in all three holes (U1591A= 66%; U1591B= 43%; U1591C= 58%).
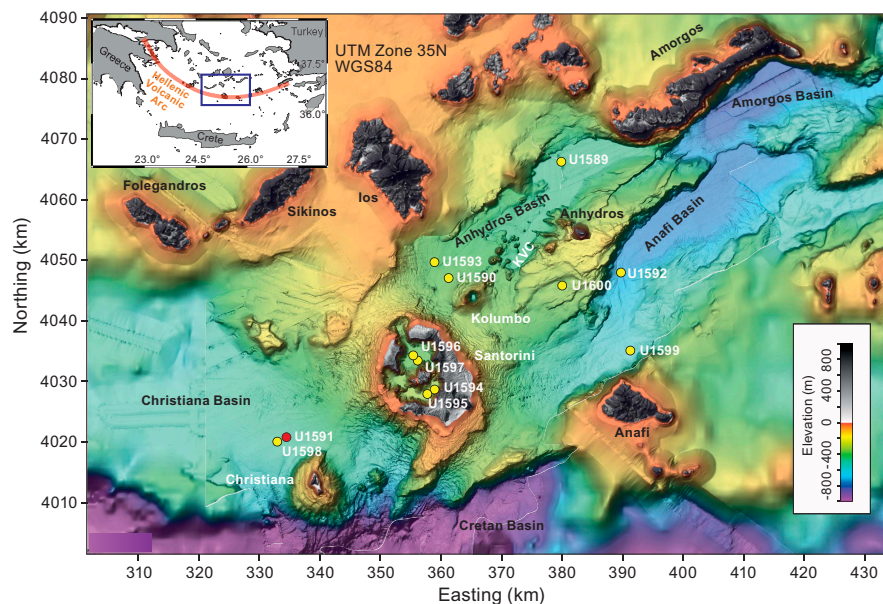

Figure F1. Site map. Red = Site U1591, yellow = other sites. Inset: location map. See Figure F1 in the Site U1589 chapter (Druitt et al., 2024) for citations for the swath data on which this map is based. KVC = Kolumbo volcanic chain.

The drill site targeted the volcano-sedimentary fill of the Christiana Basin. This basin was believed to have formed by subsidence along an ENE–WSW fault system before the changing tectonic regime activated the current northeast–southwest rift system in which the Christiana-Santorini-Kolumbo (CSK) volcanic field lies (Tsampouraki-Kraounaki and Sakellariou, 2018; Preine et al., 2022a, 2022b). Christiana Basin is deeper than the Anhydros and Anafi Basins; its volcano-sedimentary fill potentially recorded the earlier volcanic history of the CSK volcanic field (including the products of Christiana and early Santorini), as well as younger Santorini and possibly Milos Volcano to the west along the Hellenic volcanic arc. The now-extinct Christiana Volcano produced lavas and tuffs of unknown ages (Aarburg and Frechen, 1999). An ignimbrite found on Christiani Island (one of the two small islands of Christiana Volcano), Santorini, and the nonvolcanic island of Anaphi, called the Christiani Ignimbrite, was identified (Keller et al., 2010).

Six seismic units were previously recognized in the Christiana Basin (Preine et al., 2022a, 2022b; Figure **F2**). Site U1591 was chosen to pass through Seismic Units U1–U6, including volcaniclastics from Santorini and Christiana, and to target the top few meters of the prevolcanic basement below Unit U1. We received permission from the International Ocean Discovery Program (IODP) Environmental Protection and Safety Panel to drill to the Alpine basement at this site in an advanced piston corer/extended core barrel/rotary core barrel (APC/XCB/RCB) drilling strategy involving three holes.

The aims of Site U1591 were (1) to better date the volcanic activity of Christiana using biostratigraphic and magnetostratigraphic means and determine whether the CSK volcanic field had Pliocene volcanism similar to the Milos Volcano farther west; (2) to relate the Christiana volcanism to subsidence along the ENE–WSW fault sets and to the activation of the northeast–southwest fault sets; and (3) to seek the submarine equivalent of the Christiani Ignimbrite. By using deeper coring (and seismic profiles) to reconstruct the volcanic, sedimentary, and tectonic histories of the Christiana Volcano, and possibly the Milos Volcano, we aimed to complement the Santorini and Kolumbo volcanic records of Sites U1589 and U1592 and therefore access a near-continuous time series of volcanism of the CSK volcanic field since rift inception. Site U1591 addressed scientific Objectives 1–4 and 6 of the Expedition 398 Scientific Prospectus (Druitt et al., 2022).
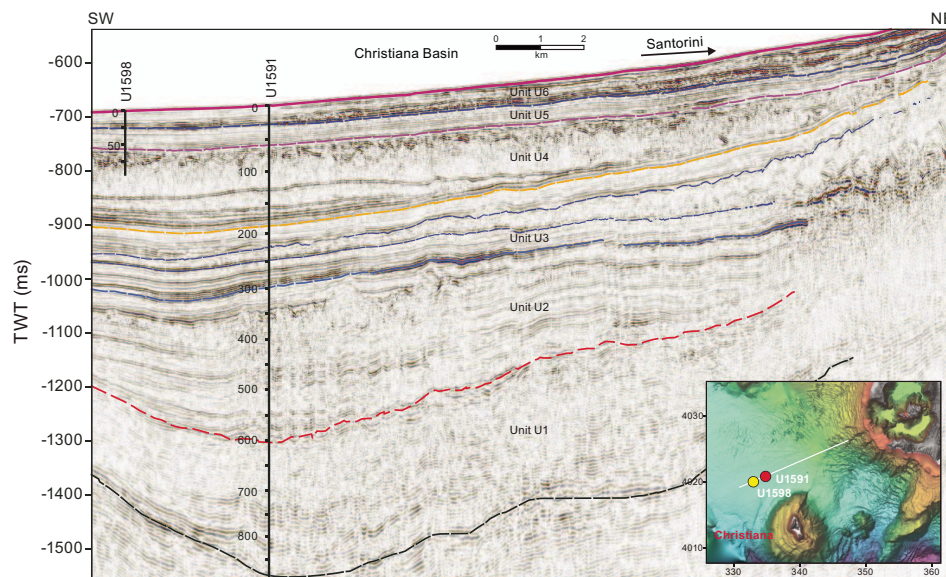
Figure F2. Seismic profile across the Christiana Basin along Seismic Line Geomar_P5008. The basin fill has six seismic stratigraphic units (U1–U6), following Preine et al. (2022b). Inset: locations of Site U1591 and Site U1598 in the same basin. Depths in meters.

2. Operations

All thrusters were down and secured on 2 January 2023 at 0006 h. The vessel was switched to dynamic positioning auto control mode at 0014 h, marking the start of Site U1591. The transit from Site U1590 took only 2.3 h, covering 20.3 nmi at 8.8 kt.

Operations involved three holes, with heavier use of the XCB and RCB systems due to the seemingly poor hole conditions when piston coring. Hole U1591A was piston cored with the APC system until the hole became unstable at Core 10H and was ended after Core 11H. Hole U1591B was piston cored to just above the trouble area, drilled down, and then primarily XCB cored. Core 43X saw the XCB shoe sheared off, ending the hole. Hole U1591C was an RCB-only hole, drilled down to 149.3 mbsf and then cored to 902.9 mbsf. The hole was terminated for time.

2.1. Hole U1591A

At 0740 h on 2 January 2023, Hole U1591A was spudded at 36°18.7615′N, 025°09.0057′E with a recovery of 3.8 m for Core 1H and a calculated seafloor at 514.6 mbsf (Table **T1**). APC coring continued through Core 11H at 98.8 mbsf.

Table T1. Core summary, Site U1591. mbsf = meters below seafloor. NA = not applicable. DSF = drilling depth below seafloor. H = APC, F = HLAPC, X = XCB, numeric core type = drilled interval, R = RCB. Times in UTC are 2 h behind the local times given in the text at the time of drilling. (Continued on next two pages.) **Download table in CSV format.**

Hole U1591A
  Latitude: 36°18.7615′N
  Longitude: 25°9.0057′E
  Water depth (m): 514.56
  Date started (UTC): 2215 h; 1 January 2023
  Date finished (UTC): 1500 h; 2 January 2023
  Time on hole (days): 0.7
  Penetration (mbsf): 98.8
  Cored interval (m): 98.8
  Recovered length (m): 64.76
  Recovery (%): 65.55
  Drilled interval (m): NA
  Drilled interval (no.): 0
  Total cores (no.): 11
  APC cores (no.): 11
  HLAPC cores (no.): 0
  XCB cored (no.): 0

Hole U1591B
  Latitude: 36°18.7621′N
  Longitude: 25°9.0190′E
  Water depth (m): 513.76
  Date started (UTC): 1500 h; 2 January 2023
  Date finished (UTC): 0745 h; 5 January 2023
  Time on hole (days): 2.7
  Penetration (mbsf): 389.2
  Cored interval (m): 364.5
  Recovered length (m): 155.08
  Recovery (%): 42.55
  Drilled interval (m): 24.7
  Drilled interval (no.): 1
  Total cores (no.): 42
  APC cores (no.): 8
  HLAPC cores (no.): 6
  XCB cored (no.): 28

Hole U1591C
  Latitude: 36°18.7810′N
  Longitude: 25°8.9962′E
  Water depth (m): 513.76
  Date started (UTC): 0745 h; 5 January 2023
  Date finished (UTC): 1445 h; 10 January 2023
  Time on hole (days): 5.29
  Penetration (mbsf): 902.9
  Cored interval (m): 668.6
  Recovered length (m): 384.47
  Recovery (%): 57.5
  Drilled interval (m): 69
  Drilled interval (no.): 2
  Total cores (no.): 122
  RCB cores (no.): 69

Core	Top depth drilled DSF (m)	Bottom depth drilled DSF (m)	Interval advanced (m)	Recovered length (m)	Core recovery (%)	Core on deck date (2023)	Core on deck time UTC (h)
398-U1591A-							
1H	0.0	3.8	3.8	3.79	100	1 Jan	0545
2H	3.8	13.3	9.5	9.71	102	1 Jan	0635
3H	13.3	22.8	9.5	8.29	87	1 Jan	0710
4H	22.8	32.3	9.5	9.60	101	1 Jan	0740
5H	32.3	41.8	9.5	9.02	95	1 Jan	0815
6H	41.8	51.3	9.5	10.04	106	1 Jan	0850
7H	51.3	60.8	9.5	6.78	71	1 Jan	0920

Table T1 (continued). (Continued on next page.)

Core	Top depth drilled DSF (m)	Bottom depth drilled DSF (m)	Interval advanced (m)	Recovered length (m)	Core recovery (%)	Core on deck date (2023)	Core on deck time UTC (h)
8H	60.8	70.3	9.5	3.46	36	1 Jan	0945
9H	70.3	79.8	9.5	2.47	26	1 Jan	1025
10H	79.8	89.3	9.5	0.05	1	1 Jan	1115
11H	89.3	98.8	9.5	1.55	16	1 Jan	1155
398-U1591B-							
1H	0.0	7.6	7.6	7.56	99	2 Jan	2000
2H	7.6	17.1	9.5	9.73	102	2 Jan	2050
3H	17.1	26.6	9.5	8.90	94	2 Jan	2125
4H	26.6	36.1	9.5	9.96	105	2 Jan	2215
5H	36.1	45.6	9.5	10.05	106	2 Jan	2245
6H	45.6	55.1	9.5	9.83	103	2 Jan	2310
7H	55.1	64.6	9.5	8.41	89	2 Jan	2350
8H	64.6	74.1	9.5	2.49	26	3 Jan	0035
91	74.1	98.8	24.7	****Drilled interval****		3 Jan	0435
10F	98.8	103.5	4.7	2.68	57	3 Jan	0510
11F	103.5	108.2	4.7	1.15	24	3 Jan	0545
12F	108.2	112.9	4.7	1.09	23	3 Jan	0625
13F	112.9	117.6	4.7	0.00	0	3 Jan	0730
14X	117.6	127.3	9.7	0.00	0	3 Jan	0920
15X	127.3	137.0	9.7	0.72	7	3 Jan	1030
16X	137.0	146.7	9.7	0.00	0	3 Jan	1130
17F	146.7	151.4	4.7	2.06	44	3 Jan	1235
18F	151.4	156.1	4.7	1.48	31	3 Jan	1320
19X	156.1	165.8	9.7	0.00	0	3 Jan	1455
20X	165.8	175.5	9.7	0.00	0	3 Jan	1615
21X	175.5	185.2	9.7	0.20	2	3 Jan	1805
22X	185.2	194.9	9.7	9.75	101	3 Jan	1955
23X	194.9	204.6	9.7	9.67	100	3 Jan	2125
24X	204.6	214.3	9.7	2.63	27	3 Jan	2245
25X	214.3	224.0	9.7	0.80	8	4 Jan	0005
26X	224.0	233.7	9.7	1.08	11	4 Jan	1015
27X	233.7	243.4	9.7	0.21	2	4 Jan	0210
28X	243.4	253.1	9.7	0.00	0	4 Jan	0340
29X	253.1	262.8	9.7	0.03	0	4 Jan	0455
30X	262.8	272.5	9.7	7.90	81	4 Jan	0620
31X	272.5	282.2	9.7	9.80	101	4 Jan	0740
32X	282.2	291.9	9.7	2.15	22	4 Jan	0925
33X	291.9	301.6	9.7	4.41	45	4 Jan	1050
34X	301.6	311.3	9.7	0.02	0	4 Jan	1215
35X	311.3	321.0	9.7	5.34	55	4 Jan	1345
36X	321.0	330.7	9.7	2.23	23	4 Jan	1640
37X	330.7	340.4	9.7	8.14	84	4 Jan	1810
38X	340.4	350.1	9.7	3.88	40	4 Jan	1935
39X	350.1	359.8	9.7	1.42	15	4 Jan	2055
40X	359.8	369.5	9.7	4.76	49	4 Jan	2210
41X	369.5	379.2	9.7	0.75	8	4 Jan	2345
42X	379.2	384.2	5.0	1.40	28	5 Jan	0130
43X	384.2	389.2	5.0	2.40	48	5 Jan	0340
398-U1591C-							
11	0.0	149.3	149.3	****Drilled interval****		5 Jan	1800
2R	149.3	158.3	9.0	0.00	0	5 Jan	1845
3R	158.3	168.0	9.7	0.43	4	5 Jan	1935
4R	168.0	177.7	9.7	0.64	7	5 Jan	2035
5R	177.7	187.4	9.7	1.73	18	5 Jan	2155
6R	187.4	197.1	9.7	4.45	46	5 Jan	2315
7R	197.1	206.8	9.7	8.29	85	6 Jan	0020
8R	206.8	216.5	9.7	5.94	61	6 Jan	0130
9R	216.5	226.2	9.7	4.51	46	6 Jan	0230
10R	226.2	235.9	9.7	0.00	0	6 Jan	0320
11R	235.9	245.6	9.7	0.51	5	6 Jan	0415
12R	245.6	255.3	9.7	5.96	61	6 Jan	0510
13R	255.3	265.0	9.7	7.74	80	6 Jan	0610
141	265.0	350.0	85.0	****Drilled interval****		6 Jan	1030
15R	350.0	359.7	9.7	1.40	14	6 Jan	1125
16R	359.7	369.4	9.7	1.07	11	6 Jan	1255
17R	369.4	379.1	9.7	1.50	15	6 Jan	1420
18R	379.1	388.8	9.7	0.16	2	6 Jan	1545
19R	388.8	398.5	9.7	3.71	38	6 Jan	1650
20R	398.5	408.2	9.7	5.74	59	6 Jan	1745

Table T1 (continued).

Core	Top depth drilled DSF (m)	Bottom depth drilled DSF (m)	Interval advanced (m)	Recovered length (m)	Core recovery (%)	Core on deck date (2023)	Core on deck time UTC (h)
21R	408.2	417.9	9.7	6.33	65	6 Jan	1855
22R	417.9	427.6	9.7	4.38	45	6 Jan	2005
23R	427.6	437.3	9.7	6.23	64	6 Jan	2115
24R	437.3	447.0	9.7	0.36	4	6 Jan	2225
25R	447.0	456.7	9.7	5.89	61	6 Jan	2345
26R	456.7	466.4	9.7	5.76	59	7 Jan	0055
27R	466.4	476.1	9.7	3.89	40	7 Jan	0205
28R	476.1	485.8	9.7	4.11	42	7 Jan	0325
29R	485.8	495.5	9.7	5.66	58	7 Jan	0435
30R	495.5	505.2	9.7	2.59	27	7 Jan	0555
31R	505.2	514.9	9.7	6.64	68	7 Jan	0815
32R	514.9	524.6	9.7	8.26	85	7 Jan	0940
33R	524.6	534.3	9.7	3.85	40	7 Jan	1105
34R	534.3	544.0	9.7	7.16	74	7 Jan	1230
35R	544.0	553.7	9.7	8.04	83	7 Jan	1340
36R	553.7	563.4	9.7	10.08	104	7 Jan	1500
37R	563.4	573.1	9.7	4.79	49	7 Jan	1620
38R	573.1	582.8	9.7	6.50	67	7 Jan	1740
39R	582.8	592.5	9.7	7.79	80	7 Jan	1905
40R	592.5	602.2	9.7	9.62	99	7 Jan	2040
41R	602.2	611.9	9.7	7.70	79	7 Jan	2205
42R	611.9	621.6	9.7	0.26	3	7 Jan	1125
43R	621.6	631.3	9.7	8.10	84	8 Jan	0055
44R	631.3	641.0	9.7	3.41	35	8 Jan	0220
45R	641.0	650.7	9.7	9.99	103	8 Jan	0345
46R	650.7	660.4	9.7	5.01	52	8 Jan	0520
47R	660.4	670.1	9.7	1.93	20	8 Jan	0645
48R	670.1	679.8	9.7	9.04	93	8 Jan	0820
49R	679.8	689.5	9.7	5.57	57	8 Jan	1000
50R	689.5	699.2	9.7	9.86	102	8 Jan	1145
51R	699.2	708.9	9.7	9.05	93	8 Jan	1325
52R	708.9	718.6	9.7	7.26	75	8 Jan	1500
53R	718.6	728.3	9.7	9.99	103	8 Jan	1620
54R	728.3	738.0	9.7	4.62	48	8 Jan	1810
55R	738.0	747.7	9.7	3.38	35	8 Jan	2015
56R	747.7	757.4	9.7	5.51	57	8 Jan	1025
57R	757.4	767.1	9.7	10.01	103	9 Jan	0025
58R	767.1	776.8	9.7	9.38	97	9 Jan	0235
59R	776.8	786.5	9.7	8.27	85	9 Jan	0415
60R	786.5	796.2	9.7	8.93	92	9 Jan	0600
61R	796.2	805.9	9.7	8.73	90	9 Jan	0725
62R	805.9	815.6	9.7	6.30	65	9 Jan	0910
63R	815.6	825.3	9.7	6.33	65	9 Jan	1145
64R	825.3	835.0	9.7	5.11	53	9 Jan	1355
65R	835.0	844.7	9.7	5.08	52	9 Jan	1630
66R	844.7	854.4	9.7	8.29	85	9 Jan	1850
67R	854.4	864.1	9.7	6.87	71	9 Jan	2110
68R	864.1	873.8	9.7	4.48	46	10 Jan	0015
69R	873.8	883.5	9.7	6.22	64	10 Jan	0400
70R	883.5	893.2	9.7	8.61	89	10 Jan	0625
71R	893.2	902.9	9.7	9.47	98	10 Jan	0845
		Totals:	1390.9	604.31			

Tight hole conditions were seen, and the decision was made to pull the bottom-hole assembly (BHA) and remove the tapered drill collar (TDC) and the nonmagnetic drill collar (NMDC), both relatively expensive compared to the rest of the BHA and also in short supply on board.

The string was pulled out of the hole with the top drive to 508 meters below rig floor (mbrf), clearing the seafloor at 1512 h. The floor crew unloaded the Icefield MI-5 core orientation tool, and the top drive was racked back. The trip out continued to 136.6 mbrf. Meanwhile, the vessel was offset 20 m east of Hole U1591A. The bit cleared the rotary table at 1700 h, ending Hole U1591A.

2.2. Hole U1591B

Still on 2 January 2023, a reconfigured APC/XCB BHA was assembled with the same drill bit. The TDC and NMDC were removed and stored in the forward collar catwalk. The trip-in started at 1945 h. Hole U1591B was spudded at 2150 h on 2 January at 36°18.7621′N, 025°09.0190′E. The recovery of 3.8 m indicated seafloor at 513.8 mbsl. APC coring continued to 3 January and Core 8H from 64.6 mbsf.

At 0245 h on the morning of 3 January, the APC system was pulled and an XCB center bit was dropped. The intention was to drill through a previously identified pumice section. The driller established slow circulation rates and proceeded to drill from 74.1 to 98.8 mbsf. The driller worked tight hole conditions at 91.3 mbsf, and a mud sweep was pumped to help alleviate the trouble.

Following the drill-down interval, the half-length advanced piston corer (HLAPC) system was deployed from Core 10F at 98.8 mbsf through Core 13F at 112.9 mbsf. Several overpulls in the range of 40,000 lb were observed. More mud was pumped.

At 0930 h, coring switched to the XCB system with Core 14X at 117.6 mbsf through Core 16X at 146.7 mbsf. However, all three XCB cores were ~0 m recovery.

The switch was again made to the HLAPC system for Core 17F from 146.7 mbsf through Core 18F from 151.4 mbsf, but higher erratic torque in the hole paused coring for several minutes. Despite the poor recovery from rotary coring, the hole was behaving better with XCB coring. With the goal for the hole being the deep target, a final switch was made back to the XCB system.

XCB coring reinitiated with Core 19X from 156.1 mbsf through Core 35X to 321.0 mbsf. The Core 36X barrel did not land (standpipe pressure did not come up). The coring line was run to retrieve the barrel, striking it early at ~187 mbsf and shearing the overshot. The sinker bars were pulled up, and the overshot was replaced. A second attempt retrieved the barrel; however, there was no evidence for why the barrel hung.

On 5 January, XCB coring finished with Core 43X at 389.2 mbsf, the final depth for Hole U1591B, after the XCB cutting shoe sheared off in hole. The reason for the failure was not clear.

A mud sweep was pumped prior to tripping. The trip continued with the bit clearing the seafloor at 0800 h. The bit cleared the rig floor at 0950 h, ending Hole U1591B.

2.3. Hole U1591C

On 5 January 2023 at 1500 h, Hole U1591C was spudded at 36°18.7810′N, 025°08.9962′E, with an offset water depth of 524.9 mbrf. A drill-ahead section was completed to 149.3 mbsf. The center bit was retrieved at 1915 h, and RCB coring began with Cores 2R–5R at 187.4 mbsf by midnight on 5 January.

On 6 January, RCB coring continued from Core 6R at 187.4 mbsf through Core 13R at 265.0 mbsf. Switching to drilling mode, the driller advanced the interval from 265.0 to 350.0 mbsf. At 1200 h, the center bit was recovered, and RCB coring was reinstated with Core 15R. Coring continued, largely uneventfully, to 10 January and Core 71R at 902.9 mbsf, the final depth for Hole U1591C. The decision was made to terminate coring in favor of other objectives. The bit cleared the rotary table at 1550 h, and the drill floor was secured for the transit. Deckhands started raising the thrusters at 1636 h. All thrusters were up and secured at 1648 h, and the sea passage to Site U1590 began, ending Site U1591.

3. Lithostratigraphy

Cores from three consecutive holes at Site U1591 (U1591A–U1591C) recovered a partial stratigraphy from 0 to 902.67 mbsf (Figure **F3**). Hole U1591A consists of Cores 1H–11H (0–90.85 mbsf), Hole U1591B includes Cores 1H–43X (0–386.57 mbsf), and Hole U1591C includes Cores 1R–71R (158.71–902.67 mbsf). We observed very good correlation between Holes U1591A and U1591B.

Recovery in Hole U1591C began at ~160 mbsf, with the goal of recovering volcanic intervals that were only poorly recovered at the bottom of Hole U1591B. In addition, Hole U1591C targets the lithology of the underlying basement.

The recovered material is sedimentary and unlithified throughout Holes U1591A and U1591B. A gradual transition to stiffer and more consolidated material toward the bottom of Hole U1591B continues in Hole U1591C. These visual observations are corroborated by increasing *P*-wave velocity and bulk density and decreasing porosity (see **Physical properties**). Sediment in Hole U1591C transitions gradually from consolidated sediment to sedimentary rock. In contrast to this gradual transition, the change in classification from sediment to sedimentary rock must occur at

Figure F3. Lithostratigraphic summary, Site U1591. * = depth and recovery affected by slumped material.

one specific interval. This boundary was made (see the Expedition 372B/375 methods chapter [Wallace et al., 2019]) where preparing smear slides became difficult and a concomitant increase in the slope of the *P*-wave velocity occurred (after Core 398-U1591C-23R). Subsequently, the lithology names changed from ash to tuff, ooze to marl, mud to mudstone, and so on.

The sedimentary succession in the uppermost 772 m is characterized by both volcanic lithologies (ash/tuff, lapilli-ash, lapilli, and tuffaceous mud/sand/mudstone/sandstone) and nonvolcanic calcareous mud/mudstone and ooze/marl. At 772 mbsf, there is a sharp transition from marls, calcareous mudstones, and micrites to nodular anhydrite-bearing lithologies (± algal mats).

Changes in relative abundances of volcanic lithologies and oozes/marls enables definition of the first two lithostratigraphic units at Site U1591. Unit I is dominated by extensive volcanic intervals with lesser overall amounts of nonvolcanic material, whereas Unit II is dominated by oozes/marls and calcareous muds/mudstones with lesser volcanic intervals (Figures **F3**, **F4**). Smear slides for microscopic analyses were prepared to confirm macroscopic descriptions of distinct lithology changes at the section level, such as identification of vitric ash particles in tuffaceous lithologies or crystals in ash layers. In Unit I, the succession of tuffaceous muds/oozes and volcanic layers defines three subunits (Ia–Ic). Unit II displays six subunits (IIa–IIf) typically defined based on relative proportions of volcanic material in the dominantly nonvolcanic unit.

The third lithostratigraphic unit (Unit III) is marked by the onset of lithologies containing anhydrite (evaporite sequence), clearly showing a distinct change in depositional environment from deep marine to shallow and terrestrial. A transition to ash- and lapilli-bearing mudstone and micrite containing anhydrite (Subunit IIIb) marks the bottom of Hole U1591C.

Figure **F3** summarizes the lithostratigraphy of Site U1591, displaying core recovery and lithostratigraphic units and subunits in Holes U1591A–U1591C. Table **T2** provides the upper and lower boundaries and biostratigraphic ages (see **Biostratigraphy**) of the lithostratigraphic units and the upper and lower boundaries of the subunits. Figure **F4** graphically presents the relative proportions of volcanic, tuffaceous, and nonvolcanic lithologies within each hole in reference to lithostratigraphic units and subunits. Figure **F5** shows the grain size distributions of the lithologies in Units I–III in more detail. Figure **F6** displays different types of core disturbances observed in Site U1591.

The following sections describe (1) the effects of core disturbance, (2) the three lithostratigraphic units and subunits, (3) correlations between Holes U1591A–U1591C, and (4) X-ray diffraction (XRD) results from Site U1591.

3.1. Core disturbance

Several types of core disturbance are observed in the sediments from Site U1591:

- Mixed sediment: grains and clasts that flow and mix in water-saturated, granular core sections, producing moderately to severely disturbed original sedimentary structures and stratigraphy (Figure **F6A**).
- Uparching: slight to moderate coring-induced shear between the sediment and core liner results in bedding uniformly dragged downward along the core margins (Figure **F6B**). In these intervals, the original lithofacies and sedimentary structures are usually slightly to severely disturbed but can still be recognized visually.
- Fall-in: coarse clast-supported intervals at the tops of many cores (Figure **F6D**). In these intervals, which may extend up to 39 cm in thickness, original lithofacies and sedimentary structures are usually destroyed.
- Brecciated: core extension disturbs the core until it becomes sheared, or, in the case of brittle failure, brecciated (Figure **F6D**). Slight brecciation produces cracks in the original lithologies, whereas moderate to severe brecciation disturbs original lithofacies and sedimentary structures more severely (Figure **F6D**), although they usually remain readily recognizable. In contrast, the contacts between intervals and stratifications in granular layers may be lost due to brecciation.

- Biscuiting: fractured disc-shaped pieces ranging from a few centimeters to more than 10 cm thick, often packed with sheared and remolded core material mixed with drill slurry, filling gaps between brittle biscuits (Figure **F6E**). The degree of biscuiting ranges from slight to severe, depending on the size of the biscuits and the proportion of biscuits to infill material.
- Sediment flowage: softer or less cohesive units are plastically mixed with harder, more cohesive units either during shaking or biscuiting or due to underpressure of a partial stroke and flow along the core liner, sometimes subsequently deposited in cracks of more consolidated sediments. Relics of squeezed sediments are visible between the liner and the sediment (Figure **F6F**).
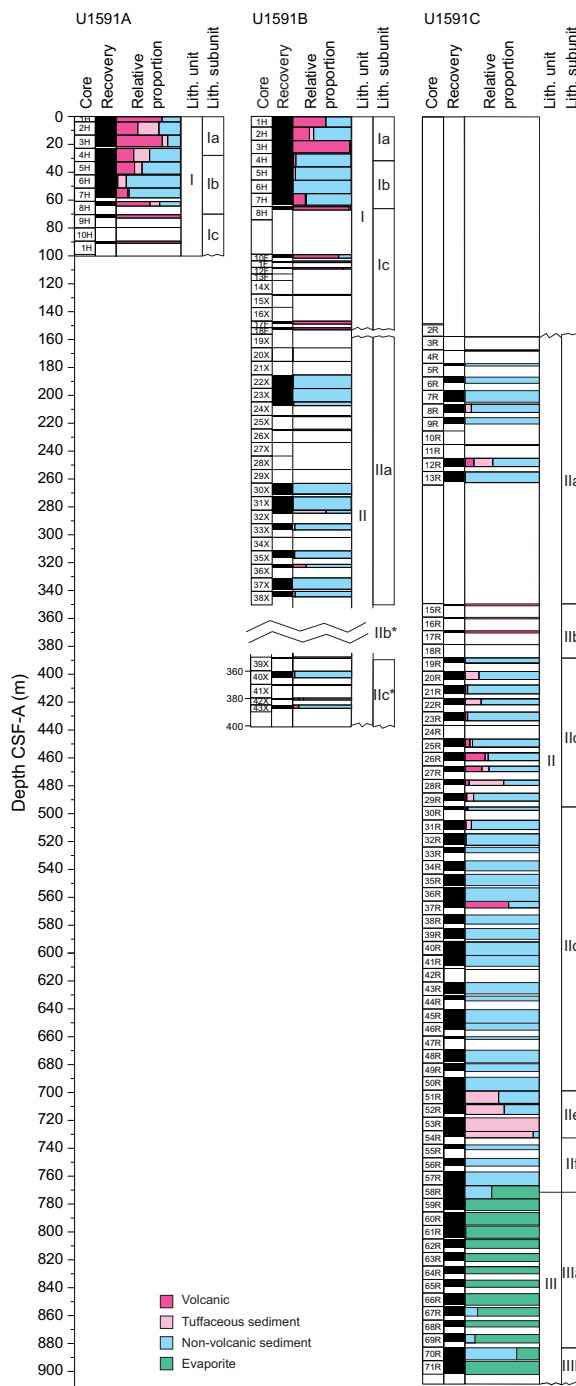
Figure F4. Relative percentages of volcanic, tuffaceous, and nonvolcanic lithologies, Site U1591. Unit I is volcanic rich compared to the nonvolcanic-dominated Unit II. Unit I subunits correspond to smaller scale variations of volcanic vs. nonvolcanic lithologies. * = depth and recovery affected by slumped material.

- Artificial size and density segregation: occurs during drilling or with postrecovery core handling processes on board (e.g., inclining, shaking, and plunging cores on the catwalk to compact sediments). Jutzeler et al. (2014) also describe pseudohorizontal density grading that can occur while the core is lying flat on deck, resulting in vertical structures once the core is turned upright. Such core disturbance is observed most often in volcanic sediments because increased porosity allows sucking in of seawater during hydraulic piston coring. The resulting soupy texture allows material to flow within the core liner. Secondary normal or reverse grading, or density separation of clasts, may occur as a result of this disturbance and obscure primary sedimentary features.

3.2. Description of units and subunits

The sediments recovered from Holes U1591A–U1591C comprise three volcano-sedimentary lithostratigraphic units (I–III) (Figure **F3**). Unit I is divided into three subunits (Ia–Ic), Unit II is divided into six subunits (IIa–IIf), and Unit III is divided into two subunits (IIIa and IIIb) (Figures **F4**, **F5**; Table **T2**). The lithology of these units and subunits is described below.

3.2.1. Unit I

Intervals: 398-U1591A-1H-1 to the bottom of the hole; 398-U1591B-1H-1 to 18F-CC, 25 cm
Thickness: 152.88 m
Depth: 0.00–152.88 mbsf
Age: Holocene to Middle Pleistocene
Lithology: volcanic and tuffaceous lithologies (ash, lapilli, lapilli-ash, and tuffaceous mud) and lesser ooze/organic-rich ooze and calcareous mud

Unit I extends from 0 to 152.88 mbsf (Table **T2**). Hole U1591A was terminated before reaching the bottom of the unit, but it was recovered in Hole U1598B. Unit I primarily consists of intercalated tuffaceous mud, ash, lapilli-ash, and lapilli punctuated by variable thickness intervals of calcareous mud and ooze (Figures **F4**, **F5**). Volcanic intervals commonly have sharp bottom contacts with tuffaceous or biogenic lithologies. Figure **F7** highlights core section images of the most common lithologies collected from Unit I. Figure **F8** shows representative smear slides from these lithologies.

Volcanic lithologies (>75% volcanic particles; glass shards, pumice, crystals) comprise ash, lapilli-ash, and lapilli. Description of these lithologies in volcanic intervals was based on the relative

Table T2. Lithostratigraphic units and subunits, Site U1591. * = top/bottom not recovered. **Download table in CSV format.**

Unit	Subunit	Top depth CSF-A (m)	Top hole, core, section, interval (cm)	Bottom depth CSF-A (m)	Bottom hole, core, section, interval (cm)	Thickness (m)	Lithologic summary
			398-		398-		
I	Ia	0.00	U1591A-1H-1, 0	27.64	U1591A-4H-4, 34	27.64	Ash, lapilli-ash, lapilli, tuffaceous mud, and ooze
		0.00	U1591B-1H-1, 0	28.75	U1591B-4H-2, 65	28.75	Ash, lapilli-ash, lapilli, tuffaceous mud, and ooze
	Ib	27.64	U1591A-4H-4, 34	62.14	U1591A-8H-1, 134	34.50	Ooze, organic-rich ooze, calcareous mud, tuffaceous mud/ooze, and ash
		28.75	U1591B-4H-2, 65	64.68	U1591B-8H-1, 8	35.93	Ooze, organic-rich ooze, calcareous mud, tuffaceous mud/ooze, and ash
	Ic	62.27	U1591A-8H-2, 0*	—	—	—	Ash, lapilli, and tuffaceous mud
		64.68	U1591B-8H-1, 10	152.88	U1591B-18F-CC, 25 *	88.20	Ash, lapilli, and tuffaceous mud
II	IIa	175.50	U1591B-21X-CC, 0*	344.25	U1591B-38X-CC, 37	168.75	Ooze, organic-rich ooze, tuffaceous ooze/sand, minor ash, and lapilli (sediments lithified from Core 23 onward)
		158.30	U1591C-3R-1, 0*	263.02	U1591C-13R-CC, 14*	104.72	Ooze, organic-rich ooze/mud, tuffaceous mud/sand, and ash
	IIb	350.10	U1591B-39X-1, 0	350.35	U1591B-39X-1, 25	0.25	Cobbles of volcanic rocks
		350.00	U1591C-15R-1, 0*	388.94	U1591C-19R-1, 14	38.94	Cobbles of volcanic rocks
	IIc	350.35	U1591B-39X-1, 25	—	—	—	Ooze, organic-rich ooze, tuffaceous mud/sand, and ash
		388.94	U1591C-19R-1, 14	491.44	U1591C-29R-4, 118	102.50	Ooze, organic-rich ooze/mud, calcareous sand, conglomerate, tuffaceous ooze/mud, ash, and lapilli
	IId	495.50	U1591C-30R-1, 0*	699.31	U1591C-50R-CC, 16*	203.81	Marl, organic-rich mudstone, tuffaceous marl, sandstone, limestone, mudstone, calcareous mudstone, and chert
	IIe	699.20	U1591C-51R-1, 0*	732.53	U1591C-54R-CC, 3	33.33	Tuffaceous mudstone, tuff, marl, and organic-rich marl
	IIf	732.53	U1591C-54R-CC, 3	772.10	U1591C-58R-4, 115	39.57	Marl, organic-rich marl, mudstone, micrite, and sandstone
III	IIIa	772.10	U1591C-58R-4, 115	879.99	U1591C-69R-CC, 21*	107.89	Micrite, anhydrite, sandstone, mudstone, and chert
	IIIb	883.50	U1591C-70R-1, 0*	902.67	U1591C-71R-CC, 30	19.17	Anhydritic mudstone and micrite with lapilli

abundance of ash-sized (<2 mm) and lapilli-sized (2–64 mm) particles, as described in **Lithostra-tigraphy** in the Expedition 398 methods chapter (Kutterolf et al., 2024), with ash and lapilli used when the proportion of one size was >75% and lapilli-ash used when both sizes were present but at <75% abundance (Fisher and Schmincke, 1984). Macroscopically, ash layers are typically white to dark gray, well sorted, range from fine ash to coarse ash, and variably admixed with mud at the top. Ash layers are typically nongraded or normally graded and are frequently characterized by a sharp base and a more diffuse and often bioturbated upper boundary that grades into tuffaceous mud. Microscopically, ash layers are characterized by colorless angular glass shards with or without crystals. Transparent pumiceous glass shards are also observed. An ash layer in the uppermost section of core (398-U1591B-8H-1, ~32 cm) contains a high abundance of pumiceous glass with tubular and rounded vesicles. A lower abundance of tubular vesicles in pumiceous glass was also observed in Sections 2H-2, 50 cm, and 8H-2, 64 cm. Some ash layers have distinct crystal/lithic-rich lags at their bases. Microscopic observations of smear slides were useful for identification of
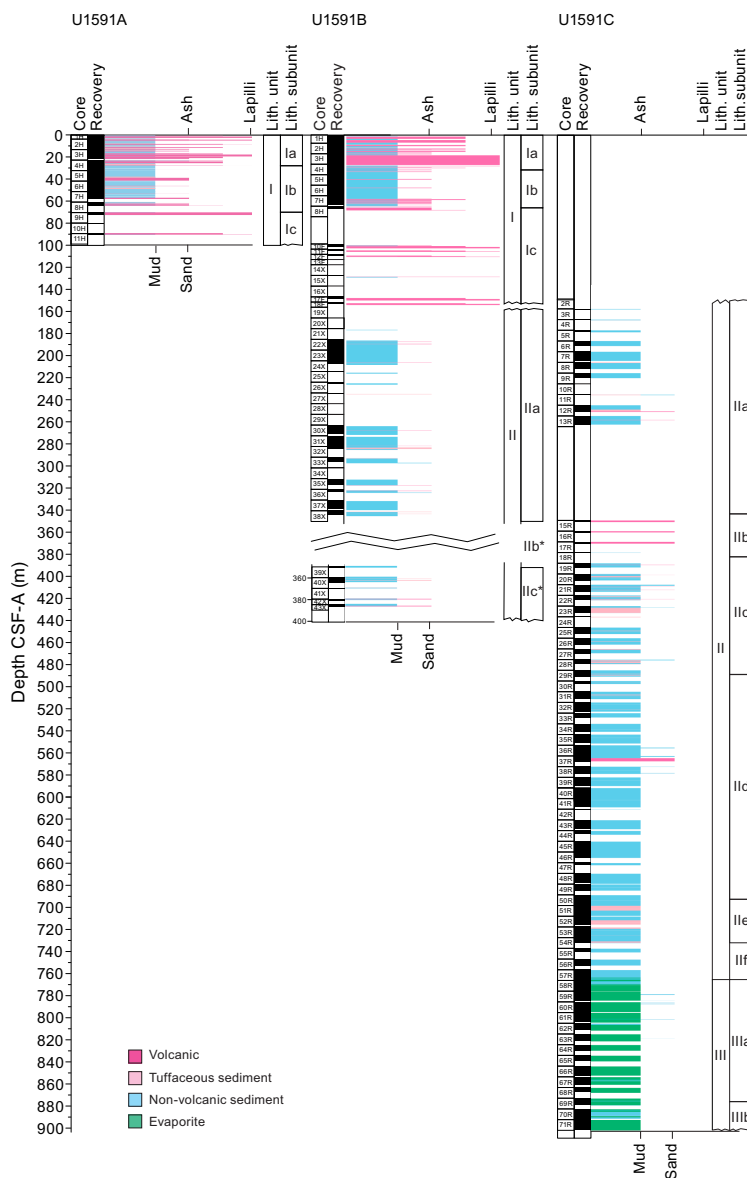
Figure F5. Average grain size distribution of volcanics, Site U1591. Length of colored bars = relative grain sizes (ash = <2 mm; lapilli = 2–64 mm; mud = <63 µm; sand = 0.063–2 mm), with separate scales shown for volcanic grain size (top) and tuffaceous and nonvolcanic sediments (bottom). Mixed lithologies such as lapilli-ash that have relative grain sizes between two categories are plotted between ticks. Evaporites (green) are not characterized by grain size. * = depth and recovery affected by slumped material.

specific minerals (e.g., biotite, feldspar, and pyroxene) in ash. The coarser volcanic intervals in Unit I range from monomictic lapilli and lapilli-ash containing white to gray pumice lapilli with varying proportions of ash matrix to polymictic lithic-vitric lapilli and lapilli-ash (Figure **F7**). Less common are lithic-rich lapilli-ash layers. Where recovered, bottom contacts of these coarser units are sharp or bioturbated but commonly affected by uparching drilling disturbance.

Subunits in Unit I were defined by the relative proportion of volcanic/tuffaceous intervals and nonvolcanic intervals:

- Subunit Ia (Sections 398-U1591A-1H-1 through 4H-4, 34 cm [0–27.64 mbsf], and 398-U1591B-1H-1 through 4H-2, 65 cm [0–28.75 mbsf]): primarily ash, lapilli, and lapilli-ash. Other components include tuffaceous mud and ooze with intermittent inclusions of ash and lapilli.
- Subunit Ib (Sections 398-U1591A-4H-4, 34 cm, through 8H-1, 134 cm [27.64–62.14 mbsf], and 398-U1591B-4H-2, 65 cm, through 8H-1, 8 cm [28.75–64.68 mbsf]): primarily nonvolcanic material consisting of ooze, organic-rich ooze, and calcareous mud, punctuated by tuffaceous mud/ooze and ash, with one expansive ash layer in Hole U1591A at 37.67–41.29 mbsf (only present at 38.78–39.19 mbsf in Hole U1591B).
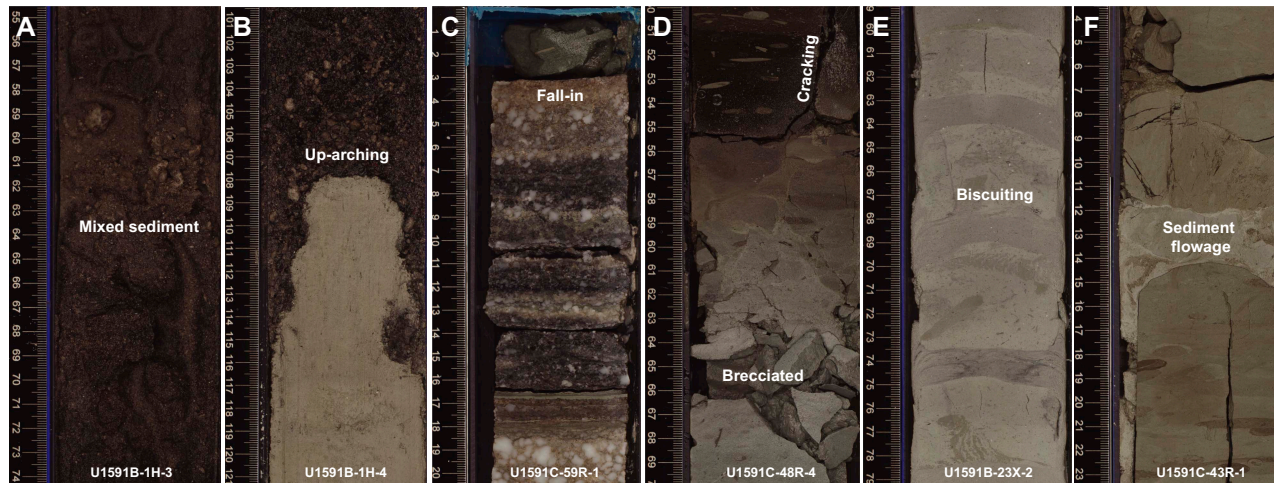
Figure F6. Core disturbances, Site U1591. A. Mixed sediments. B. Uparching. C. Fall-in. D. Cracking and brecciated core. E. Biscuiting. F. Sediment flowage.
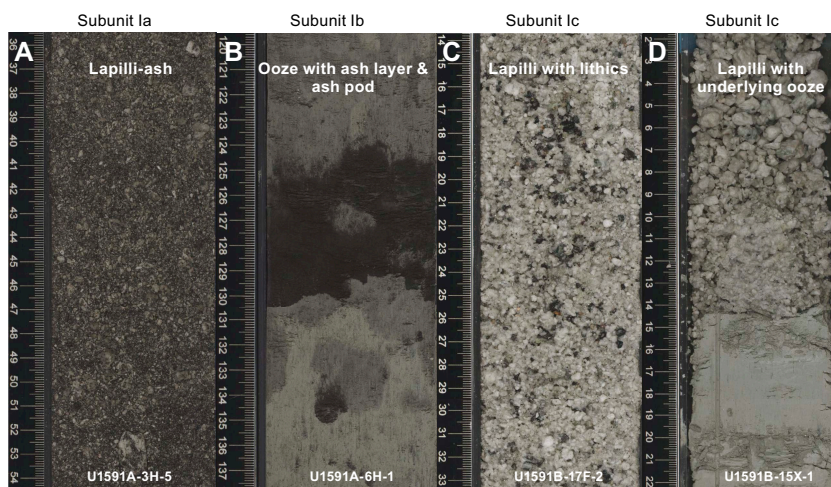
Figure F7. Representative volcanic lithologies from Unit I, Holes U1591A and U1591B. A. Ash layers. B. Ooze with ash. C, D. Lapilli layers. The ooze in D separates two large lapilli packages as shown in Hole U1591B in Figure F3.

- Subunit Ic (Sections 398-U1591A-8H-2 [62.27 mbsf to the bottom of the hole] and 398-U1591B-8H-1, 10 cm, through 18F-CC, 25 cm [64.68–152.88 mbsf]): ash, lapilli, and a layer of tuffaceous mud.

3.2.1.1. Subunit Ia

Subunit Ia extends from 0 to ~27.6 mbsf (Sections 398-U1591A-1H-1 through 4H-4, 34 cm, and 398-U1591B-1H-1 through 4H-2, 65 cm) (Table **T2**) and is dominated by volcanic-rich lithologies with sparse intercalations of fine-grained muds or oozes. Thicknesses of the volcanic intervals vary from 0.2 to ~9 m. The uppermost 32 cm consists of well-sorted yellowish brown mud that overlies a thick package (2 m) of gray to dark gray lapilli-ash, ash, and lapilli in Hole U1591A (Figure **F7A, F7B**). Pumice encountered in the aforementioned sequence is subrounded, and echinoid spines were identified in the ash layer between 0.98 and 1.01 mbsf (Section 398-U1591A-1H-1). Below this volcanic package (2.24–2.95 mbsf), a light brownish gray to very dark gray ooze and organic-rich ooze contains subrounded pumice and ash (Figure **F7C**). The second volcanic package begins at 3 mbsf in both Holes U1591A and U1591B. Gray to black tuffaceous mud, dark gray to brown ash with lapilli, and dark gray to brown lapilli were encountered between 3.00 and 4.83 mbsf in Hole U1591A and between 3.38 and 5.67 mbsf in Hole U1591B. This dark volcanic material transitions sharply downward into gray to black ooze with ash, ash with nannofossils, and ooze. The lowermost volcanic-dominated package occurs between 7.26 and 27.64 mbsf; olive-gray to very dark grayish brown tuffaceous ooze, gray to black tuffaceous mud, gray to black ash, gray to black lapilli (both pumice and scoria; Core 398-U1591A-4H), and lapilli-ash layers dominate the lithology. Light gray to dark gray ooze (some with ash) are interbedded as minor constituents (Figure **F7D**).

3.2.1.2. Subunit Ib

Subunit Ib extends from 27.64 to 62.14 mbsf in Hole U1591A and 28.75 to 64.68 mbsf in Hole U1591B (Sections 398-U1591A-4H-4, 34 cm, through 8H-1, 134 cm, and 398-U1591B-4H-2, 65 cm, through 8H-1, 8 cm). It begins with the first thick package of ooze that occurs after the last lapilli unit in Subunit Ia. This subunit consists of a package of light greenish gray to olive-gray ooze intercalated with light brownish gray to very dark gray organic-rich (sapropelic) ooze, punctuated by several thin (<10 cm) ash layers overlain by associated tuffaceous oozes. Some of the oozes have ash pods and shell fragments. In the middle of Subunit Ib (37.67 mbsf in Hole U1591A) is one extensive 3.62 m thick tuffaceous and volcanic deposit (only 41 cm thick in Hole U1591B) of light brownish gray tuffaceous ooze and lithic-crystal ash with lapilli. The bottom of Subunit Ib is ooze
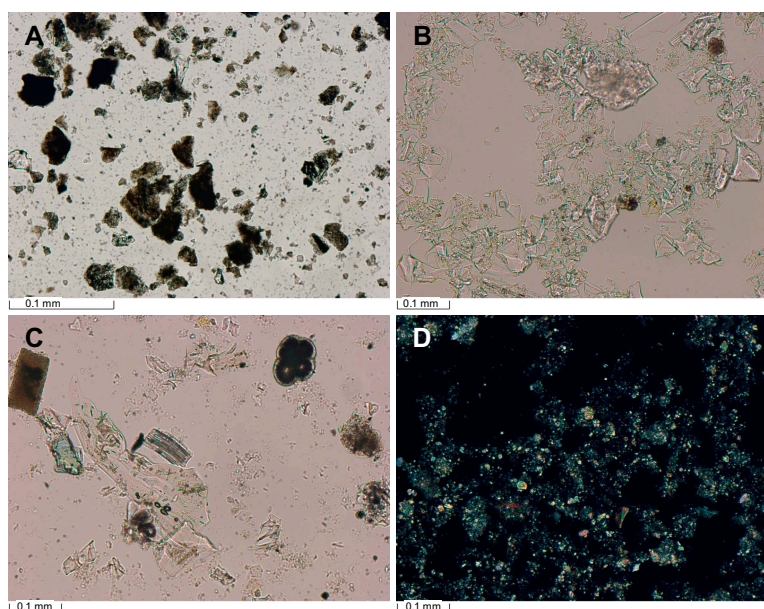
Figure F8. Ooze, Hole U1591A. A. Ooze layer (3H-2). B. Ooze with mud (2H-2). C. Ooze with ash (8H-1). D. Tuffaceous mud (8H-2).

rich but displays increasing frequency of tuffaceous ooze (some organic rich) and ash toward the bottom of the subunit.

3.2.1.3. Subunit Ic

Subunit Ic is a coarse volcanic subunit that begins beneath the last ooze interval in Subunit Ib. It extends in Hole U1591A from 62.27 mbsf to the bottom of the hole at 90.85 mbsf and in Hole U1591B from 64.68 to 152.88 mbsf. Recovery was poor, and coring in the uppermost part of Hole U1591C was unable to recover any of the volcanic material. This subunit begins with light gray ash (some with lapilli) and tuffaceous mud for 1.75 m, followed by a ~100 m thick package of light greenish gray lapilli-ash and lapilli. A thin section of the lapilli at 72.4 mbsf (interval 398-U1591A-9H-2, 70–73 cm) is highly vesicular and contains phenocrysts of plagioclase, clinopyroxene, and Fe-Ti oxides (Figure **F9**).

3.2.2. Unit II

> Intervals: 398-U1591B-21H-CC, 0 cm, to the bottom of the hole; 398-U1591C-3R-1, 0 cm, to 58R-4, 115 cm
> Thickness: 613.80 m
> Depths: Hole U1591B = 175.5–386.60 mbsf (bottom of the hole); Hole U1591C = 158.3–772.10 mbsf
> Age: Middle Pleistocene to Late Miocene (?) (see **Biostratigraphy**)
> Lithology: repeating packages of ooze/mud and organic-rich (sapropelic) ooze/mud with interspersed tuffaceous mud/sand, ash and lapilli-ash, and volcanic-dominated packages

Unit II (Figure **F3**; Table **T2**) was recovered in Holes U1591B and U1591C and is an extensive succession (613.8 m) of cyclic repetitions of ooze/mud and organic-rich (sapropelic) oozes and muds (Figure **F10A**) with minor ash and tuffaceous mud/sand. These successions are punctuated by thicker volcanic-dominated intervals. These thicker volcanic intervals, as well as the accompanying magnetic susceptibility (MS) and natural gamma radiation (NGR) data, are the basis for delineating subunits in Unit II (Table **T2**; see **Physical properties**). The top of Unit II does not begin at the same depth in Holes U1591B and U1591C because of poor recovery of the lowermost pumice-rich interval in Unit I. Hole U1591C began coring where recovery of the pumice was poorest in Hole U1591B but failed to recover it and instead retrieved material from Unit II. Thus, the actual top depth of Unit II is unconstrained.

Organic-rich intervals are oozes and calcareous muds that are typically dark greenish brown to gray. They stand out in contrast to the light greenish gray oozes (Figure **F10A**). The repetitions of oozes and organic-rich oozes/muds show regular periodicity over the span of multiple cores, but the thickness of the organic-rich intervals gradually increases and decreases over the span of 10 or more cores (Figure **F11**). On average, organic-rich intervals are 2–30 cm thick and repeat every 80–120 cm with rare breaks of up to 7 m. Their bottom contacts with oozes are typically horizontal and sharp, but the top contact shows a gradual change in color upward from dark greenish gray to light greenish gray to the sharp bottom contact of the next organic-rich interval (Figure **F10A**). The upper contacts of the organic-rich intervals are typically diffuse and gradational and marked
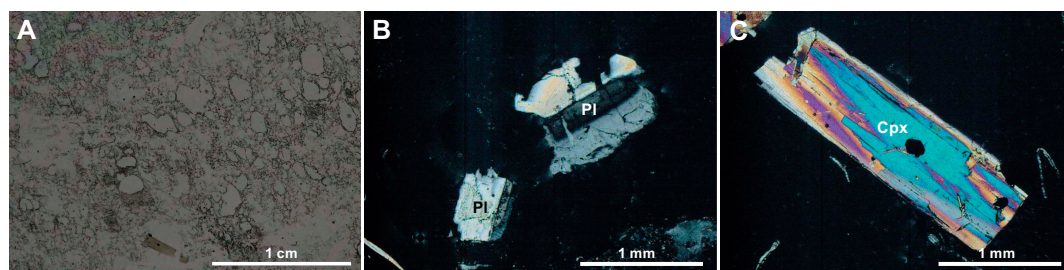
Figure F9. Light-colored, highly vesicular, porphyritic pumice from Unit I, Hole U1591A (9H-2, 70–73 cm). A. Vesicle-rich and crystal-poor nature of the pumice (plane-polarized light [PPL]). Phenocrysts of (B) plagioclase (Pl) and (C) clinopyroxene (Cpx), which occur together with Fe-Ti oxide (cross-polarized light [XPL]). Rare apatite occurs as inclusions in pyroxene. The glassy groundmass shows patchy alteration.

by high bioturbation, often as *Chondrites* traces (Figure **F12A**). Some organic-rich intervals show well-preserved *Zoophycos* traces (Figure **F12A**) and disseminated sulfides. The darkest colored organic-rich intervals are commonly thinly laminated. Within these ooze/mud intervals are intermittent volcanic (ash and lapilli-ash) and mixed sediments (tuffaceous mud/sand).

The two volcanic-dominated intervals that punctuate the ooze/mud-dominated intervals consist of a volcanic cobble unit and a tuffaceous mud (see **Subunit IIb** and **Subunit IIe**).

3.2.2.1. Subunit IIa

Subunit IIa was partially recovered in Holes U1591B and U1591C (Table **T2**) and is 104.72 m thick. The boundary between the bottom of Unit I and the top of Unit II (Subunit IIa) was not recovered. There is a gap in recovery in Hole U1591B from 152.8 to 175.5 mbsf (Cores 19X–21X), and Hole U1591C begins at 158.3 mbsf (Core 3R). The first core (3R) is assigned to this subunit instead of Unit I because of its lithology (nonvolcanic) and lower MS compared to the lower part of Unit I in Hole U1591B.

Subunit IIa consists dominantly of nonvolcanic material; slight to moderately bioturbated ooze/mud and their organic-rich equivalents; and sparse volcanic intervals of tuffaceous sand and mud, ash, and ash with lapilli. Very thin (centimeter scale) ash layers are present throughout.

Very little to no recovery occurred between Cores 398-U1591B-25X and 29X (214.9–262.8 mbsf). However, this section was partially recovered in Hole U1591C with a gap between 220.9 and 235.9 mbsf (Cores 10R and 11R). In Core 398-U1591B-27X (233.7 mbsf), 18 cm of gravelly tuffaceous sand was recovered (Figure **F12B**), and the same lithology was recovered in Core 398-U1591C-11R (236 mbsf). The poor recovery around this depth is likely caused by a coarse lithology that does not core well. Another large gap in recovery is present in Hole U1591C at 263.1–350 mbsf; however, this section was partially recovered in Hole U1591B (Figure **F3**).

The overall MS of this subunit is low, increasing in the intervals that contain volcanic material. The darkest colored organic-rich oozes and muds show higher NGR compared to the surrounding oozes and muds with lower organic content. Because of the cyclic nature of these lithologies, NGR fluctuates throughout the subunit (see **Physical properties**).
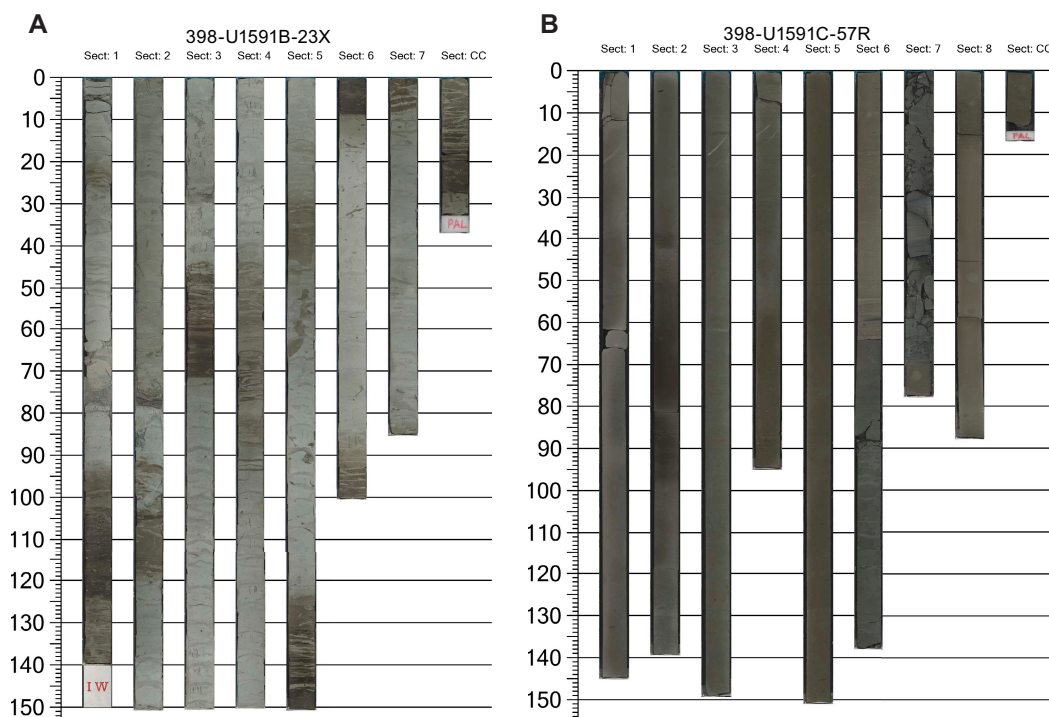
Figure F10. Core composites, Holes U1591B and U1591C. A. Cyclic intervals of ooze and organic-rich ooze (sapropelic ooze). B. Small proportion of organic-rich lithologies.

3.2.2.2. Subunit IIb

Subunit IIb is thin (38.94 m) and comprises mainly cobble-sized volcanic rocks with small intervals of lithic-crystal ash showing slump features (Figure **F12C**). This subunit was only sparsely sampled between 350 and 388.94 mbsf in Hole U1591C (Cores 15R–19R), but recovery was poorer in Hole U1591B, where only 24 cm of the subunit was sampled, part of which is fall-in (Section 39X-1; 350.10–350.35 mbsf). In Hole U1591C, the base of this subunit is defined at the base of cobble fall-in (Section 15R-1). Consequently, the top and base of this subunit are not well defined. The conflicting thickness of this subunit across Holes U1591B and U1591C, resulting in a depth offset across holes, can be attributed to a slump feature (see **Stratigraphic correlation**).
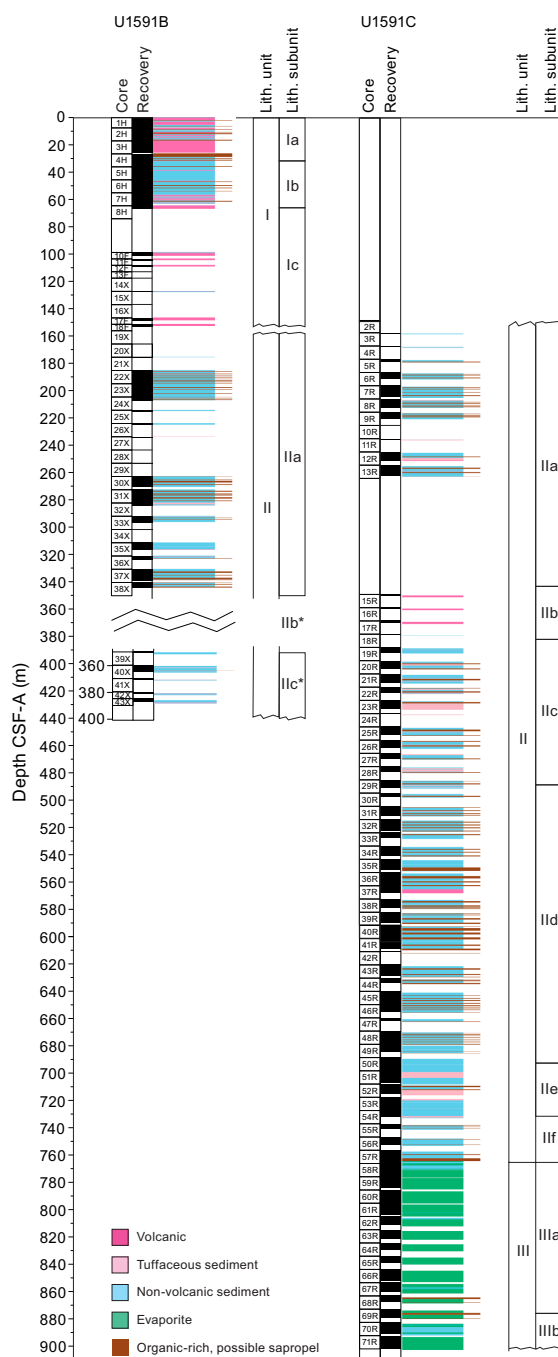
Figure F11. Organic-rich, sapropelic lithologies (extended brown lines), with background lithologies, Holes U1591B and U1591C. Confirmation of sapropelic units requires geochemical analysis of TOC content (see Geochemistry). Gaps in lithologies indicate gaps in recovery, as shown in Figure F3. * = depth and recovery affected by slumped material.

The cobbles in this subunit range from light gray to very dark grayish brown and are a mix of glassy, porphyritic, and red (oxidized) volcanic rocks. In general, several cobbles of the same type exist sequentially within core sections (i.e., four porphyritic cobbles are followed by two glassy cobbles, etc.). The matrix between cobbles is present only intermittently but is typically light gray lithic-crystal ash (Figure **F12C**). High MS is observed across this subunit in both holes.

A thin section of one of the volcanic cobbles from Core 398-U1591C-17X shows a highly porphyritic and glomeroporphyritic texture with phenocrysts of plagioclase, amphibole, clinopyroxene, and Fe-Ti oxides (Figure **F13A–F13D**).

3.2.2.3. Subunit IIc
Subunit IIc was partially recovered in Hole U1591B (350.35 mbsf to the bottom of the hole) and fully recovered in Hole U1591C (388.94–491.44 mbsf). As discussed in **Subunit IIb**, the offset in depths between Holes U1591B and U1591C is caused by variable thickness of a slump deposit. The total thickness of this subunit is 102.5 m. The upper boundary is not well defined in Holes U1591B or U1591C. In Hole U1591B, it is irregular and moderately disturbed by biscuiting (~20 cm), and in Hole U1591C the contact between it and Subunit IIb above was not recovered (see **Subunit IIb**). Subunit IIc is characterized by a moderately high frequency of volcanic lithologies within an ooze-dominated background in comparison with Subunits IIa, IId, and IIf. Lithologies present in Subunit IIc include oozes and their lithified equivalent (marl), ash (variably lithified to tuff and sometimes lithic- or crystal-rich), tuffaceous, and organic-rich sediments.

Most volcanic lithologies in Subunit IIc occur as centimeter-thick dark gray to light greenish gray ash or tuff layers interbedded with slight to moderately bioturbated ooze/marls or tuffaceous sediments (Figure **F12D**). Pumice clasts were identified within several volcanic intervals and are commonly rounded to subrounded and white/gray. One instance of biotite-bearing tuff was identified via smear slide in interval 398-U1591C-28R-1, 54–65 cm. The highest abundance of volcanic-rich sediments occurs between Cores 25R and 27R. Volcanic lithologies identified in Subunit IIc show a moderate increase in MS, which is anticorrelated with NGR (see **Physical properties**).

A thin section of a gravelly sandstone from Core 398-U1591C-28R is characterized by abundant volcanic lithics, typically plagioclase- and pyroxene-bearing scoria, grains of plagioclase, benthic foraminifera, and other bioclasts.

3.2.2.4. Subunit IId
Subunit IId was observed only in Hole U1591C and extends from 495.5 to 699.31 mbsf (Sections 30R-1, 0 cm, through 50R-CC, 16 cm) (Table **T2**). The upper boundary with Subunit IIc was clearly identified based on a sharp decrease in MS (see **Physical properties**), signifying the observed decrease in ash-bearing lithologies. Subunit IId consists of highly bioturbated marl,
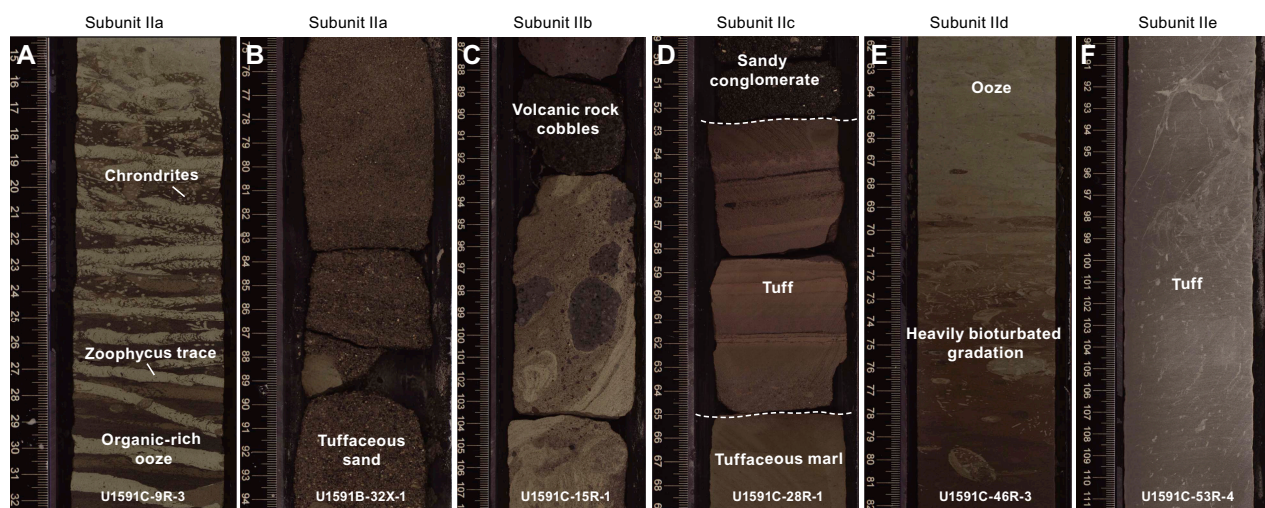
Figure F12. Representative lithologies from Unit II, Holes U1591B and U1591C. A, E. Cyclic repetitions of ooze/mud. B, D, F. Organic-rich (sapropelic) oozes/marl and muds/mudstone with minor ash and tuffaceous mud/sand. C. Sections in Subunit IIb contain volcanic rock cobbles.

mudstone, and calcareous mudstone intercalated with organic-rich marl, mudstone, and calcareous mudstone. Organic-rich intervals are commonly thinly laminated and show well-preserved *Zoophycos* and *Chondrites* traces (Figure **F12E**) and disseminated sulfides. Marl, mudstone, and calcareous mudstone have shell fragments, disseminated sulfides, and nodules of pyrite. A 2.08 m thick ash layer is observed between 566.06 and 568.14 mbsf (interval 37R-2, 135 cm, to 37R-CC, 11 cm). The middle part of the subunit (558.77–634.69 mbsf) is characterized by thicker organic-rich intervals (Sections 36R-6 through 44R-3). Marl layers in between also seem to be darker and more olive-colored than the marls above and below this interval. Below 568.14 mbsf, the organic-rich intervals become thinner (<50 cm) until they disappear; the two lowermost sections of the subunit, Cores 49R and 50R (679.8–699.36 mbsf), only contain two organic-rich calcareous mudstones <10 cm thick. Marl and mudstone between these thin organic-rich intervals are slightly bioturbated and contain plant and shell fragments and some nodules/veins of pyrite.

3.2.2.5. Subunit IIe

Subunit IIe is characterized by intermittent tuff, tuffaceous mudstone, and marl/mudstone. The recovered lithologies extend from 699.2 to 732.53 mbsf (Sections 398-U1591C-51R-1, 0 cm, through 54R-CC, 3 cm) (Table **T2**). The number of organic-rich intervals is very low in this subunit (Figure **F10B**). Only three layers of organic-rich marl (92.5, 18, and 10 cm thick) were identified between 709.25 and 712.27 mbsf (Sections 52R-1 through 52R-3). In the uppermost part of the subunit, marl is moderately sorted and contains shell fragments, organic-rich pods, and nodules of pyrite. The lower section, below 712 mbsf, consists mainly of well-sorted and fine-grained tuffaceous mudstone and tuff (Figure **F12F**). Some tuffaceous mudstones are thinly laminated (<0.3 cm). Unusually, the presence of volcanic material correlates with low MS (see **Physical properties**).

3.2.2.6. Subunit IIf

Subunit IIf extends from 732.53 to 772.1 mbsf (Sections 398-U1591C-54R-CC, 3 cm, through 58R-4, 115 cm) (Table **T2**). The uppermost part of the subunit consists of intercalated marl and organic-rich marl characterized by gradational boundaries. The thickness of the organic-rich intervals increases downcore from ~20 cm in the upper part of this subunit to ~1.5 m in the lower part. Some micrite with foraminifera, lapilli, or tuff were observed between 764.32 and 767.39 mbsf. These micritic intervals are moderately sorted and display normal grading. The lower part
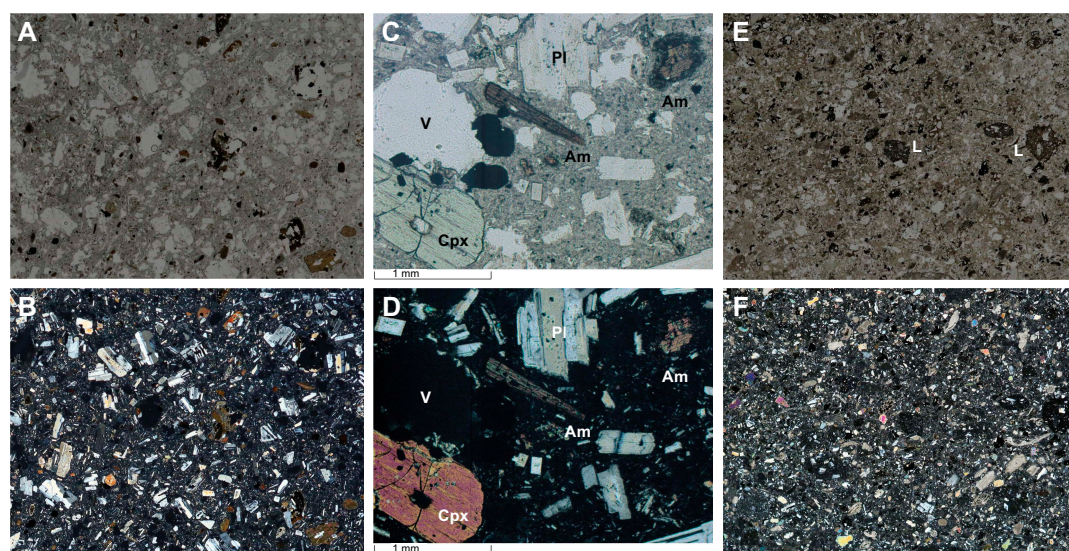
Figure F13. Cobbles in Subunit IIb and sandstone in Subunit IIc, Hole U1591C. A, B. Porphyritic extrusive volcanic rock (17R-1, 49–52 cm). (A) PPL; (B) XPL. C, D. Phenocrysts of plagioclase (Pl), amphibole (Am), clinopyroxene (Cpx), and vesicles (V) in the same sample. (C) PPL; (D) XPL. Other phenocrysts in the sample include orthopyroxene (hypersthene), the dominant pyroxene type, and Fe-Ti oxide (Ti-magnetite). Accessory apatite occurs as inclusions in other phases. Glomerocrysts consist of plagioclase, amphibole, and pyroxene. E, F. Immature sandstone (28R-1, 46–48 cm) with abundant grains of plagioclase, benthic foraminifera, and other bioclasts as well as volcanic lithics (L), typically scoria. (E) PPL; (F) XPL.

of the subunit consists of thinly laminated calcareous mudstone and sandstone. These intervals are moderately to poorly sorted and contain lithic clasts and carbonate.

3.2.3. Unit III

Interval: 398-U1591C-58R-4, 115 cm, to 71R-CC, 30 cm (bottom of the hole)
Thickness: 130.57 m
Depth: 772.1–902.67 mbsf
Age: probable Miocene
Lithology: anhydrite; alternating micrites with sandstone, mudstone, and evaporites; chert; and micrite with lapilli

Unit III was recovered only in Hole U1591C (Figures **F14**, **F15**; Table **T2**) and begins with the appearance of evaporitic lithologies that extend to the bottom of the hole. The appearance of anhydrite in Section 58R-4, 115 cm, coincides with an increase in bulk density and was confirmed as anhydrite by XRD analysis (see **Physical properties** and **X-ray diffraction**) (Figure **F14**). The unit is dominated by white to dark gray nodular and laminated anhydrite deposits interbedded with micrite (Figure **F14A**). Minor sandstone and mudstone lithologies are present, often with a micritic or anhydritic component. Intervals of nodular anhydrite commonly occur as small growths between micrite intervals (~10 mm nodules; Figure **F14A**), with a few extensive intervals of almost pure anhydrite separated by thin veinlets of micrite (Figure **F14B**). The presence of micrite was confirmed with smear slides or an HCl test. Organic-rich lithologies also appear in Unit III, occurring in thinly laminated black to reddish black muds, mudstone, and micrite.

Subunits in Unit III were designated based on the relative proportion of evaporitic deposits, as well as the appearance of lapilli near the bottom of Hole U1591C:

- Subunit IIIa (Sections 398-U1591C-58R-4, 115 cm, through 69R-CC, 21 cm; 772.1–879.99 mbsf): primarily evaporitic lithologies of alternating laminated to nodular anhydrite and micrite, with minor anhydritic mud/sandstones/breccias, organic-rich micrite, and organic-rich mud.
- Subunit IIIb (Sections 398-U1591C-70R-1, 0 cm, through 71R-CC, 30 cm; 883.5–902.67 mbsf): anhydritic mudstone, micrite, and anhydrite with variable presence of gypsum and lapilli clasts.
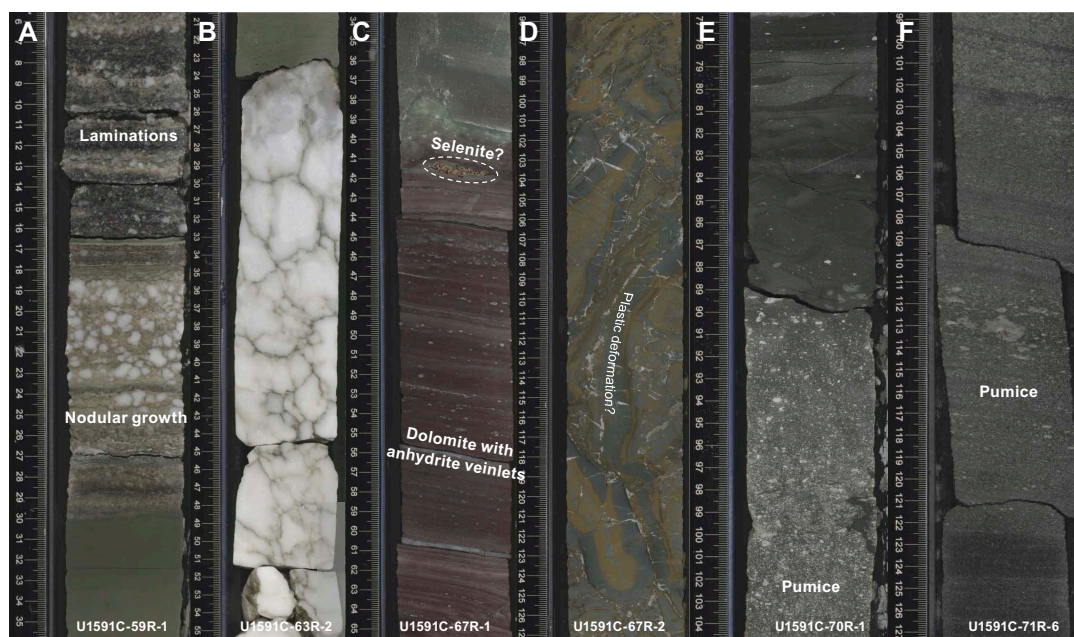

Figure F14. Representative lithologies from Unit III, Hole U1591C. A, B. Laminated and nodular anhydrite. C. Dolomite with anhydrite veinlets. D. Anhydrite with evidence of plastic deformation and secondary mineralization. E, F. Pumice lapilli within anhydritic mudstone and micrite. A–D: Subunit IIIa; E–F: Subunit IIIb.

3.2.3.1. Subunit IIIa

Subunit IIIa consists almost entirely of evaporitic lithologies (e.g., nodular anhydrite) with minor micritic/anhydritic sediments. Volcanic deposits, including pumice clasts, were identified occasionally. This subunit is ~108 m thick, extending from the top of Unit III to ~883 mbsf. The top boundary marks the start of anhydrite-dominated lithologies, transitioning from a dark greenish gray micrite to a thickly laminated, dark gray anhydritic micrite (Section 398-U1591C-58R-4, 115 cm). The subunit consists majorly of alternating anhydrite (laminated or nodular; Figure **F14A**) and micrite or micritic sediments. Laminated anhydrite sequences alternate between white and dark gray with wavy bedding ranging 0.3–10 cm in thickness. These laminations often have a crinkly texture with small anhydrite nodules separated by thin layers of micrite or mud. Micrite, mud, and sandstone are predominantly greenish gray to olive; however, between ~802 and 812.2 mbsf (interval 61R-5, 27 cm, to 62R-5, 111 cm) and 845.48–855.93 mbsf (interval 66R-1, 78 cm, to 67R-2, 15 cm), the color of the predominantly evaporitic lithologies changes to brownish red with fewer anhydritic nodules and more anhydrite-filled veins (Figure **F14C**). Between 817.2 and 817.83 mbsf (Section 63R-2, 24 cm), the most continuous interval of massive anhydrite was recovered (Figure **F14B**). Intervals dominated by dolomite also occur (e.g., Core 67R), as identified by XRD (see **X-ray diffraction**). A few intervals show signs of plastic deformation and potential alteration (Figure **F14D**).

Thin sections of four samples from Subunit IIIa show crystal-rich, quartz-feldspar-biotite bearing sandstone with laminated algal mats (Figure **F15A**), feldspar-bearing sandstone with fine-grained anhydrite nodules (Figure **F15B**), laminated anhydrite alternating with micrite (Figure **F15C**), and another laminated anhydrite alternating with algal mats and micrite (Figure **F15D**).
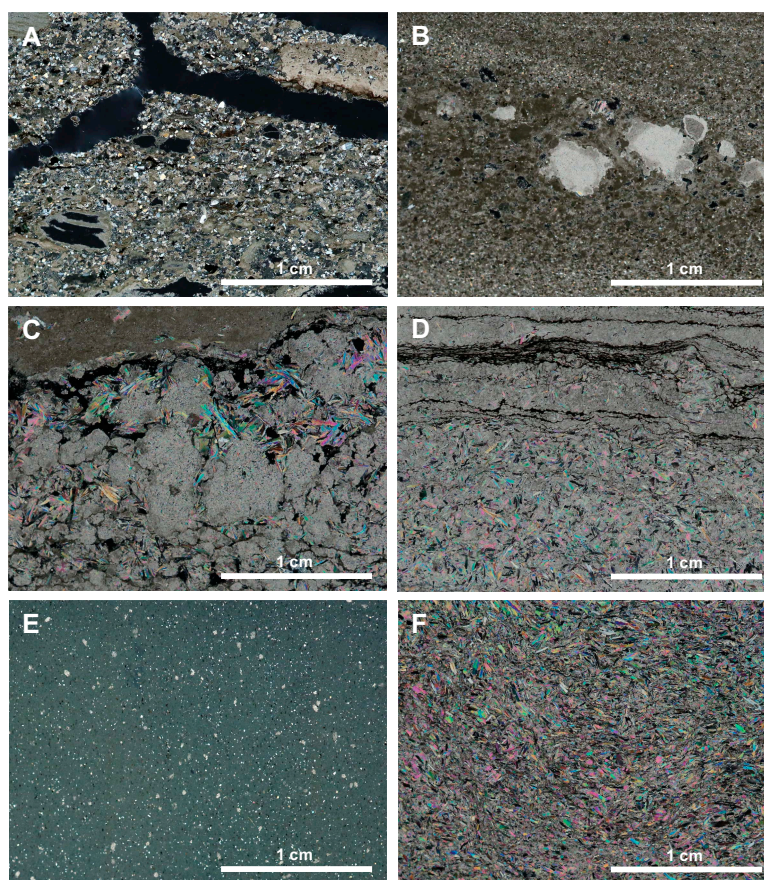
Figure F15. Evaporite lithologies from Unit III (XPL), Hole U1591C. A. Sandstone (58R-2, 6–9 cm). B. Sandstone with anhydrite nodules (58R-5, 63–66 cm). C. Laminated anhydrite alternating with micrite (58R-5, 115–118 cm). D. Laminated anhydrite alternating with algal mats and micrite (69R-1, 15–18 cm). E. Fine-grained anhydritic mudstone with crystals including feldspar, quartz, and biotite (71R-1, 90–93 cm). F. Coarse-grained anhydrite characterized by elongated anhydrite and gypsum crystals with interstitial micrite (71R-CC, 20–22 cm).

3.2.3.2. Subunit IIIb

Subunit IIIb (~883–902 mbsf [bottom of the hole]; Table **T2**) consists of ~19 m thick anhydritic mudstone, mudstone, and micritic anhydrite with mica (<2 mm), lapilli-sized pumice, and gypsum. Core 398-U1591C-70R consists mostly of massive or unbedded (anhydritic) mudstone, whereas Core 71R consists of anhydritic mudstone and micritic anhydrite, resulting in bedding and laminations from Section 70R-3 downward (Figure **F14F**). Between ~884 and 886.4 mbsf the (anhydritic) mudstone is bluish gray, whereas the uppermost part of this subunit is dark gray or grayish green to dark gray. Pumice clasts are concentrated in Sections 70R-1 (0–29, 34–47, 65–77, and 90–114 cm), 70R-6 (11–101 cm), 71R-6 (0–140 cm), and 71R-7 (0–43 cm). Most are mica rich, probably biotite (Figure **F14E, F14F**). Gypsum nodules were macroscopically identified in Sections 71R-2 (79–106 cm), 71R-3 (0–143 cm), and 71R-4 (0–94 cm) based on their hardness (very easily scratchable) and color (light gray to white).

Two thin sections from Subunit IIIb show fine-grained anhydritic mudstone with grains of plagioclase, quartz, and biotite (Figure **F15E, F15F**) and coarse-grained anhydrite characterized by elongated anhydrite and gypsum crystals with interstitial micrite (Figure **F15F**).

3.3. Correlations between holes

The sediments recovered from Holes U1591A–U1591C partly allow for correlation of sediment-specific features such as volcanic layers (e.g., discrete ash or tuffaceous mud and ooze) or organic-rich (sapropelic) ooze and mud. Holes U1591A and U1591B largely overlap; however, Hole U1591A terminates at ~100 mbsf, whereas Hole U1591B continues to ~400 mbsf. The recovery of Hole U1591C was planned to largely overlap with Hole U1591B between ~160 and 260 mbsf to recover sediments that were lost in Hole U1591B; however, the recovery in Hole U1591C was not significantly better, resulting in many core recovery gaps and generally limiting correlations between both holes.

3.3.1. Notable correlated deposits

- Sections 398-U1591A-2H-5 (bottom depth = 11.35 mbsf) and 398-U1591B-2H-3 (11.85 mbsf) (Figure **F16A**). This ~39.5 cm thick interval of ash, tuffaceous ooze/mud, and lapilli-ash is generally volcanic rich with ~60 cm of thick lapilli-ash at the bottom, followed by a ~20–30 cm thick tuffaceous ooze, and a ~2 cm diffuse ash layer at the top. The tuffaceous ooze shows vertical, partly lens-shaped bioturbation.
- Sections 398-U1591A-4H-4 (bottom depth = 28.8 mbsf) and 398-U1591B-4H-2 (29.6 mbsf) (Figure **F16B**). This interval of calcareous tuffaceous mud, organic-rich ooze, and ooze with ash pods is characterized by its dark brown color, linked to the organic and tuffaceous material, and the gradational transition from organic-rich ooze to ooze. The ooze contains some ash pods.
- Sections 398-U1591A-8H-1 (bottom depth = 62.14 mbsf) and 398-U1591B-7H-5 (62.52 mbsf) (Figure **F16C**). The ash layer in this interval of ooze, ash, and ooze is discrete, although slightly disturbed by drilling, and roughly 4 cm thick. Toward the top, the ash grades into a tuffaceous ooze (~10–18 cm; slightly thicker in Hole U1591A).
- Sections 398-U1591B-23X-4 (bottom depth = 200.93 mbsf) and 398-U1591C-7R-2 (199.94 mbsf) (Figure **F17A**). The organic-rich ooze in this interval of ooze and organic-rich ooze is highly bioturbated (probably by *Zoophycos*) with tunnel-shaped, slightly inclined burrows.
- Sections 398-U1591B-27X-CC (bottom depth = 233.88 mbsf) and 398-U1591C-11R-1 (236.19 mbsf) (Figure **F17B**). This interval of gravelly tuffaceous sands and muds with ooze was only tentatively correlated between Holes U1591B and U1591C, due to strongly disturbed sediments in Hole U1591B. The gravel-sized clasts were identified as volcanic lithics and pumice.
- Sections 398-U1591B-30X-1 (bottom depth = 263.31 mbsf) and 398-U1591C-13R-CC (263.02 mbsf) (Figure **F17C**). The organic-rich ooze in this interval of ooze and organic-rich ooze shows a very sharp contact with the lower ooze and a slightly diffuse upper boundary. Sediments in both holes show signs of strong to severe drilling disturbance.

- Sections 398-U1591B-39X-1 (bottom depth = 350.94 mbsf) and 398-U1591C-15R-1 (351.2 mbsf) (Figure **F17D**). This interval of highly disturbed ash with cobble-sized lithics, especially in Hole U1591B, is highly disturbed by drilling. Nevertheless, based on the cobble-sized clasts, these two intervals are tentatively correlated. The main component of the light beige sediment is ash.
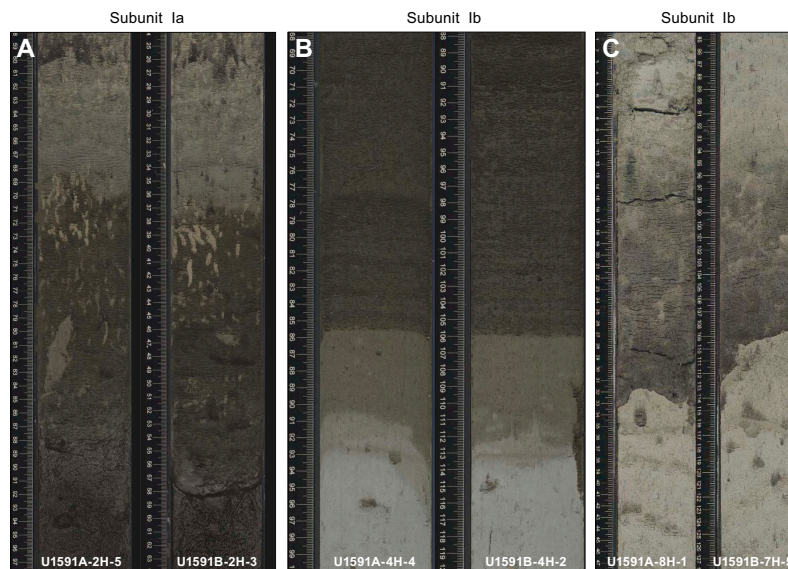
Figure F16. Exemplary correlations between Holes U1591A and U1591B. A. Volcanic and tuffaceous sediments (ash, tuffaceous ooze, calcareous tuffaceous mud, and lapilli-ash), top to bottom. B. Organic-rich sediments (calcareous tuffaceous mud, organic-rich ooze, and ooze with ash pods). C. Succession of nonvolcanic and volcanic-rich sediments (ooze, tuffaceous ooze, ash, and ooze). The ash layer in A is slightly disturbed, and the calcareous tuffaceous mud is bioturbated (light-colored vertical lenses). The discrete ash layer in C was probably disturbed by drilling; however, it is likely that suspended ash settled over time, leading to a gradational upper boundary.

Figure F17. Exemplary correlations between Holes U1591B and U1591C. A. Succession of ooze, strongly bioturbated organic-rich ooze, to ooze. B. Tentatively correlated gravelly tuffaceous mud to sand with gravel. Drilling disturbance in this sediment interval was strong in Hole U1591B and slight in Hole U1591C. C. Succession of ooze, organic-rich ooze, to ooze (top to bottom) disturbed by drilling especially above the organic-rich interval (Subunit IIa). D. Highly disturbed interval of intermixed ash, tuffaceous muds, and cobble-sized lithics.

3.4. X-ray diffraction

XRD data were collected from 8 interstitial water (IW) squeeze cake sediment residues from Hole U1591A, 11 from Hole U1591B, and 31 from Hole U1591C. The XRD spectra obtained on lithologies from Units I and II were similar to those from Sites U1589 and U1590, with the majority of analyses carried out on oozes and organic-rich oozes in addition to samples from tuffaceous sediments (oozes and muds) and volcanic lithologies. Oozes and organic-rich oozes and muds are characterized by calcite and quartz, and most samples also contain Ca-rich or Na-rich plagioclase and clay minerals of the illite group and, in some cases, the smectite group (montmorillonite). Other minerals identified in these lithologies include dolomite, ankerite, glauconite, and chlorite, among other minor phases. Tuffaceous sediments and ash show characteristic XRD patterns of glass-rich (volcanic) material with a characteristic hump at low °2θ, indicating the presence of an amorphous (noncrystalline) phase. Among the identified minerals in these lithologies were Ca-rich plagioclase, but the majority of phases identified were calcite, quartz, glauconite, and clay minerals of the illite and smectite groups (montmorillonite).

Discrete samples from Unit III were analyzed by XRD to characterize the evaporite sequences that define this lithostratigraphic unit, in particular Subunit IIIa. Selected XRD spectra are shown in Figure **F18**. Anhydrite has been identified as one of the major evaporite minerals, occurring as laminated and nodular varieties, and as veins and veinlets (Figure **F18A, F18B**). Other descriptive intervals in Subunit IIIa are dominated by dolomite with minor quartz or are characterized by a multimineral assemblage of dolomite and quartz with minor calcite and vermiculite (Figure **F18C, F18D**). The XRD spectra of two discrete samples analyzed from Subunit IIIb are characterized by Ca-rich plagioclase and muscovite (Sample 398-U1591C-71R-2, 34–35 cm) and Ca-rich plagioclase and illite, respectively.
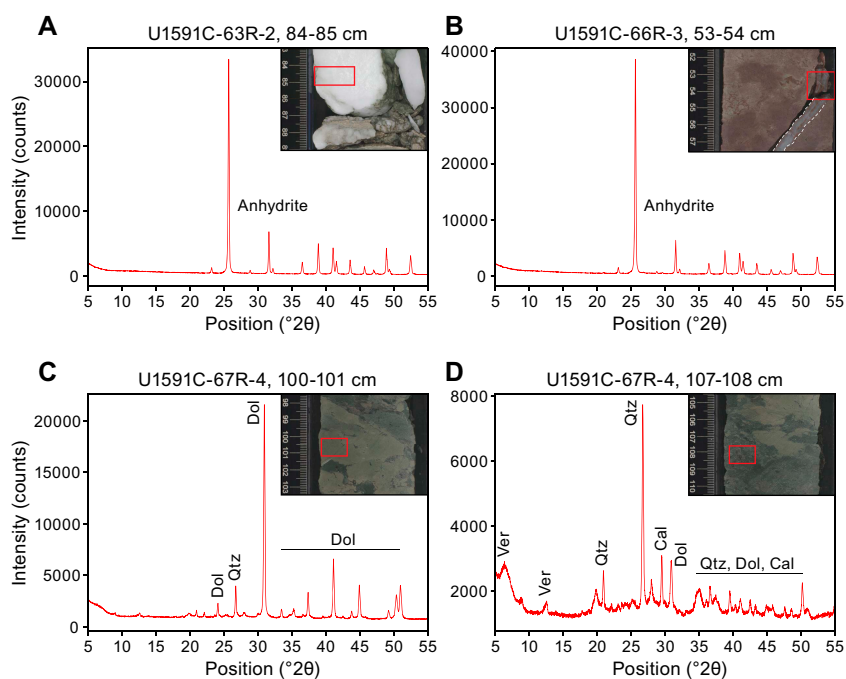
Figure F18. Selected XRD spectra of Unit III evaporite lithologies, Hole U1591C. A. Massive anhydrite. B. Anhydrite veinlet. C. Interval dominated by dolomite with minor quartz. D. Interval characterized by a multimineral assemblage of dolomite and quartz with minor calcite and vermiculite. Qtz = quartz, Dol = dolomite, Ver = vermiculite, Cal = calcite.

4. Stratigraphic correlation

Three holes were drilled at Site U1591. Hole U1591A was drilled to 90.85 mbsf (CSF-A scale) using only the APC system. Hole U1591B was drilled to 386.6 mbsf using the APC system (to 67.09 mbsf), the HLAPC system (98.8–112.9 and 146.7–152.88 mbsf), and the XCB system (117.6–137 and 156.1–386.6 mbsf). Between 74.1 and 98.8 mbsf, no cores were recovered intentionally to further advance through an interval that was difficult to drill in Hole U1591A. In Hole U1591C, the RCB system was used to drill to 902.67 mbsf, and the uppermost 149.3 m were intentionally not recovered.

4.1. Correlation during coring

Because Hole U1591A had proven to be very challenging for drilling, the priority for Hole U1591B was to advance without any delay. This implied that correlation during drilling was not required, and we did not use the Special Task Multisensor Logger (STMSL) for measurements of physical properties for fast correlations.

4.2. Correlation for establishing CCSF-A depth scale and construction of the splice

To establish the core composite depth below seafloor, Method A (CCSF-A), depth scale, we focused on the uppermost 67.09 m where piston coring was possible in Holes U1591A and U1591B and correlated the measured physical properties using the Whole-Round Multisensor Logger (WRMSL; for MS, gamma ray attenuation [GRA] density, and *P*-wave velocity), the Natural Gamma Radiation Logger (NGRL; for NGR intensity), and subsequently the Section-Half Multisensor Logger (SHMSL; for MS and color reflectance), as well as photos once the cores were split into working and archive halves (see **Physical properties**; also see **Physical properties** in the Expedition 398 methods chapter [Kutterolf et al., 2024]).

Both Holes U1591A and U1591B recovered the mudline. However, we used Core 398-U1591A-1H as the anchor because it recovered a few centimeters (3.6 cm) more of the mudline than Core 398-U1591B-1H. From there, we achieved a gapless correlation between Holes U1591A and U1591B to 68 m CCSF-A. Below this depth, however, no reliable correlations were possible due to the low recovery. All depth offsets are reported in Table **T3**.

Figure **F19** shows MS for the uppermost 70 m for both holes on the shifted CCSF-A scale, as well as the splice (core composite depth below seafloor, Method D [CCSF-D], scale) generated by combining representative intervals from both holes. In general, we identified a very good correlation between the MS measurements for both holes that also resulted in a reliable correlation of the other physical properties and the core photos. The only interval where the correlation was more difficult was between Cores 398-U1591A-5H and 398-U1591B-5H (~42 m CCSF-A), where the ash layers in the lower part of Core 398-U1591A-5H are significantly thicker than those in Core 398-U1591B-5H.

For the deeper part of the stratigraphy below 68 mbsf, where no reliable correlations were possible, we did not apply any shifts to keep the CCSF-A scale as close to the CSF-A scale as possible. Figure **F20** shows the resulting splice (CCSF-D scale) from Holes U1591A–U1591C (see Table **T4** for splice ties). Hole U1591C successfully closed major gaps between ~225 and 264 mbsf and provides a surprisingly continuous record of the subsurface between 300 and 900 mbsf, when considering that Hole U1591C was drilled with the RCB system.

In general, no significant core expansion was observed during curation and handling of the cores. Figure **F21** shows a plot comparing the CSF-A and CCSF-A scales for Holes U1591A and U1591B and a linear regression curve calculated for both holes together for the uppermost 60 m. The deviation from the dotted line indicates an affine growth factor of approximately 3%.

**Table T3.** Affine ties, Site U1591. **Download table in CSV format.**
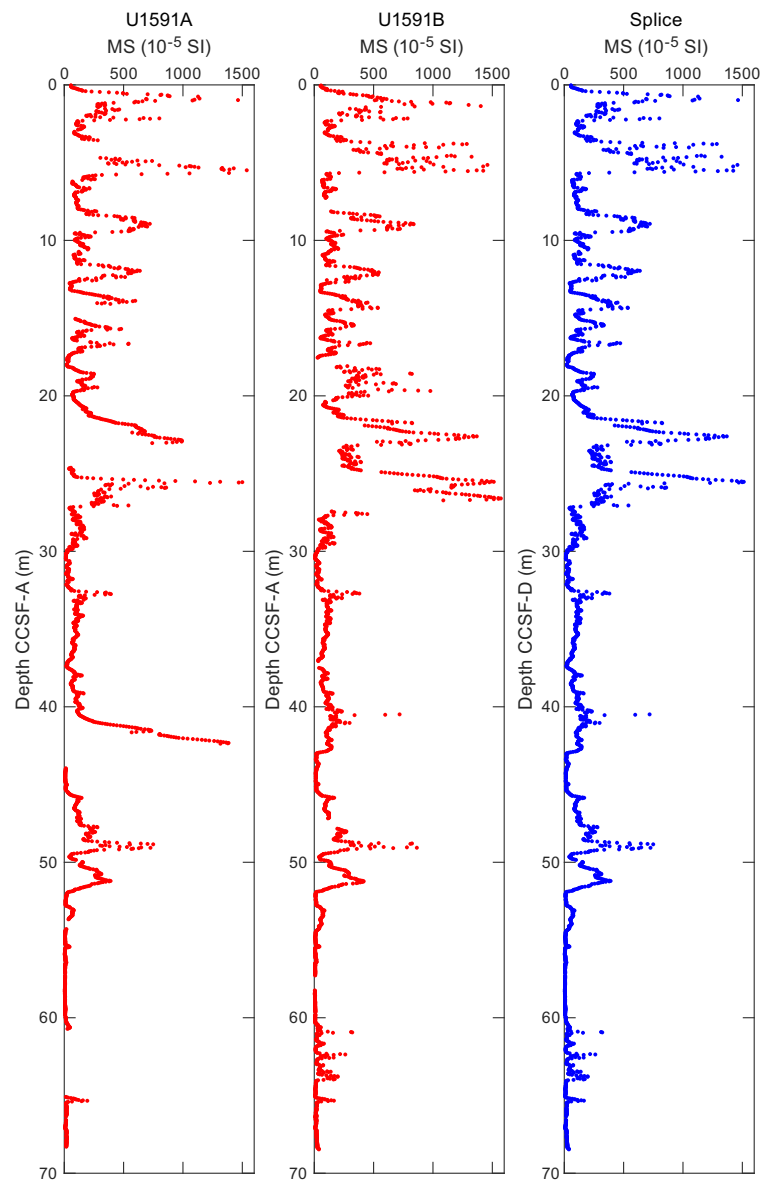
Figure F19. WRMSL-derived MS data, Holes U1591A and U1591B. The spliced section is shown in the right panel. Note that MS data are on the CCSF-A depth scale and the spliced section is on the CCSF-D depth scale. MS data were clipped at 1600 × 10⁻⁵ SI.
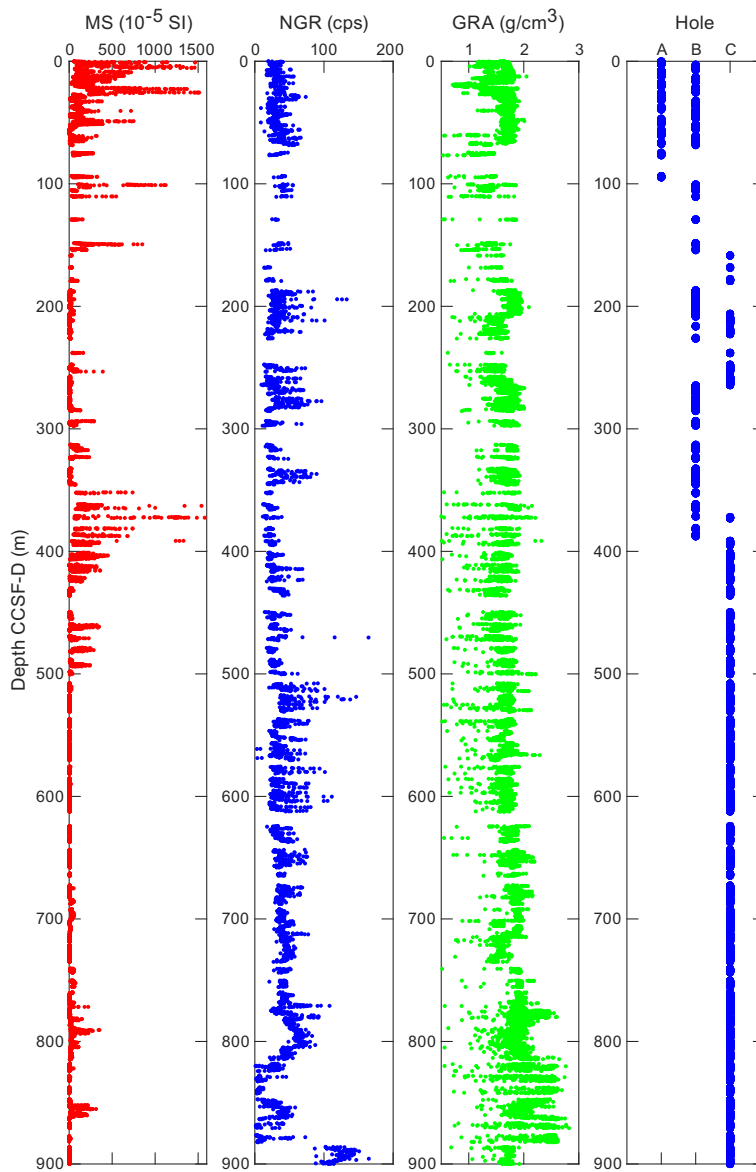
Figure F20. Splice for Site U1591 showing MS, NGR, and GRA density, as well as the respective spliced core interval from Holes U1591A–U1591C. cps = counts per second.

Table T4. Splice ties, Site U1591. **Download table in CSV format.**
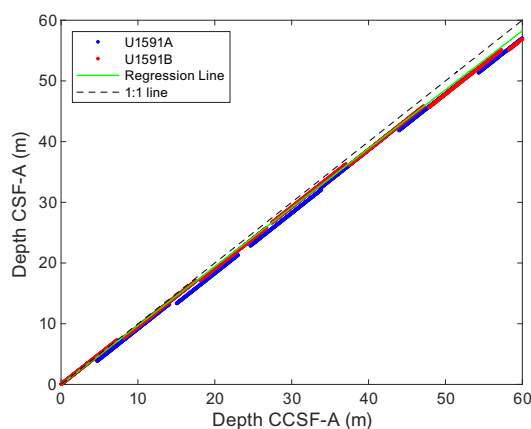
Figure F21. CCSF-A versus CSF-A core depths, Holes U1591A and U1591B. Lines fit through the core depths of all holes give an estimate of the affine growth factor. At Site U1591, this is estimated to be approximately 3%.

5. Structural geology

Structural geology analyses at Site U1591 included description of cores retrieved from Holes U1591A–U1591C. A total of 535 structures were measured, and most of those measurements derive from relatively consolidated intervals. Observed and measured structures on cores are bedding (79.1%), faults and deformation bands (12.7%), mineral veins (1.3%), and sediment veins (1.3%). The distributions and dip angles of planar structures are shown in Figure **F22**. The precision of shipboard orientation measurements is estimated to be ±2°. Deformation related to drilling and core recovery was noted but not recorded. Here, we describe and provide examples of each of the features that were recorded.

5.1. Bedding

Bedding planes (n = 423) were measured mainly on thin sand beds/laminae, sapropels, micrites, and anhydrite boundaries. They exhibit horizontal to subhorizontal dips above 350 mbsf (n = 133; mostly ≤10°; mean dip = 3.9°; median dip = 3.2°; standard deviation = 2.5°). However, steeper dips are observed below 350 mbsf, ranging 5°–85° (n = 290; mean dip = 11.4°; median dip = 5.6°; standard deviation = 14.1°) (Figure **F22**).

To evaluate the bedding dip variations in the ~900 m deep hole, we divided bedding measurements corresponding to the lithostratigraphic units/subunits defined by core description (see **Lithostratigraphy**) and used a box plot to indicate the distribution of bedding dips (Figure **F23**). Measurements were mostly concentrated in Lithostratigraphic Unit I and Subunits IIa–IIf, IIIa, and IIIb, but were limited by core recovery in Lithostratigraphic Subunit Ic (see **Lithostratigraphy**; Figure **F22**). Thus, a total of nine bedding measurement units were described that correspond respectively to the abovementioned lithostratigraphic units/subunits. In the box plot, each box indicates the data distribution range between the twenty-fifth and seventy-fifth percentiles, which is statistically meaningful. Median values (fiftieth percentile of all respective measurements in a unit) representative of the data distribution were used for evaluation of dip angles.

Major increases in bedding dip were identified at the bottom of Subunits IIe, IIc, and IIb. These occur in lithostratigraphic units/subunits where slump deposits were identified and consist of either volcanic- or tuffaceous-rich lithologies and ooze (see **Lithostratigraphy**; Figures **F23**, **F24**). In contrast, lithostratigraphic units/subunits without distinguishable volcanic records show decreasing median dips from the bottom to top also within the twenty-fifth to seventy-fifth percentile ranges, indicating that the tectonic tilting of Christiana Basin generally decreased upward. More specifically, for nonvolcanic units, the dip distributions are all positively skewed (indicating the median dip is closer to the lower quartile), with the median dip decreasing monotonically from 9.4° in Lithostratigraphic Subunit IIIb to 2.8° in Subunit IIa. Increases in median dip (from 3.9° to

13.3°) were identified between Subunits IIf and IIe. Similar major increases occurred between Subunits IId and IIc (from 3.6° to 8.0°) and between Subunit IIa and Unit I (from 2.8° to 3.6°) (Figure **F23**). All changes noted above occurred from nonvolcanic units to volcanic units, indicating either that earthquakes associated with volcanism triggered slumping or that the volcanism and slumping were both the consequence of rift pulses (Figure **F24**). From Subunit IIc to Subunit IIb, an
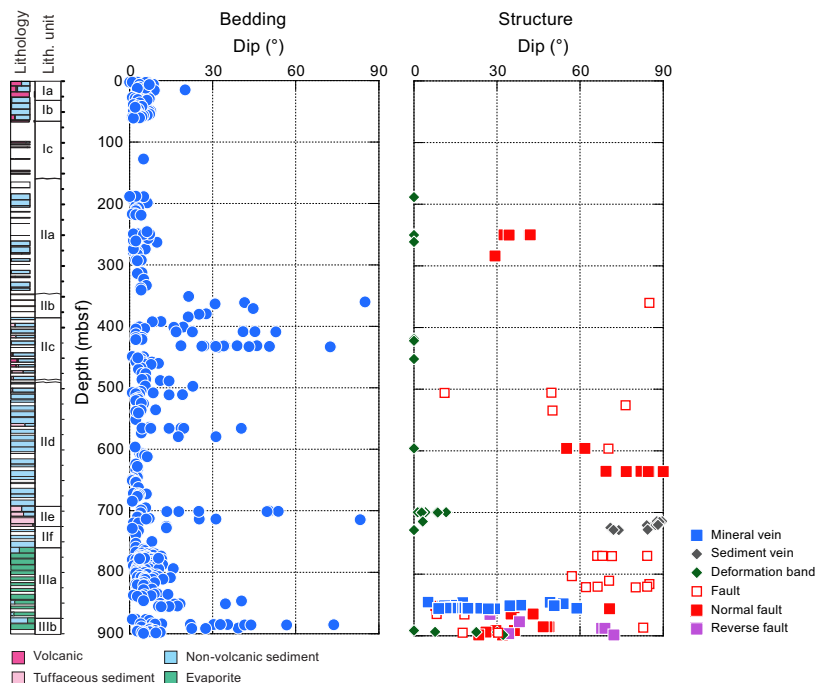

Figure F22. Dip data, Site U1591.
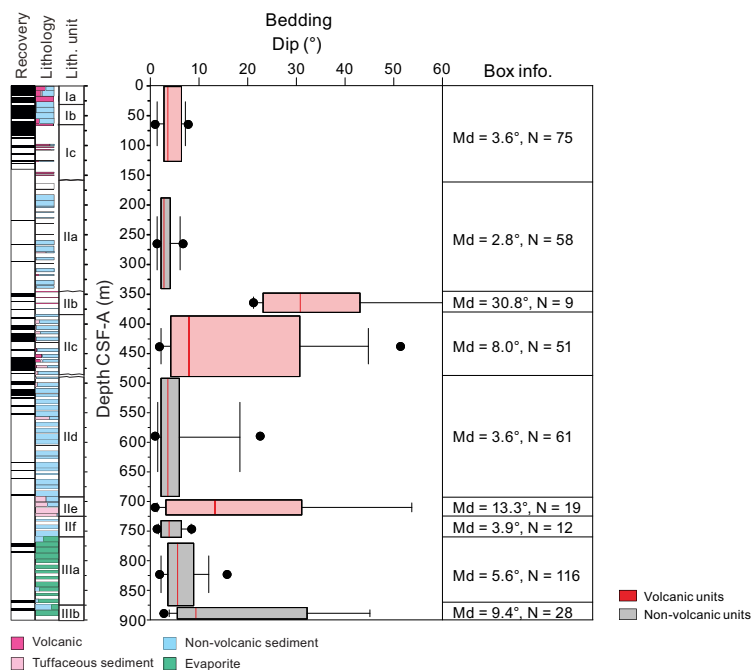
Figure F23. Box plots of bedding dip distribution in lithostratigraphic units, Site U1591. The minimum (P5), first quartile (P25), median value (P50), third quartile (P75), and maximum (P95) are shown. Only the first outlier that is smaller than P5 and larger than P95 is plotted as a dot. Md = median dip, N = number of samples.

obvious increase in the median dip (from 8.0° to 30.8°) was identified, indicating that a stronger disturbance occurred in Subunit IIb (Figure **F23**).

5.2. Slumps

At Site U1591, slump deposits were frequently identified as (1) block-in-matrix occurrences, (2) flow/disturbed mud, and (3) folding of sandy laminae/beds in muddy matrixes (Figure **F24**). The uppermost slump in the retrieved interval is from Sections 398-U1591C-9R-4 through 12R-1 (220–245 mbsf). The same slump interval is correlated to Section 398-U1591B-27X-CC (233 mbsf). Below 350 mbsf in Hole U1591C, a minor slump occurred at ~360 mbsf and slump-dominant intervals are identified at 420–477, 565–582, 699–708, and 885–890 mbsf (Figures **F22**, **F24**). These slump horizons also correspond to the intervals of drastic increase in sedimentation rate (see **Biostratigraphy**), indicative of thick accumulation/duplication of the same sedimentary intervals by slumping.

Most of the slump deposits at Site U1591 were classified as the third type listed above: folding of sandy laminae/beds in muddy matrixes (Figure **F24A, F24B**). Continuous sandy beds traced on a core-section scale (~1 m) rarely show disaggregation or flowage, but they present small-scale brittle deformation, each offset by a few millimeters filled with homogeneous muddy matrix. This type of slump lacks strong disturbance, and the mixture of materials apparently formed during slower migration (e.g., creep) in contrast to other types of slumps (Figure **F24C–F24F**). On the other hand, other examples in the cores show the first and second slump types (block-in-matrix and flow/disturbed-mud with highly mixed matrixes) (Figure **F24C, F24D**). The occurrence of polymictic clasts (Figure **F24E, F24F**) is also indicative of longer distances of transport compared with slump types associated with folding of sandy laminae/layers.
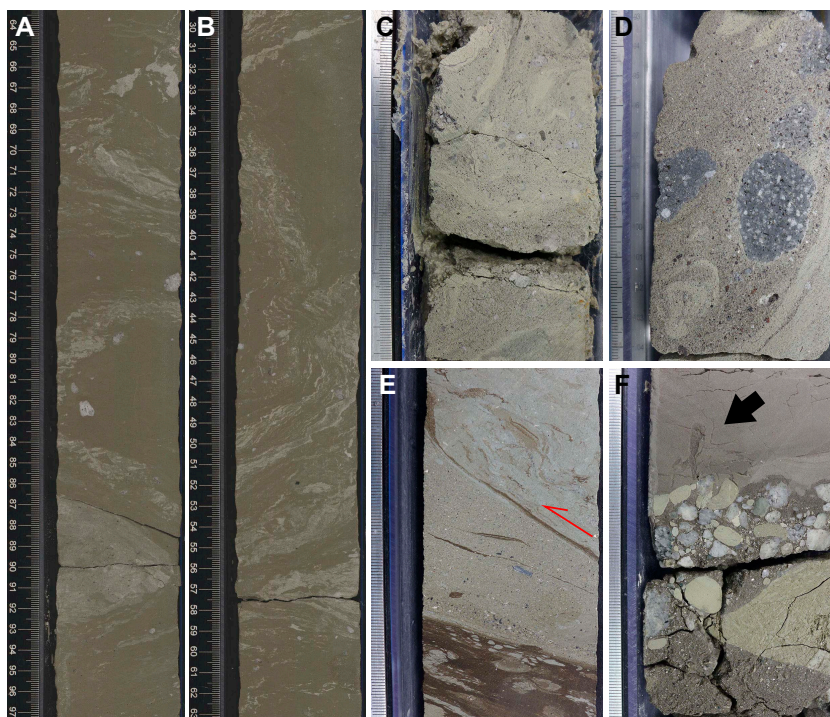

Figure F24. Slumps identified on split core surfaces. A, B. Slump composed of folded sandy laminae/beds in a muddy matrix (398-U1591C-23R-4, 29–97 cm). C. Slump representing block-in-matrix texture containing disturbed/flown muddy clasts within a mud/sand-mixture matrix (398-U1591B-27X-CC, 5–17 cm). D. Slump representing block-in-matrix texture containing pumice and siltstone clasts all within a mud/sand-mixture matrix (398-U1591C-15R-CC, 93–104 cm). E. Base of a slump representing an apparent reverse fault (split arrow; 38R-CC, 37–49 cm). The slip plane is composed of homogenized sand/mud. F. Top of a debris flow deposit (arrow; 398-U1591B-33X-CC, 16–28 cm). Clasts only occur in the uppermost part of the sand layer and indicate reverse grading.

5.3. Faults

Small-scale faults are apparent on split core surfaces (Figure **F25**). They show displacement from a few millimeters to a centimeter. The sense and/or amount of displacement is defined where these faults cut bioturbation or sedimentary structures and by asymmetric fabrics within and around the faults. Faults at Site U1591 have normal and reverse senses of displacement and mostly represent cohesive (healed) fault planes with closed fault planes. Only in Lithostratigraphic Unit III do some of the normal faults have open fault planes with slickenlines, slickensteps, and mineral growth (Figure **F26F**). Although there is a population of reverse faults in Unit III, they are developed in the folded sandstone layers of a slump interval (Figure **F24E**).
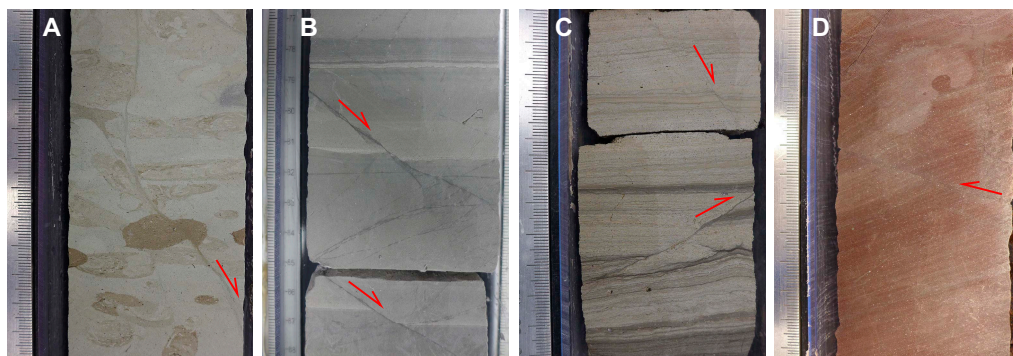
Figure F25. Small faults identified on split core surfaces, Hole U1591C. Arrows indicate the position of the faults and sense of shear direction. A, B. Normal faults identified just below slump layers (A: 40R-3, 33–45 cm; B: 12R-4, 77–88 cm). C, D. Reverse faults (C: 69R-3, 86–98 cm; D: 66R-6, 62–75 cm). Note in C a normal fault also developed.
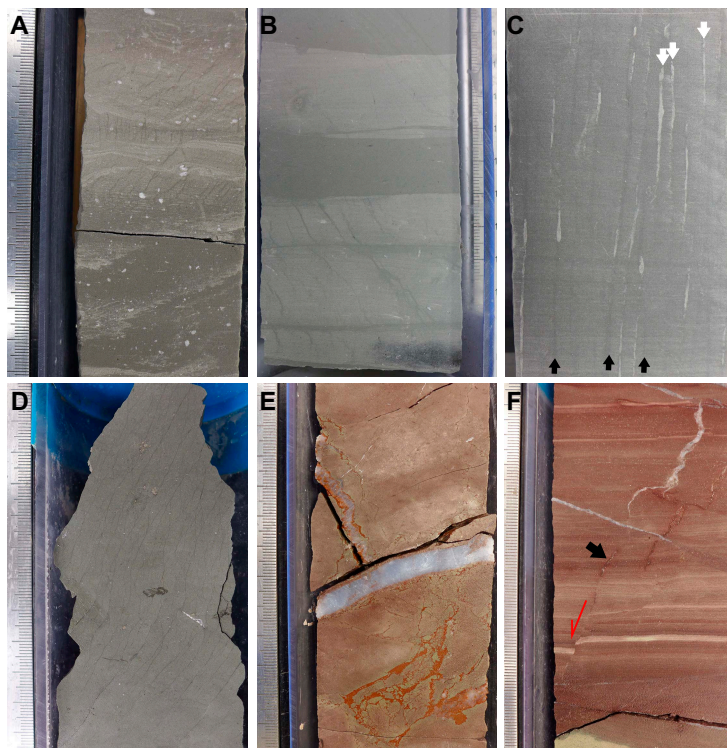
Figure F26. Sediment-filled veins in Units II and III, Hole U1591C. A–D. Typical occurrences of mud-filled vein structure in Unit II (A: 12R-1, 37–49 cm; B: 26R-4, 104–116 cm; C: 53R-2, 64–74 cm; D: 51R-CC, 0–13 cm). Note in C sand-filled veins (white arrows) apparently developed parallel to the mud-filled veins (black arrows) in the split-core section. E, F. Anhydrite veins developed in Unit III (E: 66R-1, 119–131 cm; F: 67R-2, 2–15 cm). Note small crystal growths (black arrow) along the normal fault (split arrow).

A larger population of normal faults developed just below the slump intervals (Figure **F22**), possibly indicating that a sudden increase of overburden pressure was associated with slump initiation, leading to the formation of larger differential stress as well as excess fluid pressure and finally achieving failure. Generation of slumps and normal faults associated with rapid increase of overburden are consistent with the extensional stress field of the Christiana Basin.

Deformation bands parallel/subparallel to the bedding planes are characterized by a black seam developed throughout the core. Although it is difficult to identify the offset and sense of shear, these bands represent density reduction and small offset (e.g., Hanamura and Ogawa, 1993; Maltman et al., 1993). They apparently formed soon after sedimentation.

5.4. Sediment-filled veins and mineral veins

Sediment-filled veins and mineral veins were identified in specific intervals in the lower parts of Lithostratigraphic Units II and III, respectively (Figure **F26**). Sediment-filled veins are divided into two types: mud-filled and sand-filled veins. The former is recognized as parallel sets or arrays of sigmoidal or curviplanar seams generally <1 mm wide, as found from 714 to 721 mbsf (Cores 398-U1591C-52R and 53R) (Figures **F22**, **F26A–F26D**). The typical thickness of these vein arrays is 1–10 cm.

Mud-filled veins are called "vein structure" and are common in sediments at subduction zones (accretionary prism, slope, and forearc basins; Hanamura and Ogawa, 1993; Maltman et al., 1993). They were identified in cores retrieved by ocean drilling including at the Nankai, Costa Rica, and Oregon margins and also in shallowly buried accretionary prism/slope sediments exposed on land in the Miura/Boso Peninsulas, Japan, and the Monterey Formation (USA) (Hanamura and Ogawa, 1993; Maltman et al., 1993; Shipboard Scientific Party, 2001; Expedition 334 Scientists, 2012). Field and experimental studies have shown that these structures are caused by the shaking of sediments during earthquakes (Hanamura and Ogawa, 1993; Brothers et al., 1996).

On the other hand, sand-filled veins are recognized as parallel sets or curviplanar seams generally <1 mm wide and were found from 720 to 728 mbsf (Core 398-U1591C-53R) (Figures **F22**, **F26C**). The dip angle of each vein ranges 71°–87°, almost parallel to the mud-filled vein structures on the split core surface. However, they apparently cross in three dimensions. This crosscutting relationship has not been identified previously because of its faint appearance. The typical length of these vein arrays is 2–5 cm.

Mineral veins mostly filled with anhydrite were identified in Unit III (Figure **F22**). The veins are 1–5 mm thick and occur from 844 to 856 mbsf (Cores 398-U1591C-66R and 67R). Although their dip angles are distributed over a wide range, most are parallel to bedding planes. However, some cut the bedding planes at higher dip angles (Figure **F26E, F26F**).

6. Biostratigraphy

Planktonic and benthic foraminifera and calcareous nannofossils were examined from core catcher samples and additional split core samples from Holes U1591A–U1591C to develop a shipboard biostratigraphic framework for Site U1591. Additionally, planktonic and benthic foraminifera provided data on paleowater depths, downslope reworking, and possible dissolution.

Site U1591 cored the Christiana Basin sedimentary sequence and recovered a 902.59 m thick Holocene to Early Pliocene (Late Miocene?) sequence composed primarily of volcanogenic sediments, calcareous and tuffaceous oozes, and evaporitic and siliciclastic sediments. Calcareous nannofossils and planktonic foraminifera provided good resolution in the Holocene through Early Pliocene sediments. Ages provided by benthic foraminifera were also consistent with those of planktonic foraminifera and calcareous nannofossils. Biostratigraphic datums recognized at Site U1591 are given in Tables **T5** and **T6**, and an age-depth plot is shown in Figure **F27**.

In Hole U1591A, Holocene to Middle Pleistocene aged sediments (0–0.51 Ma) were recovered from Samples 1H-CC, 11–16 cm, to 10H-CC, 0–5 cm (3.79–79.85 mbsf). Hole U1591B recovered Holocene to Early Pleistocene aged sediments (0–2.41 Ma) from Samples 1H-CC, 20–23 cm, to

43X-CC, 39–41 cm (7.56–386.6 mbsf). Hole U1591C recovered Pleistocene to Early Pliocene aged sediments (~1.2–5.33 Ma) from Samples 3R-CC, 0–2 cm, to 58R-2, 13–15 cm (158.73–768.62 mbsf), and sediments of an indeterminate age from Samples 58R-2, 89–91 cm, to 70R-CC, 0 cm (769.38–902.59 mbsf).

Table T5. Calcareous nannofossil events and absolute ages, Site U1591. **Download table in CSV format.**

Calcareous nannofossil event	Top age (Ma)	Middle age (Ma)	Bottom age (Ma)	Top core, section, interval (cm)	Bottom core, section, interval (cm)	Top depth CSF-A (m)	Mid-depth CSF-A (m)	Bottom depth CSF-A (m)
				398-U1591A-	398-U1591A-			
Base *Emiliania huxleyi*		0.265		3H-CC, 17–20	4H-CC, 26–29	21.59	31.44	41.29
Top *Pseudoemiliania lacunosa*		0.467		5H-CC, 25–28	6H-CC, 20–23	41.32	46.565	51.81
				398-U1591B-	398-U1591B-			
Base *Emiliania huxleyi*		0.265		3H-CC, 15–16	4H-4, 117–119	26.00	29.135	32.27
Top *Pseudoemiliania lacunosa*		0.467		5H-CC, 24–27	6H-CC, 25–28	46.15	50.775	55.40
Top large *Gephyrocapsa* spp. (>5.5 μm)		1.245		22X-CC, 34–38	23X-CC, 18–20	194.95	199.75	204.55
Base large *Gephyrocapsa* spp. (>5.5 μm)		1.617		27X-CC, 18–21	29X-CC, 0–3	233.91	243.505	253.10
Base medium *Gephyrocapsa* spp. (> 4.0 μm)		1.73		29X-CC, 0–3	30X-CC, 39–44	253.13	261.89	270.65
Top *Discoaster brouweri*		1.95		31X-CC, 35–38	32X-CC, 37–40	282.30	283.31	284.32
Acme base *Discoaster triradiatus*		2.216		34X-CC, 0–2	35X-CC, 38–43	301.62	309.105	316.59
				398-U1591C-	398-U1591C-			
Top large *Gephyrocapsa* spp. (>5.5 μm)		1.245		6R-CC, 16–18	7R-CC, 0–2	191.85	198.61	205.37
Base large *Gephyrocapsa* spp. (>5.5 μm)		1.617		11R-CC, 0–2	12R-CC, 11–14	236.41	243.97	251.53
Top *Discoaster pentaradiatus*		2.512		26R-CC, 0–3	28R-CC, 22–24	462.46	471.325	480.19
Top *Discoaster tamalis*		2.8		31R-CC, 19–21	32R-CC, 21–23	511.84	517.49	523.14
Top *Sphenolithus abies*		3.7		42R-CC, 0–2	43R-CC, 9–11	612.14	620.91	629.68
Top *Reticulofenestra pseudoumbilicus*		3.839		44R-CC, 0–2	45R-CC, 20–25	634.71	642.84	650.97
Base *Discoaster tamalis*		3.97		46R-CC, 13–16	47R-CC, 0–2	655.71	659.01	662.31
Base *Helicosphaera sellii*		4.62		51R-CC, 25–30	54R-CC, 39–42	708.25	720.57	732.89
Paracme end *R. pseudoumbilicus*		4.91		55R-CC, 0–3	56R-CC, 8–10	741.38	747.285	753.19
Top *Reticulofenestra zancleana*		5.199		56R-CC, 8–10	57R-7, 3–5	753.21	759.41	765.61
Bottom *Reticulofenestra zancleana*		5.322		57R-CC, 3–5	58R-1, 130	765.63	767.515	769.40
MNN6/NN6/CN5a/CNM8	12.57	13.085	13.6	60R-1, 4–7		786.53	786.545	786.56
MNN5/NN5/CN4/CNM7	13.6	14.23	14.86	68R-4, 83–85		868.07	868.085	868.10

Table T6. Foraminiferal events and absolute ages, Site U1591. **Download table in CSV format.**

Foraminifer event	Age (Ma)	Top core, section, interval (cm)	Bottom core, section, interval (cm)	Top depth CSF-A (m)	Mid-depth CSF-A (m)	Bottom depth CSF-A (m)
		398-U1591A-	398-U1591A-			
Base *Globigerinoides ruber* var. pink	0.33	3H-CC, 17–20	4H-CC, 26–29	21.59	26.995	32.40
Paracme top *Neogloboquadrina* spp. (sin)	0.51	7H-CC, 24–27	8H-1, 39–41	58.08	59.645	61.21
		398-U1591B-	398-U1591B-			
Paracme top *Neogloboquadrina* spp. (sin)	1.21	22X-CC, 34–38	23X-CC, 18–20	194.95	199.75	204.55
Top *Globigerinoides obliquus*	1.28	23X-CC, 18–20	24X-CC, 38–41	204.55	205.89	207.23
Base common *Hyalinea balthica*	1.492	24X-CC, 38–41	25X-CC, 21–24	207.23	211.165	215.10
Base common *Globoconella inflata*	1.99	29X-CC, 0–3	30X-CC, 39–44	253.13	261.915	270.70
Base *Globoconella inflata*	2.09	31X-CC, 35–38	32X-CC, 18–20	282.30	283.225	284.15
Top *Globorotalia bononiensis*	2.29	38X-CC, 37–40	39X-CC, 31–36	344.28	347.90	351.52
Top *Neogloboquadrina atlantica* (sin)	2.41	40X-CC, 20–22	41X-CC, 18–22	364.56	367.405	370.25
Top common *Globorotalia bononiensis*	2.41	42X-CC, 0–3	43X-CC, 39–41	380.60	383.60	386.60
		398-U1591C-	398-U1591C-			
Top common *Globigerinoides obliquus*	2.54	28R-CC, 22–24	29R-CC, 0–2	480.21	485.835	491.46
Top *Sphaeroidinellopsis* s.l.	3.19	32R-CC, 21–23	33R-CC, 14–17	523.16	525.805	528.45
Top *Globoconella puncticulata*	3.57	39R-CC, 0–2	40R-CC, 18–20	590.59	596.355	602.12
Top *Hirsutella margaritae*	3.81	44R-CC, 0–2	45R-CC, 23–25	634.71	642.85	650.99
Top common *Hirsutella margaritae*	3.98	46R-CC, 13–16	47R-CC, 0–2	655.71	659.02	662.33
Top *Globoturborotalita nepenthes*	4.6	51R-CC, 25–30	54R-CC, 39–42	708.25	720.585	732.92
Acme Top *Sphaeroidinellopsis* s.l.	5.21	55R-CC, 0–3	56R-CC, 8–10	741.38	747.295	753.21
Acme Base *Sphaeroidinellopsis* s.l.	5.3	56R-CC, 8–10	57R-7, 3–5	753.21	759.42	765.63
Base *Siphonina reticulata*	5.234	58R-1, 129–131	58R-2, 13–15	768.41	768.515	768.62

6.1. Calcareous nannofossils

Calcareous nannofossil biostratigraphy in Holes U1591A–U1591C was established through analysis of core catcher samples, with additional split core samples taken to better constrain biostratigraphic events. Nannofossils are rare to abundant in samples from the Pleistocene–Pliocene sequence (Hole U1591A = 3.765–79.825 mbsf; Hole U1591B = 7.545–386.59 mbsf; Hole U1591C = 158.72–769.72 mbsf) and are rare to barren in Miocene samples (Hole U1591C = 776.47–892.1 mbsf). Preservation is moderate to poor throughout the sequence, and there is significant reworking of older material in most of the Pleistocene and Pliocene samples (Figure **F28**). Sixteen nannofossil biostratigraphic datums and two calcareous nannofossil zones are recognized at Site U1591, representing a discontinuous Pleistocene to Miocene sedimentary sequence. Distributions of calcareous nannofossil taxa are shown in Table **T7**, and biostratigraphic datums are given in Table **T5** and in GEODESC.

6.1.1. Pleistocene

The presence of *Emiliania huxleyi* in Samples 398-U1591A-1H-CC, 11–16 cm, to 3H-CC, 17–20 cm (3.765–21.575 mbsf), and 398-U1591B-1H-CC, 20–23 cm, to 3H-CC, 15–16 cm (7.545–25.995 mbsf), indicates a Holocene to Middle Pleistocene age (≤0.29 Ma) in Zones MNN21a and MNN21b (CNPL11, Backman et al., 2012; NN21, Martini, 1971; CN15, Okada and Bukry, 1980) of Rio et al. (1990) and Di Stefano and Sturiale (2010) (Figure **F28**). The top occurrence of *Pseu-*
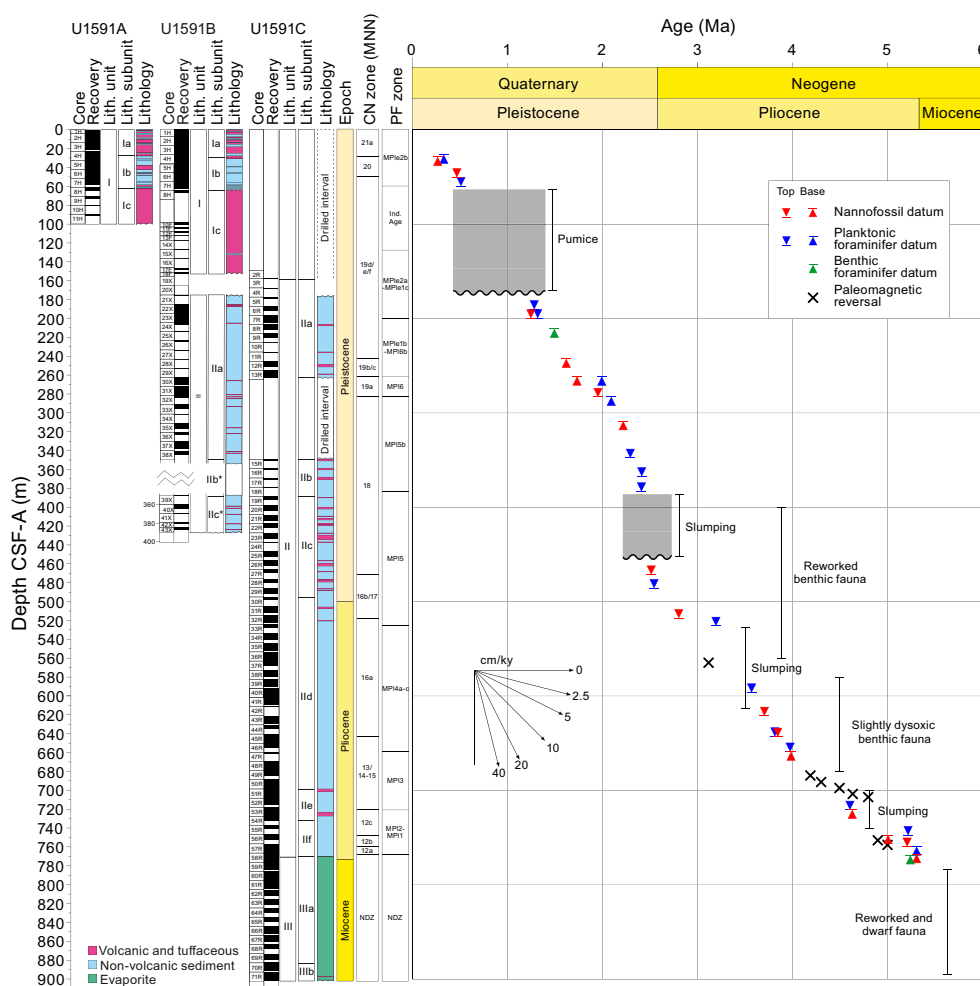

Figure F27. Age-depth plot, Holes U1591A–U1591C. Integrated biochronology and magnetostratigraphy are shown. CN = calcareous nannofossil, MNN = Mediterranean Neogene Nannoplankton, PF = planktonic foraminifer. Hiatuses correspond to periods of significant sediment remobilization. Biohorizons are listed in Tables T6 and T9. * = depth and recovery affected by slumped material.

doemiliania lacunosa defines the Zone MNN20/21a (CNPL10/11, NN19/20, and CN14a/CN14b) boundary. The last consistent appearance of *P. lacunosa* in Holes U1591A and U1591B occurs in Samples 398-U1591A-6H-CC, 20–23 cm (51.825 mbsf), and 398-U1591B-6H-CC, 25–28 cm (55.415 mbsf). The large form of *Gephyrocapsa* spp. (>5.5 µm) appears between 1.245 and 1.617 Ma (Zones MNN19d, CNPL8, NN19, and CN13b) and occurs between Samples 398-U1591B-23X-CC, 18–20 cm, and 27X-CC, 18–21 cm, and between Samples 398-U1591C-7R-CC, 0–2 cm, and 11R-CC, 0–2 cm. Samples 398-U1591B-29X-CC, 0–3 cm, and 398-U1591C-12R-CC, 11–14 cm, and 13R-CC, 14–16 cm, are characterized by the occurrence of *Gephyrocapsa oceanica*, *Gephyrocapsa caribbeanica*, and *P. lacunosa* and by the absence of the large form of *Gephyrocapsa* spp. This indicates that these intervals (U1591B = 253.1–270.65 mbsf; U1591C = 251.53–263.04 mbsf) are assigned to an age between 1.617 and 1.73 Ma. The Gelasian (Early Pleistocene) assemblages found at this site are characterized by the occurrence of discoasters that include marker species of Miocene–Pliocene successions. The last occurrence of *Discoaster brouweri*, which indicates the Zone MNN18/19a boundary (NN18/19 and CN12d/CN13a), occurs between Samples 398-U1591B-31X-CC, 35–38 cm, and 32X-CC, 37–40 cm (283.31 mbsf). The acme base of *Discoaster triradiatus*, which characterizes middle Zone MNN18 (2.216 Ma), appears between Samples 34X-CC, 0–2 cm (301.62 mbsf), and 35X-CC, 38–43 cm (316.59 mbsf).

6.1.2. Pliocene

In Hole U1591C, the top of *Discoaster pentaradiatus* (2.512 Ma) occurs at the boundary between Samples 398-U1591C-26R-CC, 0–3 cm, and 28R-CC, 22–24 cm (471.325 mbsf), and defines Zone MNN17/18 (NN/17/18, CN12c/d, and CNPL5/6). *Discoaster tamalis* disappears at 2.8 Ma in the upper part of the Gauss Chronozone. This specimen last occurs in Hole U1591C between Samples 31R-CC, 19–21 cm (511.84 mbsf), and 32R-CC, 21–23 cm (523.14 mbsf). *Sphenolithus abies*, with
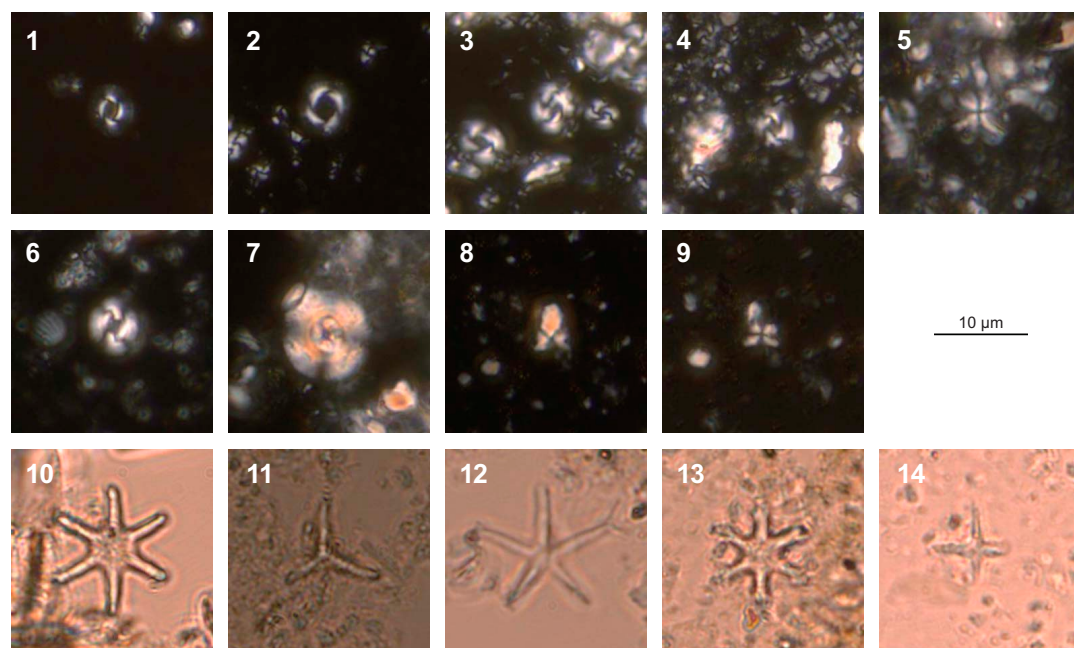
Figure F28. Calcareous nannofossils. 1. *Emiliania huxleyi* (Lohmann) Hay and Mohler (398-U1591A-3H-CC, 17–20 cm). 2. *Pseudoemiliania lacunosa* (Kamptner) Gartner, (8H-1, 39–41 cm). 3, 4. 398-U1591B-24X-CC, 38–41 cm: (3) *Gephyrocapsa* spp. large form (>5.5 µm); (4) *Gephyrocapsa oceanica* Kamptner. 5. *Sphenolithus abies* Deflandre (398-U1591C-48R-CC, 0–4 cm). 6. *Reticulofenestra pseudoumbilicus* (Gartner) (54R-CC, 42–49 cm). 7. *Cyclicargolithus floridanus* (Roth and Hay) Bukry (60R-1, 3 cm). 8, 9. *Sphenolithus heteromorphus* Deflandre (68R-4, 83–86 cm). 10. *Discoaster brouweri* Tan Sin Hok (23R-CC, 21–24 cm). 11. *Discoaster triradiatus* Tan Sin Hok (398-U1591B-34X-CC, 0–2 cm). 12. *Discoaster pentaradiatus* Tan Sin Hok (398-U1591C-29R-CC, 0–2 cm). 13. *Discoaster surculus* Martini and Bramlette (31R-CC, 19–21 cm). 14. *Discoaster tamalis* Kamptner (32R-CC, 21–23 cm).

Table T7. Distribution of calcareous nannofossils, Site U1591. **Download table in CSV format.**

its last occurrence in the lower part of Zone MNN16a (3.7 Ma; NN16/CN12a/CNPL4), is found in and below Sample 43R-CC, 9–11 cm. The last occurrence of *Reticulofenestra pseudoumbilicus*, which shows the boundary of Zone MNN15/16 (3.839 Ma; NN15/16, CN11b/12a, and CNPL3/4), is recognized between Samples 44R-CC, 0–2 cm (634.71 mbsf), and 45R-CC, 20–25 cm (650.97 mbsf). The base common occurrence of *D. tamalis* in Zone MNN14-15 (3.97 Ma) is found at the boundary between Samples 46R-CC, 13–16 cm (655.71 mbsf), and 47R-CC, 0–2 cm (662.31 mbsf). The base common occurrence of *Helicosphaera sellii*, which indicates the boundary of Zone MNN12c/13 (4.62 Ma), occurs between Samples 51R-CC, 25–30 cm (708.25 mbsf), and 54R-CC, 39–42 cm (732.89 mbsf). *R. pseudoumbilicus* shows a paracme (absence interval) in the Lower Pliocene (Di Stefano and Sturiale, 2010). This specimen paracme top appears in Samples 55R-CC, 0–3 cm (741.38 mbsf), and 56R-CC, 8–10 cm (753.19 mbsf). *Reticulofenestra zancleana*, which characterizes the lowermost Pliocene (5.199–5.322 Ma; MNN12a) in the Mediterranean area (Di Stefano and Sturiale, 2010), occurs between Samples 57R-CC, 14–16 cm (767.39 mbsf), and 58R-1, 130 cm (768.4 mbsf).

6.1.3. Miocene

Sample 398-U1591C-60R-1, 4 cm (786.53 mbsf), yields *Calcidiscus premacintyrei*, *Coccolithus miopelagicus*, and *Cyclicargolithus floridanus*, which define Zone MNN6 (12.57–13.60 Ma; NN6/CN5a/CNM8). Sample 68R-4, 83–85 cm (868.085 mbsf), which includes *C. premacintyrei*, *C. floridanus*, and *Sphenolithus macintyrei* without *Helicosphaera ampliaperta*, defines Zone MNN5 (13.60–14.86 Ma; NN5/CN4/CNM7).

6.2. Foraminifera

Planktonic and benthic foraminifera were examined in core catcher samples and split core samples from Holes U1591A–U1591C (Tables **T8**, **T9**). Absolute ages assigned to biostratigraphic datums follow those listed in Table **T6** in the Expedition 398 methods chapter (Kutterolf et al., 2024). Planktonic and benthic foraminifer datums for Site U1591 are given in Table **T6**. Planktonic foraminifer abundances and indications of oceanicity (e.g., Hayward et al., 1999) and benthic foraminifer paleowater depths estimations are shown in Figures **F29** and **F30**.

Because of the volcanogenic nature of the cored sedimentary sequence, residues (>125 μm) from washed samples were often significantly composed of volcaniclastic particles such as pumice, scoria, and ash that often diluted the microfossil component of residues. Foraminifera dominated the biogenic component of residues, however, and age markers were present in sufficient numbers to date most samples reliably. In addition to volcanic material, clastic grains, minor pyrite, carbonaceous plant-derived matter, and other fossil material including shells and fragments (Bivalvia and Gastropoda), Pteropoda, Scaphopoda, Bryozoa, Arthropoda (*Balanus*), echinoid spines and plate fragments, radiolarians, and ostracods, as well as fish teeth, are also present in variable amounts in most samples. In addition, reworked Pliocene foraminifera are often present.

Throughout the section, foraminifera with very good to poor preservation are present in siliciclastic and volcaniclastic sediments. However, where present, foraminifera found in evaporitic and siliciclastic sediments from Samples 398-U1591C-58R-2, 89–91 cm, to 70R-CC, 0–2 cm (769.38–892.11 mbsf), were very rare and exhibited very poor preservation. Foraminifer abundances are also highly variable, commonly making up the primary sedimentary component in nannofossil oozes and notably rare in tuffaceous oozes, likely due to sedimentary dilution, whereas coarser volcaniclastic intervals and evaporitic and siliciclastic intervals were sometimes barren altogether of biogenic material.

Table T8. Distribution of planktonic foraminifera, Site U1591. **Download table in CSV format.**

Table T9. Distribution of benthic foraminifera, Site U1591. **Download table in CSV format.**

6.2.1. Holocene to Pleistocene foraminiferal biostratigraphy

As a result of explosive volcanic events and rapid deposition of the upper sedimentary section, the base of the Holocene is not possible to assign accurately. Planktonic foraminifer assemblages from the Holocene–Pleistocene section of Holes U1591A–U1591C are mostly well preserved, with specimens rarely broken or exhibiting partially dissolved shell walls.

Holocene–Pleistocene foraminifer faunas indicate large fluctuations in relative paleowater depth and oceanicity, with highly variable planktonic abundances that range 12%–100% when foraminifera were present (Figure **F30**). The fauna is typical of Mediterranean biostratigraphic Zones MPle2–MPl5, primarily composed of *Neogloboquadrina incompta, Globigerina bulloides, Globigerina falconensis, Globigerina umbilicata, Globigerinella siphonifera, Globigerinita glutinata, Globigerinoides elongatus, Globigerinoides pyramidalis, Trilobatus trilobus* group, *Globigerinoides*

| Core, section, interval (cm)	Bottom depth CSF-A (m)	AW Planktonic (%)	OK Planktonic (%)	Planktonic mean (%)	Oceanicity	Paleowater depth (m)	
398-U1591A-							
1H-CC	3.79	47	35	41	Extra-neritic	Uppermost to upper bathyal	300-600
2H-CC	13.51	48	50	49	Extra-neritic	Uppermost to upper bathyal	300-600
3H-CC	21.59	53	60	56.5	Extra-neritic	Uppermost to upper bathyal	300-600
4H-CC	32.40	84	71	77.5	Sub-oceanic	Uppermost to upper bathyal	300-600
5H-CC	41.32	89		89	Sub-oceanic	Uppermost to upper bathyal	300-600
6H-CC	51.84	89	95	92	Open oceanic	Uppermost to upper bathyal	300-600
7H-CC	58.08	89	82	85.5	Sub-oceanic	Uppermost to upper bathyal	300-600
8H-1, 39–41	61.21	65	70	67.5	Sub-oceanic	Uppermost to upper bathyal	300-600
8H-CC	64.20	BARREN	BARREN	NA	NA	NA	NA
10H-CC	89.30		56	56	Extra-neritic	Uppermost to upper bathyal	300-600
398-U1591B-							
1H-CC	7.56	58	65	61.5	Sub-oceanic	Uppermost to upper bathyal	300-600
2H-2, 134–136	10.46	75	80	77.5	Sub-oceanic	Uppermost to upper bathyal	300-600
2H-CC	17.33	85	75	80	Sub-oceanic	Uppermost to upper bathyal	300-600
3H-CC	26.00		84	84	Sub-oceanic	Uppermost to upper bathyal	300-600
4H-4, 117–119	32.29		85	85	Sub-oceanic	Uppermost to upper bathyal	300-600
4H-CC	36.56		80	80	Sub-oceanic	Uppermost to upper bathyal	300-600
5H-CC	46.15		69	69	Sub-oceanic	Uppermost to upper bathyal	300-600
6H-CC	55.43		85	85	Sub-oceanic	Uppermost to upper bathyal	300-600
7H-5,.118–120	62.36		80	80	Sub-oceanic	Uppermost to upper bathyal	300-600
8H-CC	66.94		25	25	Outer neritic	Uppermost to upper bathyal	300-600
10F-CC	101.21		85	85	Sub-oceanic	Uppermost to upper bathyal	300-600
15X-CC	128.02	49	50	49.5	Extra-neritic	Uppermost to upper bathyal	300-600
21X-CC	175.70	74	75	74.5	Sub-oceanic	Reworked benthic	
22X-1, 117–119	186.39	79	80	79.5	Sub-oceanic	Reworked benthic	
22X-CC	194.95	87	89	88	Sub-oceanic	Reworked benthic	
23X-CC	204.57	83	87	85	Sub-oceanic	Reworked benthic	
24X-CC	207.23	78	80	79	Sub-oceanic	Uppermost to upper bathyal	300-600
25X-CC	215.10	66	60	63	Sub-oceanic	Uppermost to upper bathyal	300-600
26X-CC	225.08	83	86	84.5	Sub-oceanic	Uppermost to upper bathyal	300-600
27X-CC	233.91	90	73	81.5	Sub-oceanic	Uppermost to upper bathyal	300-600
29X-CC	253.13	67	75	71	Sub-oceanic	Uppermost to upper bathyal	300-600
30X-CC	270.70	75	75	75	Sub-oceanic	Uppermost to upper bathyal	300-600
31X-CC	282.30	69	70	69.5	Sub-oceanic	Uppermost to upper bathyal	300-600
32X-CC, 18–20	284.15	81	75	78	Sub-oceanic	Reworked benthic	
32X-CC	284.35	19	BARREN	19	NA	NA	NA
33X-CC	296.31	12	8	10	Inner neritic	Reworked	
34X-CC	301.62	86	80	83	Sub-oceanic	Reworked benthic	
35X-CC, 18–20	316.41	72	75	73.5	Sub-oceanic	Reworked benthic	
35X-CC, 38–43	316.64	27	30	28.5	Outer neritic	Reworked benthic	
36X-CC	323.23	73	67	70	Sub-oceanic	Reworked benthic	
37X-CC	338.84	60	55	57.5	Sub-oceanic	Reworked benthic	
38X-CC	344.28	52		52	Extra-neritic	Reworked benthic	
39X-CC	351.52	87	75	81	Sub-oceanic	Reworked benthic	
40X-CC	364.56	87	90	88.5	Sub-oceanic	Reworked benthic	
41X-CC	370.25	71	70	70.5	Sub-oceanic	Reworked benthic	
42X-CC	380.60	81	75	78	Sub-oceanic	Reworked benthic	
43X-CC	386.60	93	85	89	Sub-oceanic	Reworked benthic	

Figure F29. Foraminiferal oceanicity and paleowater depth estimates, Site U1591. Blue colors show relationship between oceanicity index and paleowater depth. Observers: AW = Adam Woodhouse, OK = Olga Koukousioura. NA = not applicable. (Continued on next page.)

Core, section, interval (cm)	Bottom depth CSF-A (m)	AW Planktonic (%)	OK Planktonic (%)	Planktonic mean (%)	Oceanicity	Paleowater depth (m)	
398-U1591C-							
3R-CC	158.73		65	65	Sub-oceanic	Mid to lower bathyal	600->1000
4R-CC	168.64		55	55	Extra-neritic	Mid to lower bathyal	600->1000
5R-CC	179.43		90	90	Open oceanic	Mid to lower bathyal	600->1000
6R-CC	191.83		50	50	Extra-neritic	Mid to lower bathyal	600->1000
7R-CC	205.39		71	71	Sub-oceanic	Mid to lower bathyal	600->1000
8R-CC	212.74		57	57	Extra-neritic	Mid to lower bathyal	600->1000
9R-CC	221.01		95	95	Open oceanic	Mid to lower bathyal	600->1000
11-CC	236.41		95	95	Open oceanic	Mid to lower bathyal	600->1000
12R-CC	251.56		74	74	Sub-oceanic	Mid to lower bathyal	600->1000
13R-CC	263.04		75	75	Sub-oceanic	Mid to lower bathyal	600->1000
15R-CC	351.40		83	83	Sub-oceanic	Mid to lower bathyal	600->1000
17R-CC	370.70		61	61	Sub-oceanic	Mid to lower bathyal	600->1000
19R-CC	392.51	93	75	84	Sub-oceanic	Reworked benthic	
20R-CC	404.24	88	85	86.5	Sub-oceanic	Reworked benthic	
21R-CC	414.32	92	100	96	NA	NA	NA
22R-CC	422.28	86	91	88.5	Sub-oceanic	Reworked benthic	
23R-CC	433.83	33	78	55.5	Sub-oceanic	Reworked benthic	
24R-CC	437.66	100		100	Open oceanic	NA	NA
25R-CC	452.89	100	0	50	NA	Reworked benthic	
26R-CC	462.46	100	50	75	Sub-oceanic	Reworked benthic	
27R-CC	470.29	44	55	49.5	Extra-neritic	Reworked benthic	
28R-CC	480.21	88	90	89	Sub-oceanic	Reworked benthic	
29R-CC	491.46	69	75	72	Sub-oceanic	Reworked benthic	
30R-CC	498.09	92	86	89	Sub-oceanic	Reworked benthic	
31R-CC	511.84	81	77	79	Sub-oceanic	Reworked benthic	
32R-CC	523.16	80	87	83.5	Sub-oceanic	Reworked benthic	
33R-CC	528.45	89	87	88	Sub-oceanic	Reworked benthic	
34R-CC	541.46	88	86	87	Sub-oceanic	Reworked benthic	
35R-CC	552.04	71	50	60.5	Sub-oceanic	Reworked benthic	
36R-CC	563.78	43	25	34	Extra-neritic	Reworked benthic	
37R-CC	568.19	BARREN	BARREN	NA	NA	NA	NA
38R-CC	579.60	78	80	79	Sub-oceanic	Slightly dysoxic	
39R-CC	590.59	43	32	37.5	Extra-neritic	Slightly dysoxic	
40R-CC	602.12	58	56	57	Extra-neritic	Slightly dysoxic	
41R-CC	609.90	79	72	75.5	Sub-oceanic	Slightly dysoxic	
42R-CC	612.16	58	47	52.5	Extra-neritic	Slightly dysoxic	
43R-CC	629.70	72	60	66	Sub-oceanic	Slightly dysoxic	
44R-CC	634.71	70	77	73.5	Sub-oceanic	Slightly dysoxic	
45R-CC	650.99	84	70	77	Sub-oceanic	Slightly dysoxic	
46R-CC	655.71	79	68	73.5	Sub-oceanic	Slightly dysoxic	
47R-CC	662.33	81	70	75.5	Sub-oceanic	Slightly dysoxic	
48R-CC	679.14	81	73	77	Sub-oceanic	Slightly dysoxic	
49R-CC	685.37	88	77	82.5	Sub-oceanic	NA	NA
50R-CC	699.36	BARREN	BARREN	NA	NA	NA	NA
51R-CC	708.25	90	75	82.5	Sub-oceanic	NA	NA
52R-6, 83–86	716.16	BARREN	BARREN	NA	NA	Mid to lower bathyal	600->1000
53R-CC	728.59	100	BARREN	100	Open oceanic	NA	NA
54R-CC	732.92	93	89	91	Open oceanic	Mid to lower bathyal	600->1000
55R-CC	741.38	92	89	90.5	Open oceanic	Mid to lower bathyal	600->1000
56R-CC	753.21	93	95	94	Open oceanic	Mid to lower bathyal	600->1000
57R-7, 3–5	765.63	100		100	Open oceanic	Reworked benthic	
57R-CC	767.41	94	95	94.5	Open oceanic	Reworked benthic	
58R-1, 129–131	768.41	100	99	99.5	Open oceanic	Reworked benthic	
58R-2, 13–15	768.62	100	99	99.5	Open oceanic	Reworked benthic	
58R-2, 89–91	769.38	100		100	Open oceanic	NA	NA
58R-3, 1–3	769.73	BARREN	BARREN	NA	NA	NA	NA
58R-CC	776.48	100		100	Open oceanic	NA	NA
59R-CC	785.07		BARREN	NA	NA	NA	NA
60R-1, 3–6	786.56		0			NA	NA
60R-CC	795.43		BARREN			NA	NA
61R-CC	804.93		BARREN			NA	NA
62R-CC	812.20		BARREN			NA	NA
63R-1, 132–134	816.94		BARREN			NA	NA
63R-4, 85–87	820.62		BARREN			NA	NA
66R-CC	852.99		BARREN			NA	NA
68R-1, 16–19	864.29		BARREN			NA	NA
68R-4, 83–86	868.10		BARREN			NA	NA
68R-CC	868.35		BARREN			NA	NA
69R-3, 39–42	876.47		BARREN			NA	NA
69R-CC	880.02		BARREN			NA	NA
70R-7, 76–78	891.90		BARREN			NA	NA
70R-7, 89–91	832.03		BARREN			NA	NA
70R-CC	892.11		BARREN			NA	NA

Figure F29 (continued).

ruber var. white, *G. ruber* var. pink, *Globoconella inflata*, *Hirsutella scitula*, *Truncorotalia truncatulinoides* s.l. (sinistral and dextral coiling), *Neogloboquadrina pachyderma*, *Orbulina universa*, *Turborotalita quinqueloba*, and *Globigerinella calida* through the Middle Pleistocene–Holocene, and the addition of species such as *Globoturborotalita woodi*, *Globorotalia bononiensis*, *Globigerinoides obliquus*, *Globigerinoides extremus*, and *Neogloboquadrina atlantica* (sinistral) through the Lower Pleistocene (Figures **F31**, **F32**). Rare reworked Pliocene specimens are found throughout the Holocene–Pleistocene interval.
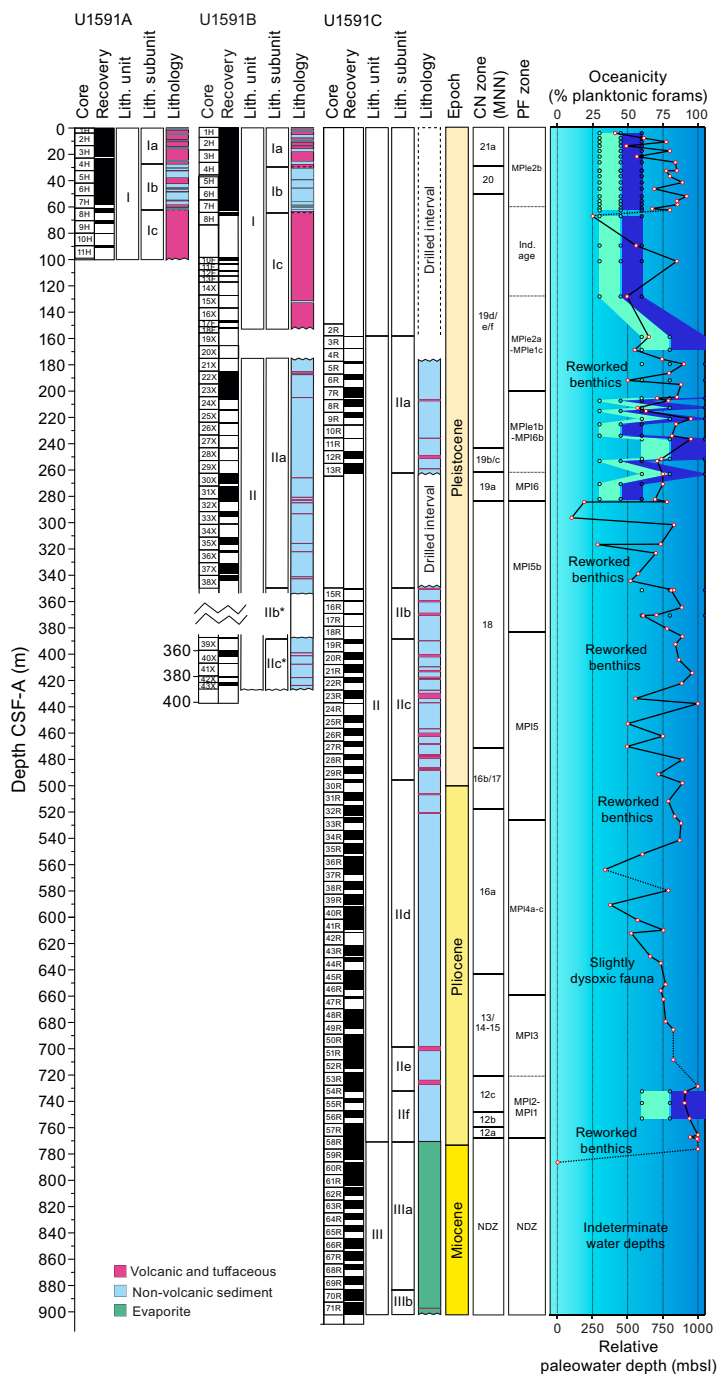
Figure F30. Biostratigraphic summary, Site U1591. CN = calcareous nannofossil, MNN = Mediterranean Neogene Nannoplankton, PF = planktonic foraminifer. Interpreted oceanicity (Hayward et al., 1999): solid line/red points = interpreted oceanicity, dashed line = extrapolation through barren/unreliable sample data. Interpreted paleowater depths: light blue points/shading = shallower paleowater depth interpretation, dark blue points/shading = deeper paleowater depth interpretation. * = depth and recovery affected by slumped material.

Foraminiferal faunas are sufficiently common to biostratigraphically divide the Pleistocene into the majority of Mediterranean planktonic foraminiferal biostratigraphic zones determined via both primary and secondary marker species (Lirer et al., 2019), separated by several sedimentary hiatus:

- Zone MPle2b (0.00–0.53 Ma), Hole U1591A: 3.79–58.08 mbsf.
- Zones MPle1c–2a (0.53–1.21 Ma), Hole U1591B: 128.02–204.57 mbsf.
- Zones MPle1b–MPl6b (1.21–2.00 Ma), Hole U1591B: 207.23–253.13 mbsf.
- Zone MPl6 (2.00–2.09 Ma), Hole U1591B: 270.7–282.3 mbsf.
- Zone MPl5b (2.09–2.41 Ma), Hole U1591B: 284.15–364.56 mbsf.

The faunal criteria for age assignments are given below.

6.2.1.1. Zone MPle2b (0.00–0.53 Ma)

Samples 398-U1591A-1H-CC, 54–59 cm, to 7H-CC, 0–5 cm (3.79–58.08 mbsf), are assigned to Zone MPle2b based on the paracme top of sinistrally coiled *Neogloboquadrina* spp. (<0.51 Ma) in Sample 8H-1, 39–41 cm (61.21 mbsf), above which this species is common but sporadically present through sediments. Furthermore, the first occurrence of *G. ruber* var. pink (<0.33 Ma) occurs in Sample 33H-CC, 17–20 cm (21.59 mbsf).
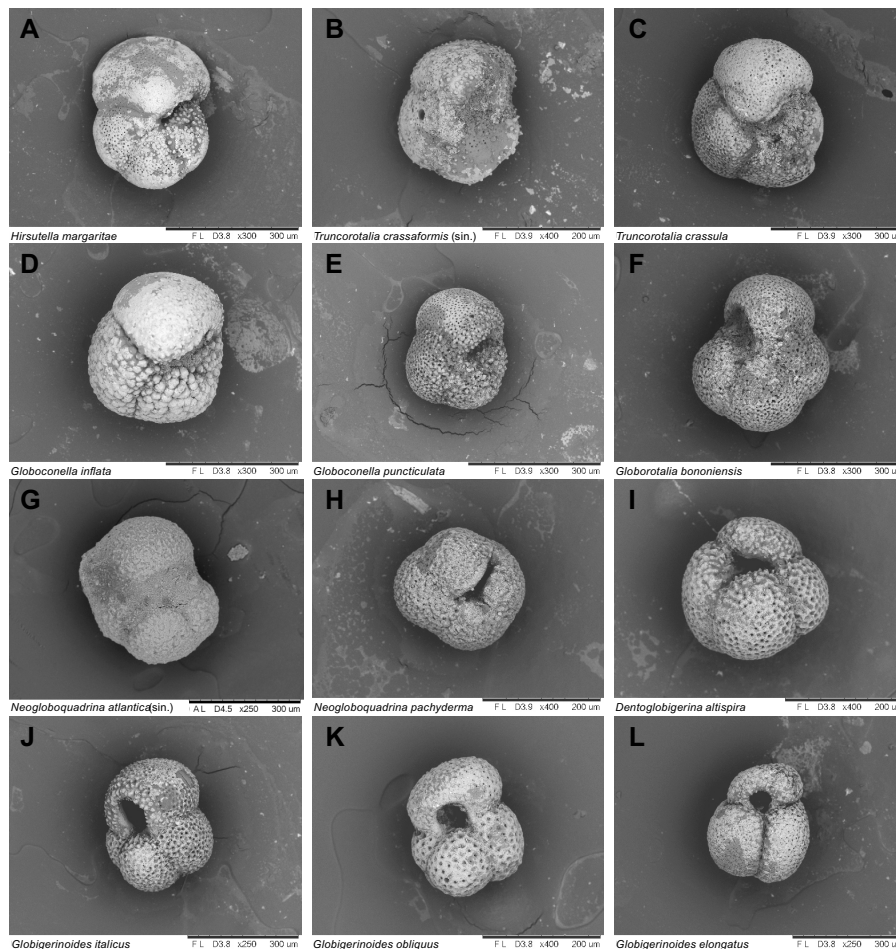
Figure F31. Planktonic foraminifera, Site U1591. A. *Hirsutella margaritae*. B. *Truncorotalia crassaformis* (sinistral) (398-U1591C-20R-CC, 10–15 cm). C. *Truncorotalia crassula* (398-U1591B-32X-CC, 37–40 cm). D. *Globoconella inflata* (1H-CC, 20–23 cm). E. *Globoconella puncticulata*. F. *Globorotalia bononiensis* (398-U1591C-31R-CC, 19–21 cm). G. *Neogloboquadrina atlantica* (sinistral) (398-U1591B-42X-CC, 0–3 cm). H. *Neogloboquadrina pachyderma* (398-U1591A-7H-CC, 24–27 cm). I. *Dentoglobigerina altispira*. J. *Globigerinoides italicus* (398-U1591C-48R-CC, 0–4 cm). K. *Globigerinoides obliquus* (56R-CC, 8–10 cm). L. *Globigerinoides elongatus*. (A, L: 47R-CC, 0-2 cm; E, I: 45R-CC, 23-25 cm).

6.2.1.2. Zone MPle2a–1c (0.53–1.21 Ma)

Samples 398-U1591B-15X-1, 117–119 cm, to 23X-CC, 34–38 cm (128.02–204.57 mbsf), are assigned to Zones MPle2a–1c based on the common occurrence of sinistrally coiled *Neogloboquadrina* spp. (0.91–1.21 Ma). Because of the consistent occurrence of sinistrally coiled *Neogloboquadrina* spp., the base of Zone MPle2a (0.91 Ma) could not be assigned and is likely missing because of the extensive and potentially erosive overlying pumice deposits of Lithostratigraphic Subunit Ic.

6.2.1.3. Zones MPle1b–MPl6b (1.21–2.00 Ma)

Samples 398-U1591B-24X-CC, 38–41 cm, to 29X-CC, 0–3 cm (207.23–253.13 mbsf), are assigned to Zones MPle1b–MPl6b based on the top occurrence of well-preserved and morphologically advanced specimens of *G. obliquus* (last occurrence = 1.28 Ma) alongside rare sinistrally coiled *Neogloboquadrina* spp. (1.21–1.37 Ma) throughout the top part of this interval. The base of this zone is assigned based on the first common occurrence of *G. inflata* (1.99 Ma) in Sample 29X-CC, 0–3 cm (253.13 mbsf), which was used in place of the primary biostratigraphic marker for this zone in the Mediterranean Sea (Lirer et al., 2019), the first occurrence of *T. truncatulinoides* (2.00 Ma), a species that is comparably rare in the Aegean Sea. Additionally, Sample 24X-CC (207.23 mbsf) marks the first common occurrence of the benthic foraminifer *Hyalinea balthica* (1.492 Ma; Lourens et al., 1998).

6.2.1.4. Zone MPl6 (2.00–2.09 Ma)

Samples 398-U1591B-30X-CC, 39–44 cm, to 31X-CC (270.7–282.3 mbsf) are assigned to Zone MPl6 because it represents the interval from the first occurrence of *G. inflata* (2.09 Ma) and the first common occurrence of *G. inflata* (2.00 Ma).

6.2.1.5. Zone MPl5b (2.09–2.41 Ma)

Samples 398-U1591B-32X-CC, 18–20 cm, to 40X-CC, 0–3 cm (284.15–364.56 mbsf) are assigned to Zone MPl5b based on the absence of *G. inflata* and the last occurrence of *N. atlantica* (sinistral) (2.41 Ma) in Sample 41X-CC, 18–22 cm (370.25 mbsf).
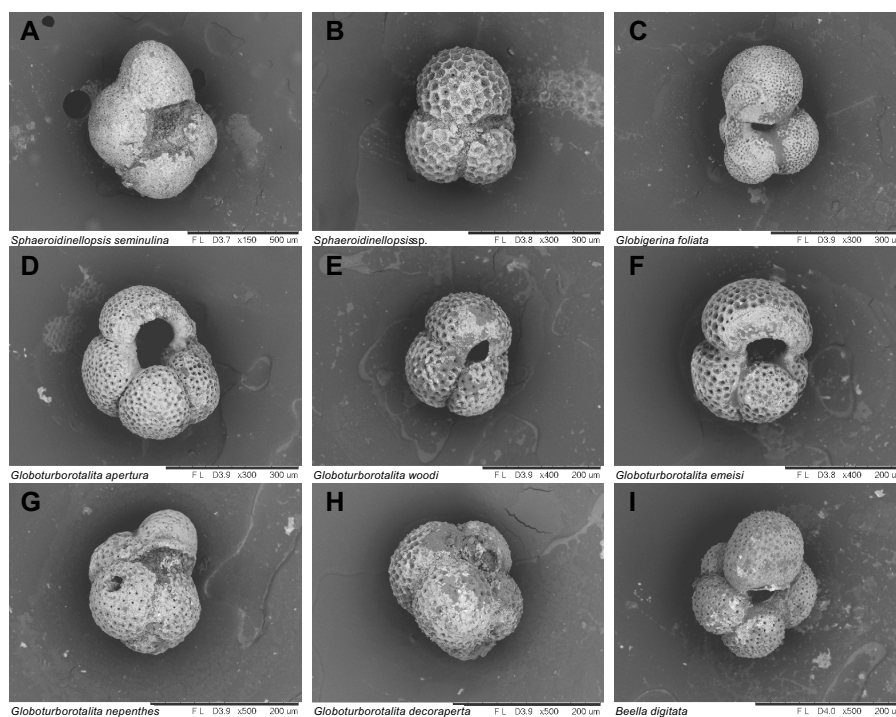
Figure F32. Planktonic foraminifera, Hole U1591C (unless otherwise specified). A. *Sphaeroidinellopsis seminulina* (56R-CC, 8–10 cm). B. *Sphaeroidinellopsis* sp. (38R-CC, 67–69 cm). C–F. 47R-CC, 0–2 cm: (C) *Globigerina foliata*; (D) *Globoturborotalita apertura*; (E) *Globoturborotalita woodi*; (F) *Globoturborotalita emeisi*. G. *Globoturborotalita nepenthes* (55R-CC, 0–3 cm). H. *Globoturborotalita decoraperta* (45R-CC, 23–25 cm). I. *Beella digitata* (398-U1591A-7H-CC, 24–27 cm).

6.2.2. Pliocene foraminiferal biostratigraphy

Planktonic foraminifer assemblages from the Pliocene section of Hole U1591C are mostly well preserved; specimens are rarely broken or exhibit partially dissolved shell walls.

Pliocene foraminifer faunas indicate large fluctuations in relative paleowater depths and oceanicity with highly variable planktonic abundances that range 33%–100% where foraminifera are present (Figure F30). The fauna is typical of Mediterranean biostratigraphic Zones MPl5–NDZ, primarily composed of *N. incompta*, *G. bulloides*, *G. falconensis*, *G. glutinata*, *G. elongatus*, *T. trilobu*s group, *G. ruber* var. white, *N. pachyderma*, *O. universa*, and more typical Pliocene species such as *G. obliquus*, *G. extremus*, *Globoturborotalita decoraperta*, *Sphaeroidinellopsis* s.l., *Globoconella puncticulata*, *Hirsutella margaritae*, and *Truncorotalia crassula* (Figures F31, F32).

Foraminiferal faunas are sufficiently common to biostratigraphically divide the Pliocene into the majority of Mediterranean planktonic foraminiferal biostratigraphic zones determined via both primary and secondary marker species (Lirer et al., 2019), which are separated by several sedimentary hiatus:

- Zone MPl5 (2.41–3.19 Ma), Hole U1591C: 392.51–523.16 mbsf.
- Zones MPl4a–4c (3.19–3.98 Ma), Hole U1591C: 528.45–655.71 mbsf.
- Zone MPl3 (3.98–4.52 Ma), Hole U1591C: 662.33–708.25 mbsf.
- Zones MPl2–MPl1 (4.52–5.33 Ma), Hole U1591C: 732.92–768.62 mbsf.
- Nondistinctive Zone (5.33–5.99 Ma), Hole U1591C: 769.38–892.11 mbsf.

The faunal criteria on which these age assignments are based are given in the sections below.

6.2.2.1. Zone MPl5 (2.41–3.19 Ma)
Samples 398-U1591C-19R-CC, 0–4 cm, to 32R-CC, 21–23 cm (392.51–523.16 mbsf), are assigned to Zone MPl5 based on the rare to common occurrences of *G. bononiensis* (last common occurrence = 2.41 Ma) and the absence of *Sphaeroidinellopsis* s.l. (last occurrence = 3.19 Ma). Additionally, the last common occurrence of *G. obliquus* (2.54 Ma) occurs in Sample 29R-CC, 0–2 cm (491.46 mbsf).

6.2.2.2. Zones MPl4c–4a (3.19–3.98 Ma)
Samples 398-U1591C-33R-CC, 14–17 cm, to 46R-CC, 13–16 cm (528.45–655.71 mbsf), are assigned to biostratigraphic Zones MPl4c–4a based on the last occurrence of *Sphaeroidinellopsis* s.l. (3.19 Ma) in Sample 33R-CC, 14–17 cm (528.45 mbsf), and the absence of common occurrence of *H. margaritae* (last common occurrence = 3.98 Ma). Additionally, typical specimens of *G. ruber* occur at the base of this interval; the last occurrence of *H. margaritae* (3.81 Ma) was found in Sample 45R-CC, 23–25 cm (650.99 mbsf); and the last occurrence of *G. puncticulata* (3.57 Ma) was found in Sample 40R-CC, 18–20 cm (602.12 mbsf). However, *G. puncticulata* is reported to occur consistently and abundantly through its range in the Mediterranean (Lirer et al., 2019) and is only sporadically present at the Aegean Expedition 398 sites; therefore, this datum can only tentatively be used to constrain the boundary between Zones MPl4 and MPl4b.

6.2.2.3. Zone MPl3 (3.98–4.52 Ma)
Samples 398-U1591C-47R-CC, 0–2 cm, to 51R-CC, 25–30 cm (662.33–708.25 mbsf), are assigned to Zone MPl3 based on the top common occurrence of *H. margaritae* (3.98 Ma) in Sample 47R-CC, 0–2 cm (662.33 mbsf); the absence of *Globoturborotalita nepenthes* (last occurrence ~4.6 Ma); and the presence of typical specimens of *G. elongatus*. Because of the presence of significant sediment remobilization from 700 to 715 mbsf, the base of this zone is difficult to accurately assign.

6.2.2.4. Zones MPl2–MPl1 (4.52–5.33 Ma)
Samples 398-U1591C-54R-CC, 39–42 cm, to 58R-2, 13–15 cm (732.92–768.62 mbsf), are assigned to Zones MPl2–MPl1 based on the last occurrence of *G. nepenthes* (~4.6 Ma) in Sample 54R-CC, 39-42 cm (732.92 mbsf), and the absence of normal marine planktonic foraminiferal assemblages in sediments deeper than Sample 58R-2, 89–91 cm (768.62 mbsf). The lower part of this sedimentary section also contains higher abundances of *G. nepenthes* and *Globoturborotalita apertura*; rare occurrences of the species *Globoturborotalita emeisi*; the acme of *Sphaeroidinellopsis* s.l.

(5.21–5.3 Ma) in Sample 56R-CC, 8–10 cm (753.21 mbsf); and the first occurrence of *Siphonina reticulata* (5.234 Ma) (Lourens et al., 2004) in Sample 58R-1, 129–131 cm (768.41 mbsf). The boundary between Zones MPl2 and MPl1 could not be accurately assigned because the boundary marker species (first common occurrence of *H. margaritae*; 5.08 Ma) is only continuously present in pelagic successions (Lirer et al., 2019).

6.2.2.5. Nondistinctive Zone (5.33–5.99 Ma)

Samples 398-U1591C-58R-2, 89–91 cm, to 70R-CC, 0–2 cm (769.38–892.11 mbsf), are assigned to the Nondistinctive Zone due to absence of normal marine planktonic foraminiferal assemblages, and, where present, faunas are dwarfed and exhibit very poor preservation.

6.2.3. Planktonic foraminiferal oceanicity

Planktonic foraminifer abundances are highly variable, ranging 12%–100% when foraminifera were present. Oceanicity values are generally in agreement with benthic foraminiferal paleowater depth indicators in intervals where reworking is low or absent (Figure **F30**). In general, the oceanicity data for Site U1591 indicate that relatively consistent suboceanic conditions (200–1000 mbsl) prevailed from Samples 398-U1591A-1H-CC, 11–16 cm, to 398-U1591B-32X-CC, 18–20 cm (3.79–284.15 mbsf). Samples 32X-CC, 37–40 cm, to 38X-CC, 37–40 cm (284.35–344.28 mbsf), indicate large fluctuations in oceanicity from suboceanic (200–1000 mbsl) to inner neritic (0–50 mbsl) conditions, where Sample 33X-CC, 43–45 cm (296.31 mbsf), records the lowest oceanicity values (12% planktonic foraminifera) recorded downhole so far (Figure **F30**). Samples 39X-CC, 31–36 cm, to 398-U1591C-34R-CC, 19–24 cm (313.52–541.46 mbsf), then indicate generally suboceanic conditions (200–1000 mbsl) downhole, after which values once again fluctuate between extraneritic (100–200 mbsl) and suboceanic in Samples 35R-CC, 14–16 cm, to 42R-CC, 0–2 cm (552.04–612.16 mbsf). Downhole from Sample 42R-CC, 0–2 cm, planktonic foraminifera indicate increasing oceanicity, consistently indicating open oceanic conditions from Samples 53R-CC, 21–24 cm, to 58R-CC, 18–20 cm (728.59–776.48 mbsf), below which foraminifera are not present in abundances sufficient for oceanicity interpretations.

6.2.4. Benthic foraminifera paleowater depths

Benthic foraminiferal distributions are variable, indicating paleowater depths from uppermost bathyal (200–400 m) to lower bathyal (>1000 m) (Figure **F30**). The low abundances or complete absence of benthic foraminiferal faunas in some samples (e.g., 398-U1591B-32X-CC, 37–40 cm [284.35 mbsf], and 398-U1591C-19R-CC, 0–4 cm, to 36R-CC, 22–24 cm [392.51–563.78 mbsf]) are possibly correlated with rapid emplacement of volcaniclastic sediments and/or inhospitable environmental conditions. Samples from Hole U1591A (3.8–89.3 mbsf) and Samples 398-U1591B-1H-CC, 20–23 cm, to 15X-CC, 15–18 cm (7.56–128.02 mbsf), record an uppermost to upper bathyal depth (300–600 m), as indicated by the presence of species such as *Cibicides pachyderma* and *Gyroidina* spp., *Cassidulina* spp., and *H. balthica*. Samples 398-U1591C-3R-CC, 0–2 cm, to 17R-CC, 0–2 cm (158.73–370.7 mbsf), and 54R-CC, 39–42 cm, to 56R-CC, 8–10 cm (732.92–753.21 mbsf), exhibit mid- to lower bathyal paleowater depths, as indicated by the presence of *Oridorsalis umbonatus*, whereas lower bathyal markers including *Cibicidoides wuellerstorfi* and *C. mundulus* also occur (Figures **F30**, **F33**). Additionally, samples in various intervals present broken and reworked foraminifer faunas and in some cases abundant specimens, as in Samples 29R-CC, 0–2 cm (491.46 mbsf), and 36R-CC, 22–24 cm (563.78 mbsf), which likely represent downslope reworking and sediment transportation (Figure **F30**). For Samples 39R-CC, 0–2 cm, to 48R-CC, 0–4 cm (590.59–679.14 mbsf), no paleowater depth estimation was possible because of the dominance of dysoxic-tolerant species such as *Bolivina dilatata* and *Bulimina costata* (e.g., Abu-Zied et al., 2008), most possibly representing intervals with high organic matter content.
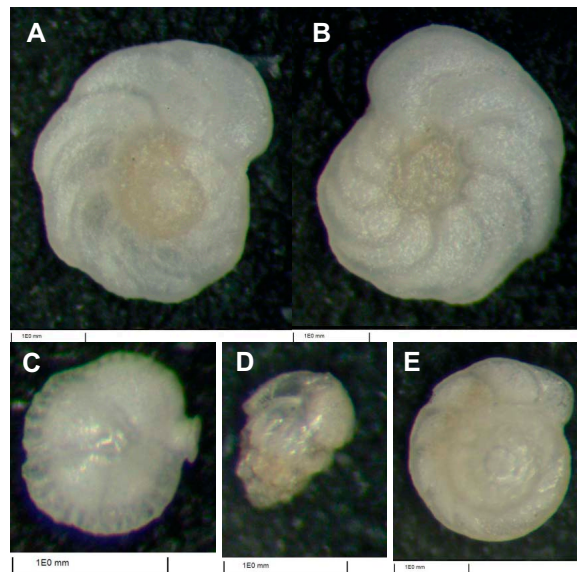
Figure F33. Benthic foraminifera, Hole U1591C. A, B. *Cibicidoides wuellerstorfi* (8R-CC, 14–16 cm); (A) umbilical view; (B) spiral view. C. *Siphonina reticulata* (13R-CC, 14–16 cm). D. *Bulimina costata* (39R-CC, 0–2 cm). E. *Cibicidoides mundulus* (9R-CC, 9–12 cm).

7. Paleomagnetism

Paleomagnetic analyses at Site U1591 focused on measurement and demagnetization of archive-half sections to determine magnetostratigraphic age controls. The uppermost 63 m of the sequence sampled at this site carries normal polarity remanences acquired during the Brunhes Chron. Scattered inclinations then prevent magnetostratigraphic correlations from ~185 to 480 mbsf. From 480 to 770 mbsf, however, the quality of data improves and eight reversal boundaries can be tied precisely to the geomagnetic polarity timescale (within the Pliocene), with a further four tentative correlations also possible. Data in the Messinian evaporite sequence sampled deeper than 771 mbsf are less conclusive. Some intervals display reversed polarities consistent with formation during Chron C3r (5.235–6.023 Ma; Gradstein et al., 2020), but other intervals appear to be contaminated by a strong drilling-induced overprint with steep positive inclinations.

7.1. Bulk magnetic properties

The bulk magnetic parameters of intensities of magnetization and low-field MS typically have log-normal (geometric) distributions in natural samples (Tarling, 1983). Table **T10** provides the geometric means and ranges of these parameters observed at the same measurement points in archive-half sections for all three holes cored at Site U1591, whereas the histograms of Figure **F34** show their overall distributions for the entire site (plotted as $\log_{10}$ values). Both parameters show positive skew, reflecting dominance of measurements made in weakly magnetic sediments and sedimentary rocks.

7.2. Downhole variations in magnetic characteristics

Remanence measurements were made on archive-half sections recovered during Expedition 398 by APC, XCB, and RCB coring in Holes U1591A–U1591C using the 2G Enterprises Model 760R-4K superconducting rock magnetometer (SRM) system. Remanences were measured every 2 cm and were filtered to reject data from points within 8 cm of section ends. This produced a dataset consisting of natural remanent magnetization (NRM) and alternating field (AF) demagnetization data (after applied field steps of 15, 20, and 25 mT) measured at 18,271 intervals downhole. Point MS data obtained from the archive-half sections were also filtered to preserve only data corresponding to the intervals where remanence measurements were made. In addition, 119 discrete

samples were subject to AF demagnetization in maximum applied fields of up to 50–100 mT (in some cases up to 200 mT) to help constrain magnetic polarities.

Downhole variations in magnetic properties are shown in Figures **F35**, **F36**, and **F37** for Holes U1591A, U1591B, and U1591C, respectively. Declinations of magnetizations are azimuthally unconstrained and show wide variations between cores, as expected. Inclinations are observed to become shallower than the NRM directions following demagnetization, reflecting removal of a ubiquitous drilling-induced remanent magnetization (DIRM). Variations in inclinations fall into three zones: (1) interval 0–63 mbsf, inclinations are consistently positive and close to the expected value of 56° for the site; (2) interval 185–480 mbsf, inclinations are widely scattered but with a bias toward steep values >56° (these variations may reflect a combination of residual DIRM components and/or the effects of diagenetic alteration); and (3) a zone below 480 mbsf that exhibits systematic variations between normal and reversed inclinations. The significance of these data for magnetostratigraphic dating is discussed below. Median destructive fields (MDFs) throughout the sampled sequence are typically 10–15 mT, indicating a dominance of low-coercivity magnetic minerals, but some intervals (e.g., 680–820 mbsf; Figure **F37**) display higher MDFs, suggesting

Table T10. NRM intensity and MS, Site U1591. **Download table in CSV format.**
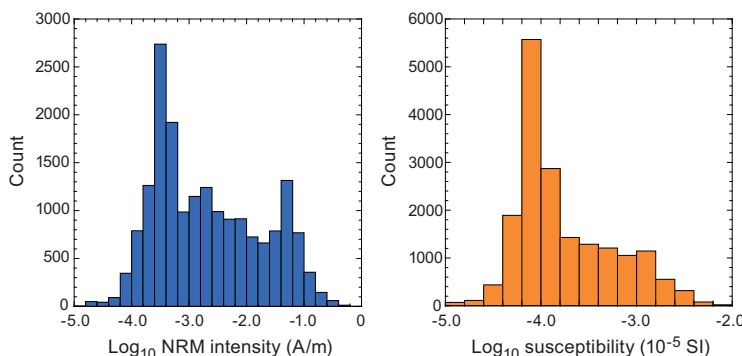
Figure F34. Histograms of NRM intensity and low-field MS, Site U1591. Data are based on archive-half section SRM measurements and low-field point MS measurements made at the same intervals downhole.
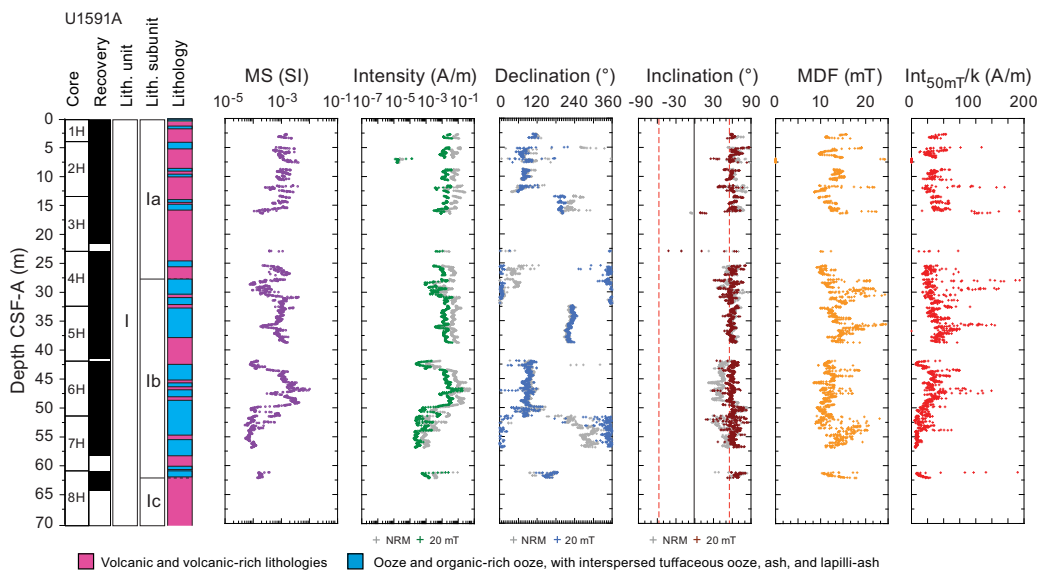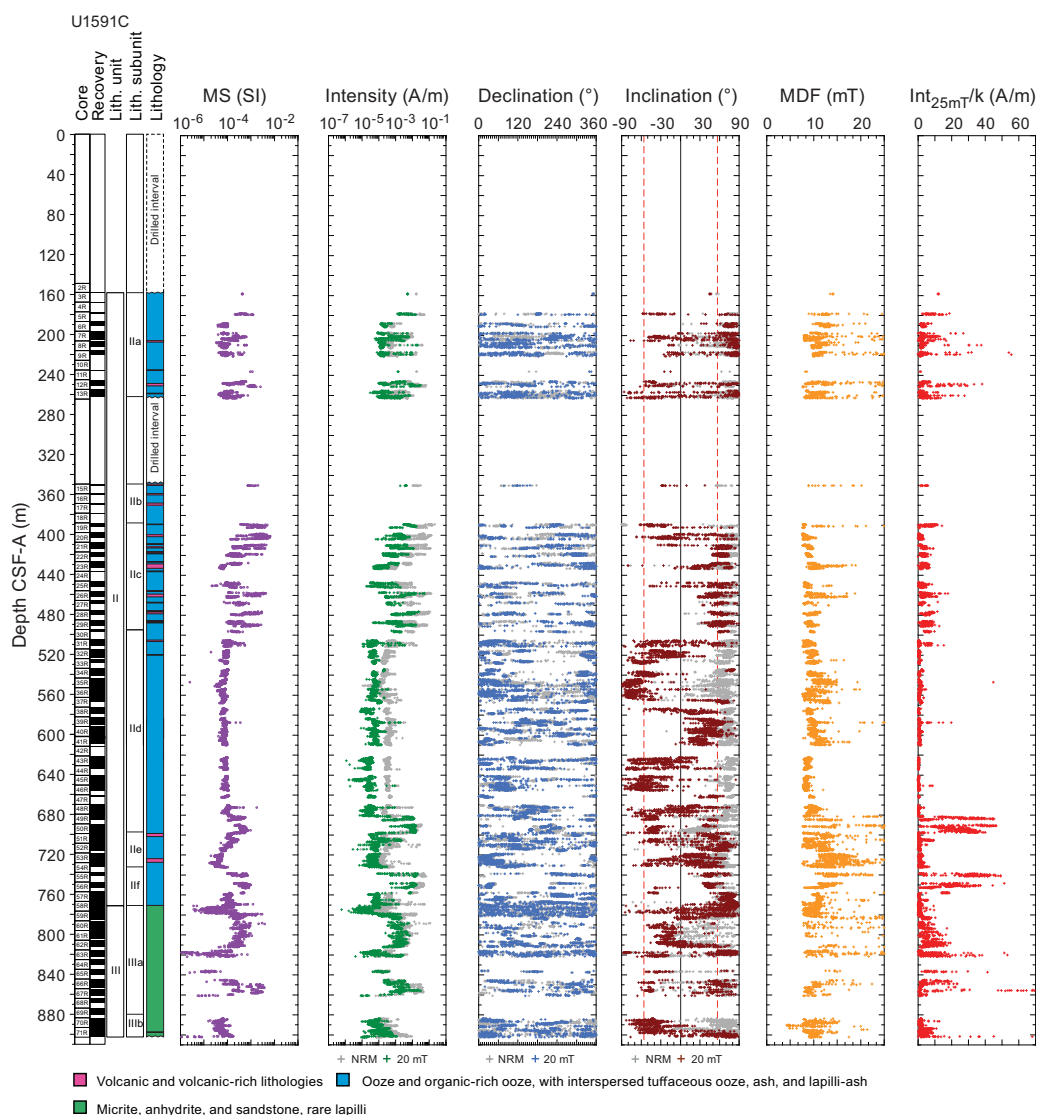

Figure F35. Archive-half section magnetic data, Hole U1591A. Red dashed lines = geocentric axial dipole inclinations expected at this site.

presence of higher coercivity carriers. Samples in these intervals often display only minor directional and intensity variations after treatment at 15 mT, and analysis of discrete samples indicated that even demagnetization in applied fields of 50–200 mT results in limited changes in intensity. These characteristics suggest that magnetic remanence is carried by hematite (in addition to a magnetite signal overprinted by DIRMs) with high coercivities (Kletetschka and Wieczorek, 2017).

We employed an automated principal component analysis (PCA) approach to analyze archive-half section data acquired at higher AF demagnetization steps to identify samples displaying linear decay toward the origin during demagnetization (see **Paleomagnetism** in the Site U1589 chapter [Druitt et al., 2024]). This involved comparing free-fitting and anchored PCA directions through the 15, 10, and 25 mT step remanences calculated with PuffinPlot software and accepting only those free-fitting PCAs with maximum angular deviations <15° that differ by <15° from the corresponding anchored PCAs. The resulting PCA data set represents the highest quality inclination estimates obtained in each of the three holes sampled at Site U1591. We also observed a significant number of samples that displayed only minor decay in intensity after removal of the drilling-induced magnetization and only minor variation in magnetization directions at higher steps. These samples carry stable magnetizations that cannot be demagnetized using the SRM system but still provide valuable information about magnetic polarity. To extract inclination data from such samples, we also calculated the Fisher mean directions of the remanences measured at each interval downhole after demagnetization at 15, 20, and 25 mT. For samples where no valid PCA was found, we accepted those Fisher mean directions with precision parameters >15 and α_{95} cones
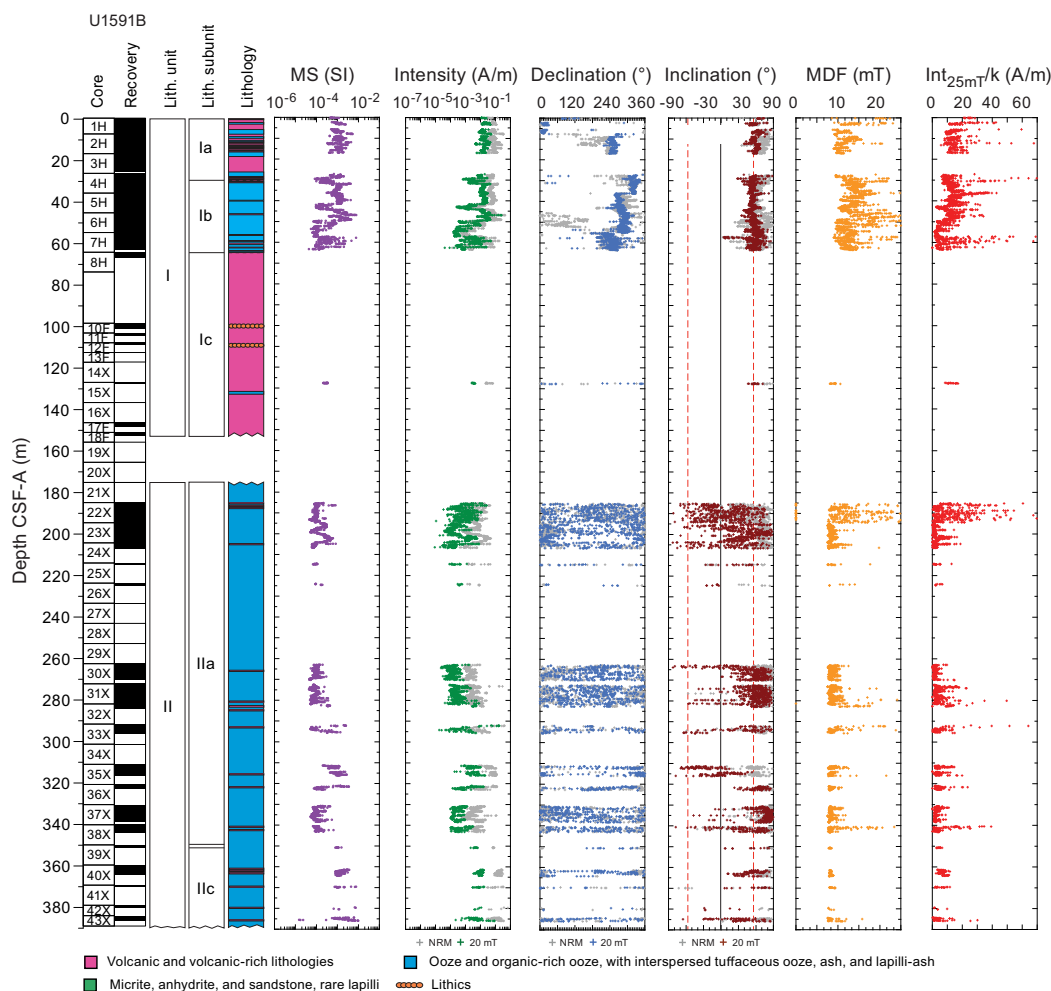
Figure F36. Archive-half section magnetic data, Hole U1591B. Red dashed lines = geocentric axial dipole inclinations expected at this site.

of confidence <15°. Samples that yielded neither statistically acceptable PCAs or Fisher mean directions were represented in the final site database by their 25 mT step inclinations. The combination of these three different estimates of inclinations downhole was then used to define magnetozones.

7.3. Correlations with the geomagnetic polarity timescale

Variations in inclination with depth after combining data from all three holes into a single record (divided by quality) are shown in Figure **F38**. The highest quality PCA directions down to 63 mbsf have a mean inclination of 53.4° (k = 42.5; $α_{95}$ = 1.0; n = 2908). This agrees well with the geocentric axial dipole field inclination of 56° at Site U1591, confirming that the interval 0–63 mbsf carries a normal polarity magnetization acquired in the Brunhes Chron.

Inclinations at 185–480 mbsf vary widely and are considered unreliable for magnetostratigraphic interpretation. This interval is biostratigraphically dated to 1.28–2.51 Ma (see **Biostratigraphy**), spanning Chrons C1r.3r–C2r.2r, where the geomagnetic field had a reversed polarity apart from two short normal subchrons at 1.775–1.934 Ma (C2n) and 2.120–2.155 Ma (C2r.1n) (Gradstein et al., 2020). The presence of samples with both normal and reversed polarity with no systematic
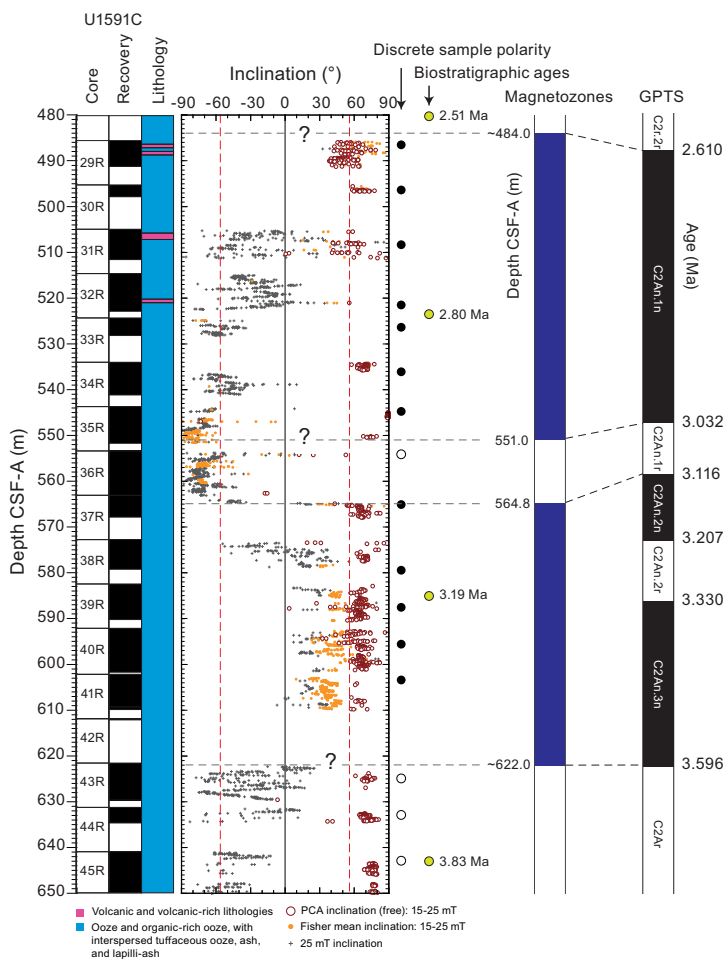

Figure F37. Archive-half section magnetic data, Hole U1591C. Red dashed lines = geocentric axial dipole inclinations expected at this site.

distribution in this interval therefore suggests that the record is affected by variable diagenetic alteration and the growth of new magnetic mineral assemblages (see **Paleomagnetism** in the Site U1589 chapter [Druitt et al., 2024]).

Inclinations in the interval 480–770 mbsf show systematic variations with depth that define eight clear reversals that may be correlated with confidence to the geomagnetic polarity timescale (Gradstein et al., 2020) on the basis of both archive-half section and discrete sample data. Inclination data for this interval are shown in detail in Figures **F39** and **F40**, and examples of both archive-half section and discrete sample demagnetization data across these reversal events are shown in Figure **F41**. A downhole change from reversed to normal polarity at 564.8 mbsf (Figure **F39**) lies between biostratigraphic markers for 2.80 and 3.19 Ma and must therefore represent the base of Chron C2An.1r at 3.116 Ma (see **Biostratigraphy**). The remaining seven clear reversals (Figure **F40**) occur below a biostratigraphic marker for 3.98 Ma and are tied to the bases of Chrons C2Ar–C3n.3r (see **Biostratigraphy**). The assignment of interval 707.2–753.0 mbsf (Cores 398-U1591C-52R to 55R) to Chron C3n.3n (Figure **F40**) implies a period of very rapid deposition (45.8 m in 97 ka). An additional four tentative correlations may also be made (flagged by question marks in Figures **F39**, **F40**) but should not be used in the age model for the site.
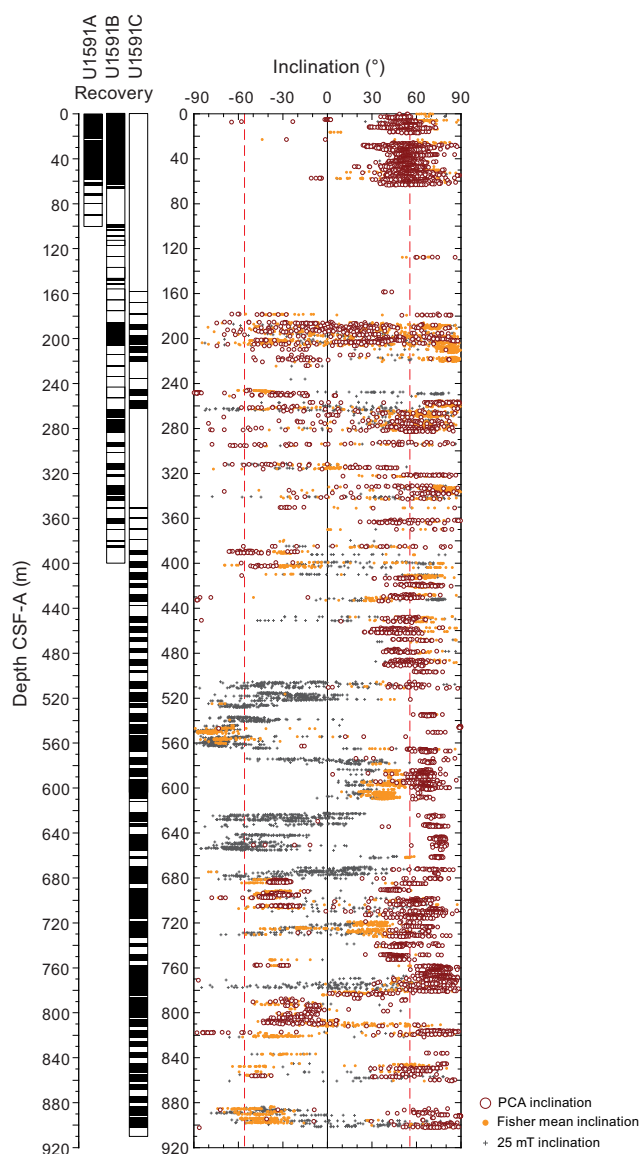
Figure F38. Archive-half section magnetic inclinations, Site U1591. Red dashed lines = geocentric axial dipole inclinations expected at this site.

The Messinian evaporite sequence sampled below 771 mbsf shows large variations in inclination estimates including several intervals with positive PCA inclinations that are steeper than the expected value at this site and some intervals with negative Fisher mean inclinations. These variations in apparent polarity are not considered reliable for magnetostratigraphic purposes, however, because the well-established age of the Messinian evaporites (5.96–5.33 Ma; Krijgsman et al., 2007) falls entirely within reversed Chron C3r (Gradstein et al., 2020).

7.4. Anisotropy of low-field magnetic susceptibility

Anisotropy of magnetic susceptibility was measured on 106 discrete samples from Site U1591 (Figure **F42**). The distribution of the majority of sample minimum principal susceptibility (k_{min}) axes is subvertical with subhorizontal girdle distributions of intermediate (k_{int}) and maximum (k_{max}) axes. Corrected anisotropy degrees, P_J, reach maximum values of 1.14 (i.e., 14% anisotropy), but the majority of samples have moderate anisotropies of ~1.01–1.06. Shape parameters are mainly positive, indicating dominance of oblate anisotropy ellipsoids. These distributions are characteristic of primary depositional fabrics with k_{min} principal axes oriented normal to bedding.

Figure F39. Archive-half section magnetic inclinations for 480–650 mbsf, Hole U1591C. Data are used to define magnetozones that are correlated to the geomagnetic polarity timescale (GPTS) of Gradstein et al. (2020). Red dashed lines = geocentric axial dipole inclinations expected at this site. Solid/open circles = normal/reversed polarity of discrete samples.
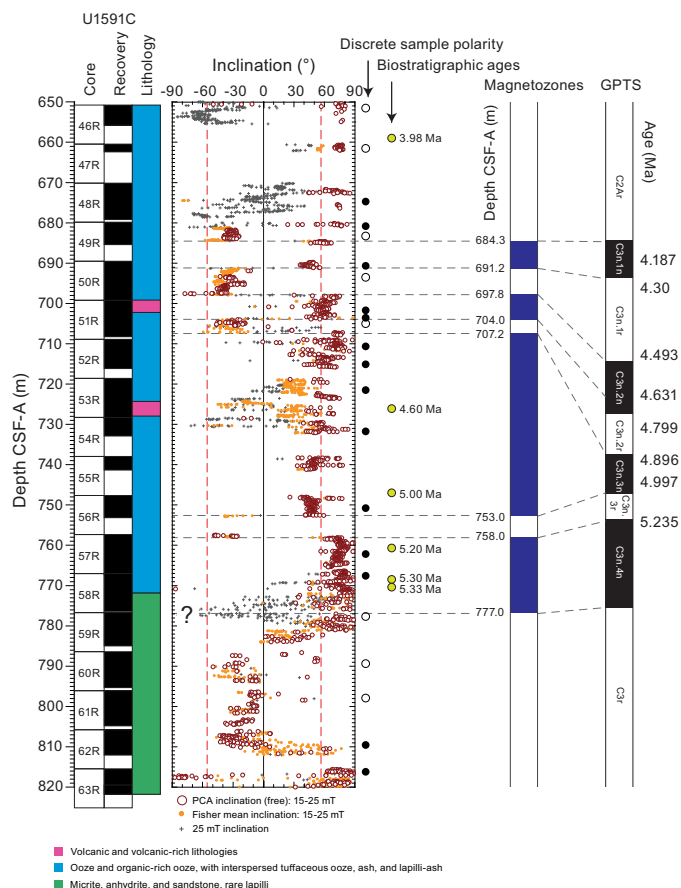
Figure F40. Archive-half section magnetic inclinations for interval 650–820 mbsf, Hole U1591C. Data are used to define magnetozones that are correlated to the geomagnetic polarity timescale (GPTS) of Gradstein et al. (2020). Red dashed lines = geocentric axial dipole inclinations expected at this site. Solid/open circles = normal/reversed polarity of discrete samples.
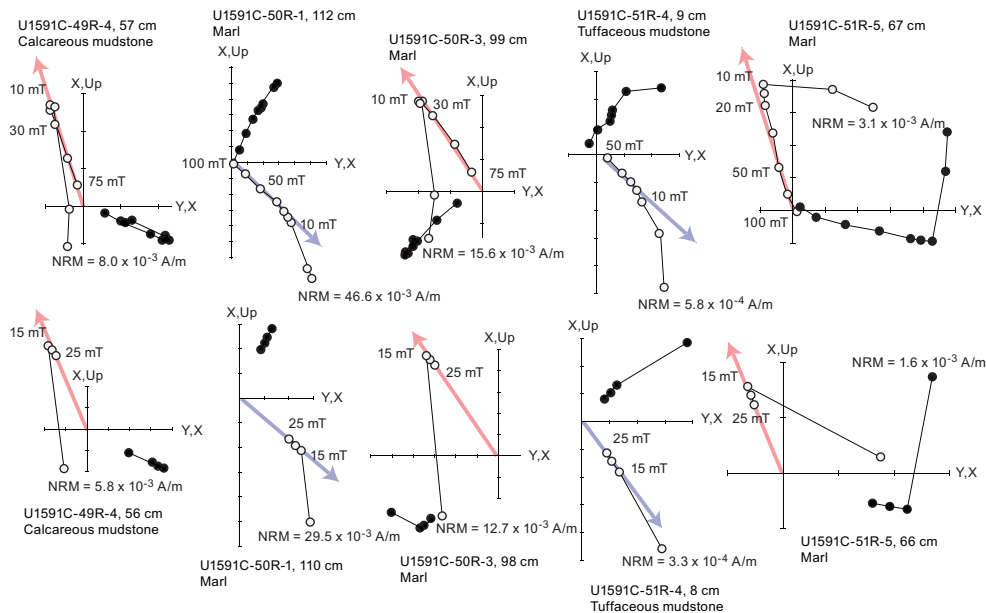
Figure F41. AF demagnetization of discrete samples (top) and archive-half sections (bottom), Site U1591. The series of reversals shown in Figure F40 are documented. Red/blue arrows = reversed/normal polarity inclinations, solid circles = projection onto horizontal plane, open circles = projection onto vertical plane.
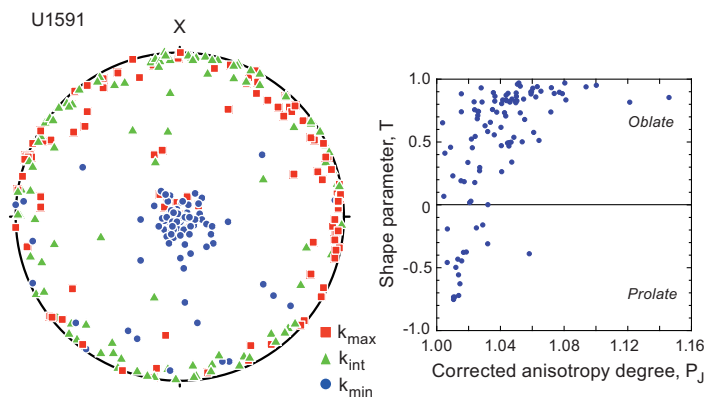
Figure F42. Discrete sample anisotropy of low-field magnetic anisotropy, Hole U1591C. Left: lower hemisphere stereographic equal-area projections of principal anisotropy axes (min = minimum, int = intermediate, max = maximum). Right: shape parameter plotted against corrected anisotropy degree (Jelínek and Kropáček, 1978).

8. Physical properties

Physical properties at Site U1591 correlate with lithology. Thick volcaniclastic layers in Lithostratigraphic Unit I (ash, lapilli-ash, and lapilli) sometimes have low grain densities (<2.0 g/cm^3) in coarse, pumice-rich subunits. Volcaniclastic deposits also exhibit large variations in MS and often have high MS compared to other sediments at this site. High-MS anomalies are most abundant and largest in amplitude at depths shallower than 490 mbsf (downhole through Core 398-U1591C-29R). Unit II, which is dominated by nannofossil-rich oozes, often displays cyclic variations in NGR that correlate with organic-rich layers. The anhydrite layers of Unit III have much higher *P*-wave velocity, thermal conductivity, and bulk density and lower NGR than the surrounding sediments.

8.1. Whole-round GRA density, MS, *P*-wave velocity, and NGR

Figure **F43** summarizes data collected on whole-round cores measured using the GRA densitometer, MS loop, and *P*-wave logger on the WRMSL and NGR. There are a few possible systematic sources of error in these data that should be considered when interpreting absolute values and trends.

- Redistribution of unconsolidated volcaniclastic materials in core liners during coring and on the core retrieving platform can lead to sorting by particle size and density and hence changes in physical properties.
- During XCB and RCB coring, recovered cores can contain cracks and void space around the cored materials that lower the values of all physical property measurements made on whole-round cores.
- Whole-round measurements in sections that match discrete measured values on split cores are thus most reliable. Note that whole-round *P*-wave velocity data were not collected for RCB cores because the cored materials do not fill the core liner.

MS variability is high in the volcaniclastic deposits at this site. These variations arise from differences in relative abundance of ferromagnetic minerals. For example, volcaniclastic Lithostratigraphic Subunit Ia (see **Lithostratigraphy**) in the uppermost 30 m has MS values as high as 1000 × 10^{-5} to 2000 × 10^{-5} SI and values of ~1500 × 10^{-5} SI in intervals that contain tuffaceous sand (360–364 mbsf in Hole U1591B) and lithic crystal ash with cobbles (volcanic slump deposit of Subunit IIb Cores 398-U1591C-16R and 17R; 360–370 mbsf). Figure **F44** illustrates correlations between lithology and physical properties including MS in Cores 398-U1591B-2H and 3H. Overall, at this site, MS anomalies are most pronounced and occur most abundantly to 490 mbsf (Core 398-U1591C-29R). Large MS peaks occur again in Unit III below 770 mbsf, beginning in Core 58R (Figure **F43**).

NGR measurements on whole-round core sections show (at least qualitatively) cyclic variations that are most clear in Unit II at 400–680 mbsf (Cores 398-U1591C-20R through 48R). Variations are often correlated with the presence of organic-rich lithologies, as shown in Figure **F45** (see **Lithostratigraphy**). NGR measurements on whole-round core sections of Cores 70R and 71R (883–903 mbsf) show distinctive increases in total counts to >150 counts/s from values <40 counts/s at shallower depths (Figure **F43**).
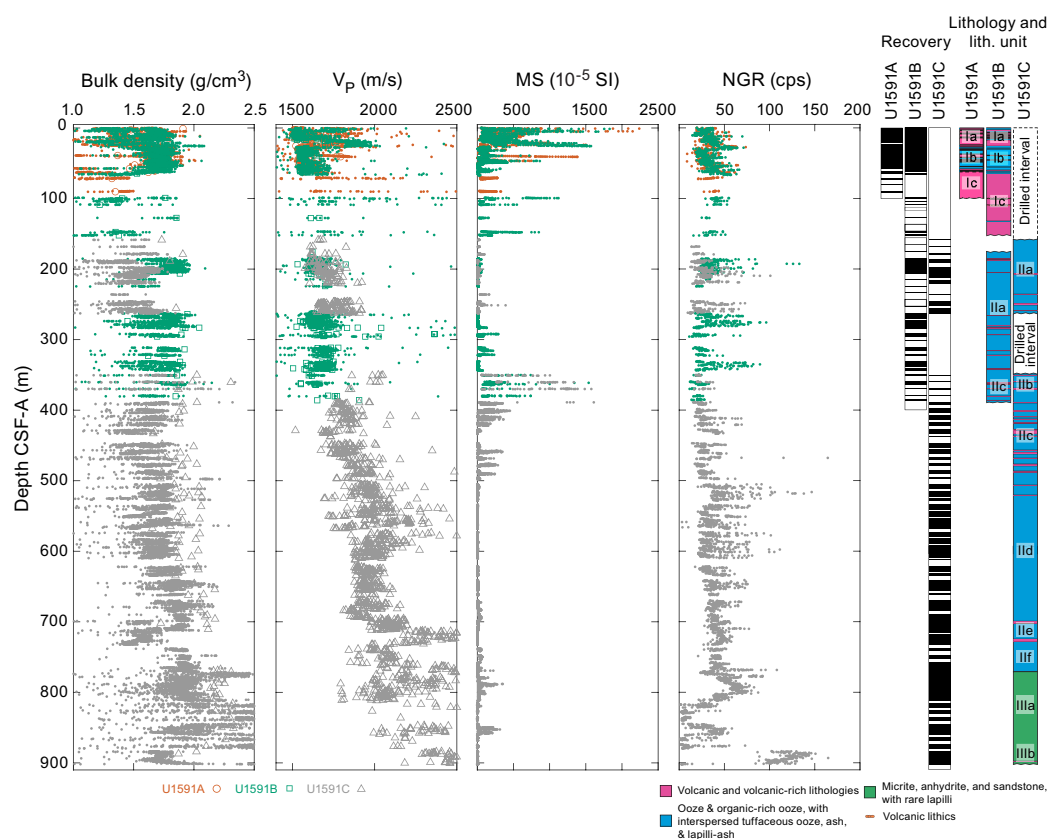
8.2. Discrete measurements

8.2.1. Material strength

Sediment strength was measured with a pocket penetrometer (PP) on the catwalk immediately after section splitting. Automated vane shear (AVS) strength measurements were made on working-half sections. Totals of 14 and 33 AVS measurements were made on working-half sections from 5 to 61 mbsf in Hole U1591A and from 3 to 380 mbsf in Hole U1591B, respectively (Figure **F46**; Table **T11**). Samples in the uppermost 100 m with shear strengths too low to be measured might be a consequence of disturbance during recovery. A total of 21 PP measurements were made on fine-grained materials that remained intact in core liners upon recovery on the catwalk (Table **T11**). No measurements were made in Hole U1591C during RCB coring because the recovered material was too stiff or was already crumbling during splitting of core sections. Figure **F46** shows that shear strength increases as a function of depth to 400 mbsf, and below this depth the fine-grained sediment became too stiff to be measured.

8.2.2. *P*-wave velocity

Totals of 119, 209, and 1534 *P*-wave velocity measurements were conducted on Hole U1591A, U1591B, and U1591C working-half sections, respectively. The discrete measurements of *P*-wave


Figure F43. Physical properties, Site U1591. Dots = whole-round measurements, open symbols = discrete sample measurements. Samples with bulk density and *P*-wave velocity greater than the maximum values on the x-axes are plotted in Figure F46. cps = counts per second.

velocity follow the trend observed in WRMSL measurements on whole-round cores (Figures **F43**, **F46**; Table **T12**); *P*-wave velocity increases with depth, which is expected as sediments compact. Discrete measurements are more reliable and have less scatter than WRMSL measurements because the calipers measure the *P*-wave velocity of cored materials in direct contact, whereas the WRMSL measures material within core liners that contain water pockets, fractures, and other gaps that are ubiquitous in the XCB and RCB cores that dominated drilling at this site. Note that discrete *P*-wave velocity measurements of cores with severe biscuiting drilling disturbance may be
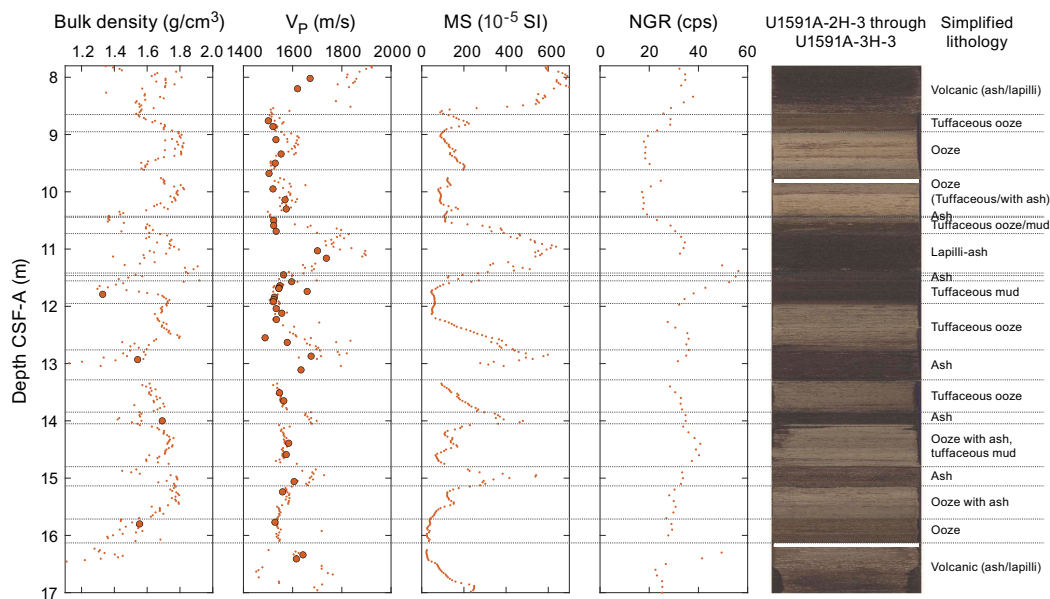
Figure F44. Relationships between lithology and physical properties, Hole U1591A. The top and bottom NGR measurements are removed from each section because the values are affected by edges of sections. White bars on image = void space where IW samples were collected. cps = counts per second.
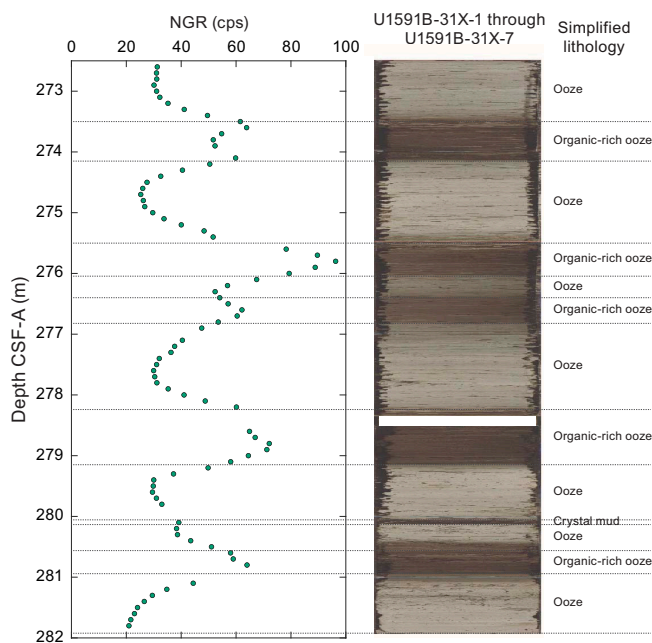
Figure F45. Relationships between NGR and lithology, Hole U1591B. The top and bottom NGR measurements are removed from each section because the values are affected by edges of sections. White bar on images = void space where IW samples were collected. cps = counts per second.

affected by soft material that likely originated from the drilling disturbance of the formation and is found between the coherent core pieces and the underlying core liner. Measurements were not made where biscuiting disturbance was clear.

Volcaniclastic materials in Lithostratigraphic Unit I have *P*-wave velocities of ~1.5–1.7 km/s. Typical *P*-wave velocity of the oozes in Unit II increases with depth from ~1.7 km/s at the top of Unit II to ~2.1 km/s at its base. A best-fit to measurements from Holes U1591B and U1591C for Unit II (160–700 mbsf; a total of 1070 discrete measurements) gives

$$\text{velocity } (z) = (1.564 \pm 0.022) + (0.716 \pm 0.060)z \text{ km/s,}$$

where *z* is in kilometers and reported ± values are standard errors. Unit III has highly variable *P*-wave velocity (Figure **F46**) with evaporite velocities that can exceed 5.0 km/s, whereas the background sediments have values similar to those of the overlying deposits of Unit II (2.1–2.8 km/s).

8.2.3. Moisture and density

A total of 217 discrete samples were collected to conduct moisture and density (MAD) measurements (Figure **F46**; Table **T13**). Bulk density derived by MAD measurements on discrete samples should be more reliable than GRA data from WRMSL measurements on whole-round cores.

Porosity ranges 3–79 vol% (mean = 45 vol%; standard deviation = 15 vol%). Bulk density ranges 1.2–2.9 g/cm³ and is lowest in volcaniclastic materials with high porosity. Grain density ranges 1.6–3.0 g/cm³ (mean = 2.68 g/cm³; median = 2.76 g/cm³), with the low values primarily in volcaniclastic subunits in the uppermost 150 m. The evaporites of Lithostratigraphic Unit III have grain densities >2.9 g/cm³, consistent with anhydrite-dominated lithologies (anhydrite mineral density = 2.96 g/cm³). A few low grain densities (<2.4 g/cm³) are found in between anhydrite-dominated
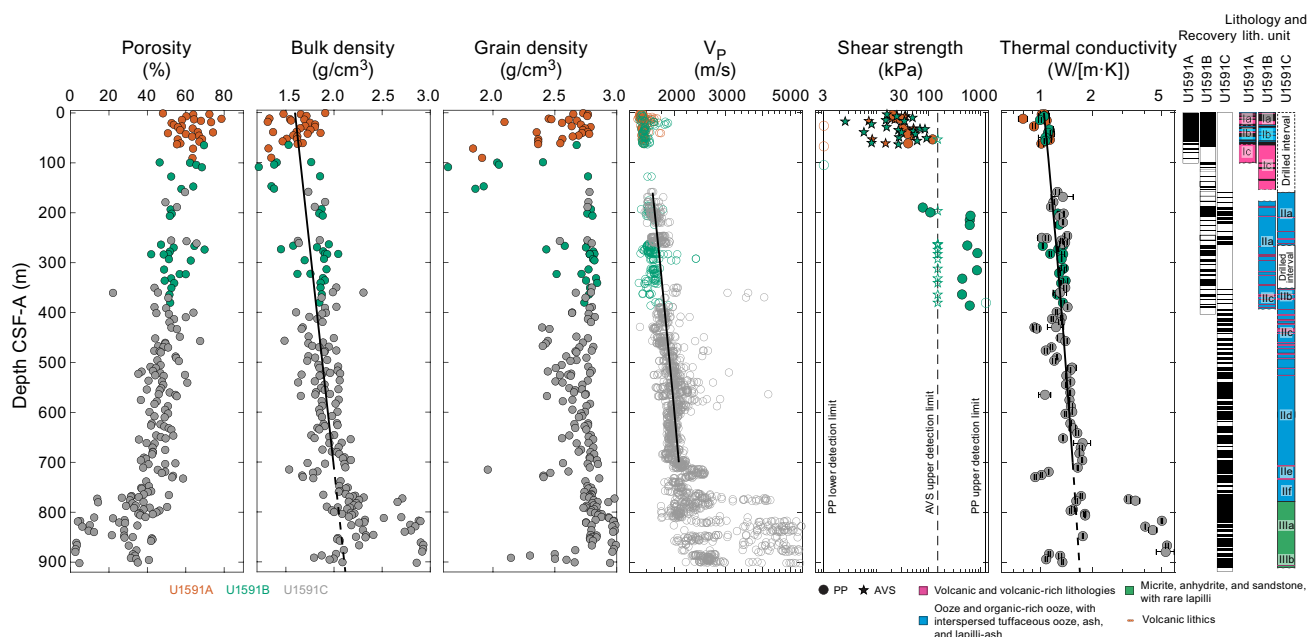
Figure F46. Discrete physical property measurements, Site U1591. Sediment below shear strength measurements shown was too stiff for measurement. Solid curves = linear least-squares best fits to the data, dashed lines = extrapolations.

Table T11. Shear strength, Site U1591. **Download table in CSV format.**

Table T12. *P*-wave velocity, Site U1591. **Download table in CSV format.**

Table T13. MAD measurements, Site U1591. **Download table in CSV format.**

Table T14. Thermal conductivity, Site U1591. **Download table in CSV format.**

lithologies in Unit III. Excluding the evaporites of Unit III, bulk density increases with depth. A least-squares fit of bulk density data from Units I and II in the uppermost 700 m is

$$\rho(z) = (1.595 \pm 0.025) + (0.569 \pm 0.061)z \text{ g/cm}^3,$$

where z is in kilometers and reported ± values are standard errors.

8.2.4. Thermal conductivity

A total of 101 thermal conductivity measurements were made on selected working-half sections, typically 1–2 per core (Table **T14**). Overall, thermal conductivity increases with increasing depth (Figure **F46**), as expected from the compaction of the sediments. The anhydrite-dominated lithologies of Unit III have much higher thermal conductivities (4–5 W/[m·K]) than sediments at the same depths (1–2 W/[m·K]). A least-squares linear fit to the thermal conductivity data for the uppermost 700 m (hence omitting the high values from anhydrite in Unit III) is

$$k(z) = (1.03 \pm 0.02) + (0.89 \pm 0.12)z \text{ W/(m·K)},$$

where z is in kilometers and reported ± values are standard errors, with large scatter about the trend.

9. Geochemistry

9.1. Volcaniclastic bulk geochemistry

To determine the geochemistry of the volcanic and tuffaceous materials, 22 tephra samples were handpicked from various layers in Holes U1591A–U1591C. Following cleaning, grinding, fusion, and dissolution, the materials were analyzed shipboard for major (Si, Al, Fe, Mg, and Ca), minor (Ti, Mn, Na, K, and P), and trace (Sc, V, Cr, Co, Ni, Cu, Zn, Rb, Sr, Y, Zr, Nb, Ba, Ce, and Nd) elements using inductively coupled plasma–atomic emission spectroscopy (ICP-AES) (see **Geochemistry** in the Expedition 398 methods chapter [Kutterolf et al., 2024] for analytical technique). Several unknown samples were run multiple times to determine analytical reproducibility.

9.1.1. ICP-AES: major, minor, and trace elements

Of the volcaniclastic units sampled, 3 were classified as basaltic andesites or basaltic trachyandesites, 4 as andesites or trachyandesites, 13 as dacites or trachydacites, and 2 as rhyolites (Table **T15**; Figure **F47**). Bulk chemistry values are less evolved than glass chemistry reported in Kutterolf et al. (2021), as expected due to bulk analyses including both minerals and glass.

Concentrations are reported for all analyzed trace elements, but Ce, Cr, Cu, Nb, Ni, P, Rb, S, and V were below detection limits in the majority of samples and are not shown for respective samples in Table **T15**; volcaniclastic analytical errors are ±1% for major elements and ±5%–10% for trace elements (see **Geochemistry** in the Expedition 398 methods chapter [Kutterolf et al., 2024]). Trace element ratios were used to broadly discriminate between the volcanic centers of Kolumbo, Santorini, and Christiana.

9.2. Interstitial water geochemistry

To determine the inorganic constituents of IW, a total of 55 water samples were taken from the mudline and whole-round squeezing of sediment intervals in Holes U1591A (10 samples), U1591B (12 samples), and U1591C (33 samples). Aliquots of IW were used for shipboard analyses, and the remaining water was taken for shore-based analysis following protocols specified by individual scientists. The retrieved pore waters were analyzed shipboard for salinity, alkalinity, pH, major anions (Cl^-, SO_4^{2-}, and Br^-), major cations (Ca^{2+}, Na^+, Mg^{2+}, and K^+), and major (S, Ca, Mg, K, and Na) and minor (B, Ba, Fe, Li, Mn, P, Si, and Sr) elements using the methods described in **Geochemistry** in the Expedition 398 methods chapter (Kutterolf et al., 2024).
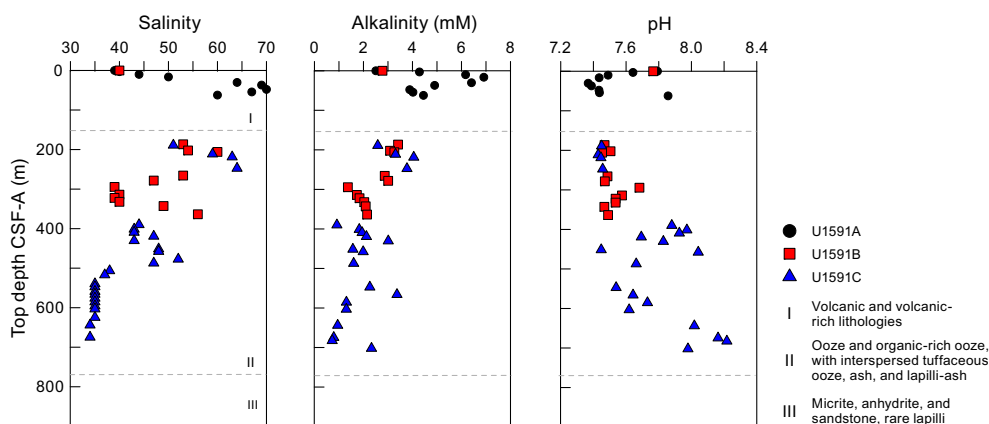
9.2.1. Salinity, alkalinity, and pH

Total IW salinities range 35–70 throughout the hole; most values are 35–60 (Table **T16**; Figure **F48**). The highest salinity values of 70, 56, 64, and 52, which caused four local maxima, were recorded in Sections 398-U1591A-6H-4, 398-U1591B-40X-3, 398-U1591C-12R-2, and 28R-1, respectively. Salinities <39 may be related to pore water freshening from dehydration of clays at depth or during the squeezing procedure.

Table T15. ICP-AES data for major, minor, and trace elements, Site U1591. **Download table in CSV format.**
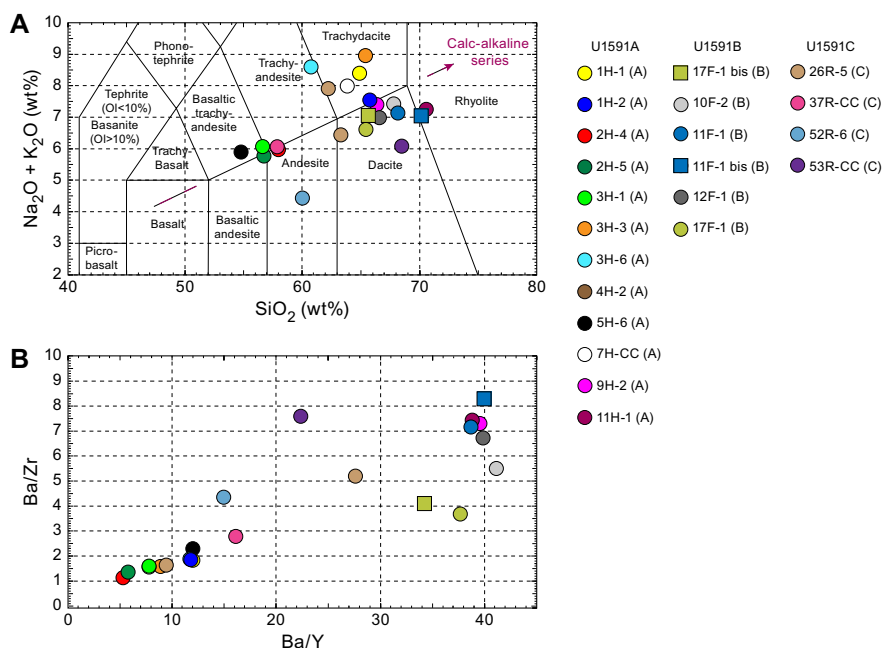
Figure F47. ICP-AES analyses of selected volcaniclastic units used to discriminate between potential volcanic sources, Site U1591. A. Total alkali vs. SiO_2 plot with the rock nomenclature of Le Maitre et al. (2002) overlain used for sample naming. Ol = olivine. B. Ba/Y vs. Ba/Zr plot used to correlate samples following Kutterolf et al. (2021).

Table T16. Alkalinity, pH, and salinity, Site U1591. **Download table in CSV format.**

Figure F48. IW salinity, alkalinity, and pH, Site U1591. Dashed lines = unit boundaries.

Total alkalinity increases from 2.5 mM at the seafloor to a maximum of ~7 mM at 16 mbsf. In general, alkalinity decreases with depth below this maximum, aside from elevated values of 4.1, 3.0, and 3.4 mM at 219, 430, and 566 mbsf, respectively (Table **T16**; Figure **F48**).

Values for pH show some variation in the sampled depths, ranging 7.4–8.2 (average = 7.8 ± 0.1). Higher pH was recorded in deeper samples.

9.2.2. Bromide, chloride, boron, sodium, potassium, magnesium, calcium, and sulfate

Bromide, Cl^-, B, Na^+, K^+, Mg^{2+}, Ca^{2+}, and SO_4^{2-} all follow similar trends to salinity and reach maxima in the same samples as salinity (except B and Ca^{2+}, which are slightly higher in the sample from the core above) (Table **T17**; Figure **F49**). These maxima occur mainly in lithologies dominated by calcareous ooze (see **Lithostratigraphy**); however, alteration of intercalated volcanic material may be supplying these elements to the pore fluids (Schacht et al., 2008). Between 500 and 650 mbsf, SO_4^{2-} drastically decreases and has near-zero values before increasing again to the bottom of the hole. This trend is similar in the other elements, most prominently in K^+ and Ca^{2+}.

9.2.3. Lithium, strontium, manganese, barium, and silicon

Trends for Li, Sr, Mn, Ba, and Si do not strongly correlate with lithologic units (Table **T17**; Figure **F50**). Lithium and Sr follow largely similar trends with depth: an initial increase with depth, a decrease to minima near 450 mbsf, and an increase to maxima at 625 and 585 mbsf, respectively.

Table T17. IW data for major anions and cations measured using ion chromatography and major and minor elements measured using ICP-AES, Site U1591. **Download table in CSV format.**
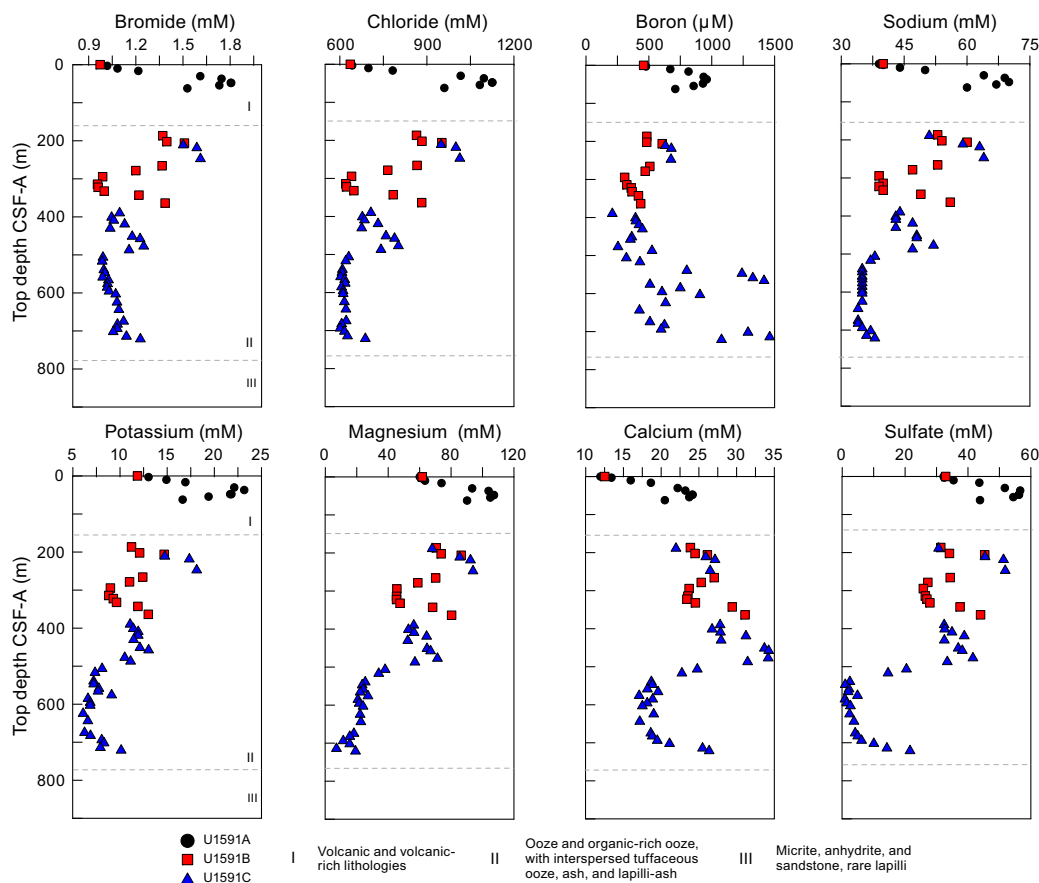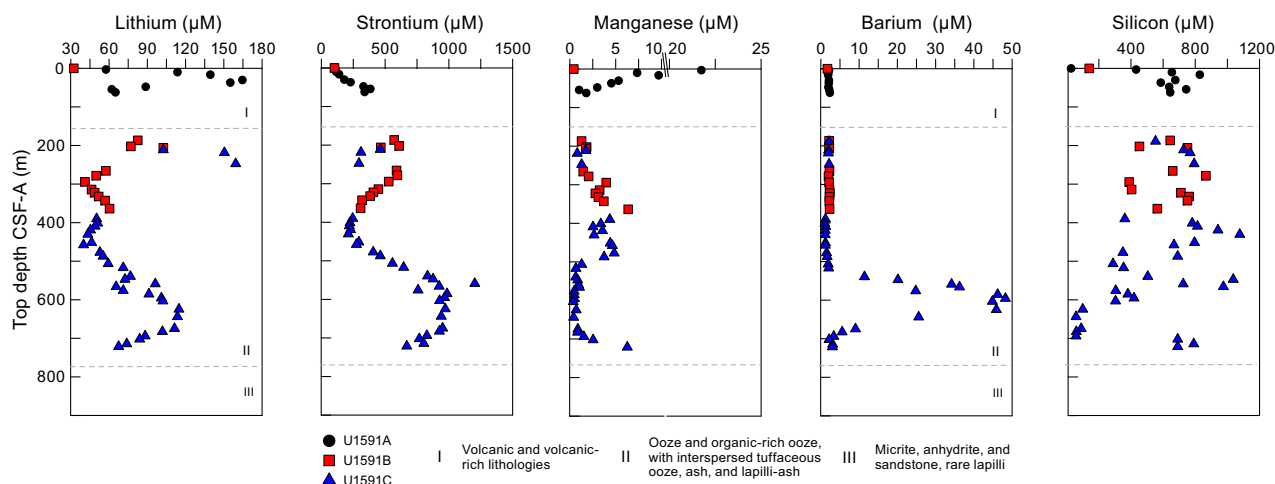

Figure F49. IC and ICP-AES concentrations of Br, Cl, B, Na, K, Mg, Ca, and SO_4^{2-} in IW samples, Site U1591. Dashed lines = unit boundaries.

Pore water Mn concentration is highest at the surface and increases again beginning at 300 mbsf. Between 500 and 700 mbsf, pore water Mn is near zero, which corresponds to the peaks in Li, Sr, and Ba. Barium is near zero except for a peak of 48 µM between 500 and 700 mbsf, also corresponding to the lowest values for SO_4^{2-}. Silicon values show no obvious trends. Iron and phosphorus are not plotted because most or all samples had concentrations below the detection limit. However, most samples with detectable Fe values are in the uppermost 63 m and reach concentrations as high as 66 µM.

9.3. Sediment bulk geochemistry

A total of 101 sediment samples were analyzed for bulk geochemistry (Table **T18**). Of these, 100 were analyzed for total carbon, hydrogen, and nitrogen (CHN) and 100 were analyzed for inorganic carbon and carbonate content following the protocols explained in **Geochemistry** in the Expedition 398 methods chapter (Kutterolf et al., 2024). For the CHN analysis, duplicates were run on ~10% of the samples to determine analytical reproducibility. Highest carbonate values are noted in the interval 186–693 mbsf, reaching values of 71 wt%, corresponding to Lithostratigraphic Unit II, which is dominated by calcareous oozes (Figure **F51**). We note a slight decrease in

Figure F50. ICP-AES concentrations of Li, Sr, Mn, Ba, and Si in IW samples, Site U1591. Dashed lines = unit boundaries.

Table T18. Total inorganic carbon, percent CaCO₃, TC, TN, and TOC data, Site U1591. **Download table in CSV format.**
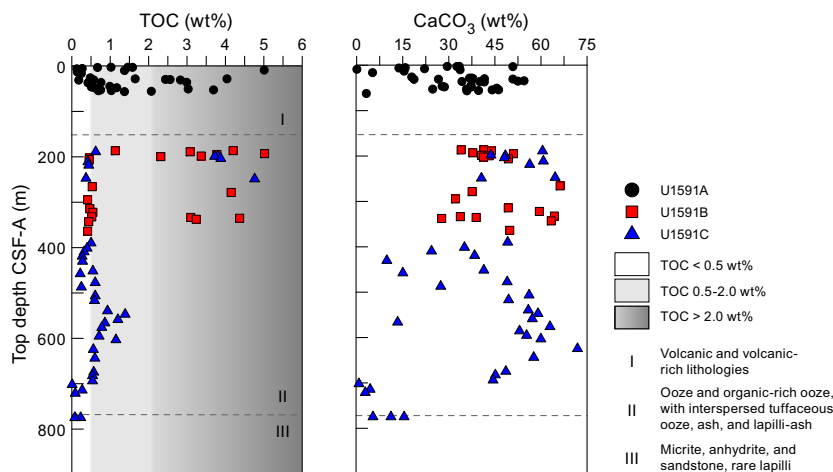
Figure F51. TOC and carbonate, Site U1591. Dashed lines = unit boundaries. Sapropel conventions follow Kidd et al. (1978).

carbonate content at ~400–500 mbsf, which corresponds to higher amounts of volcanic or tuffaceous lithologies in that unit. In Unit III, which is characterized by evaporites, three samples were collected to identify the total organic carbon (TOC) content of mud and possible interaction with the evaporites. The mud layer was sampled at 774.75 mbsf and has two adjacent evaporite units, one light and one dark, at 774.79 and 774.82 mbsf, respectively. The TOC value for the mud unit is 0.23 wt%, and both evaporite units have TOC values of 0.08 wt%.

9.3.1. Sapropel identification

A total of 44 organic-rich units of interest were sampled after core splitting. Because of the lithified nature of cores deeper than ~400 mbsf, limited sampling was realized on board, although more organic-rich units were identified by the core describers (see **Lithostratigraphy**). TOC was calculated using total carbon and inorganic carbon values. Following the convention set forth by Kidd et al. (1978), units with TOC > 2.0 wt% were identified as sapropels and units with TOC values of 0.5–2.0 wt% were identified as sapropelitic. Using these values, 22 units were identified as sapropels and 37 units were identified as sapropelitic (Figure **F51**).

9.4. Headspace gas analysis

Headspace gas analyses were performed at a resolution of one sample per full-length core (9.5 m advance) or one sample every other core for half-length cores (4.7 m advance) throughout Hole U1591A. The aim was to monitor the presence and abundance of C_1–C_3 hydrocarbons as part of the standard IODP safety protocol (Pimmel and Claypool, 2001). A total of 10 headspace gas samples were analyzed using gas chromatography (GC) (see **Geochemistry** in the Expedition 398 methods chapter [Kutterolf et al., 2024]). Methane was the dominant hydrocarbon present at low concentrations or concentrations below the detection limit in Hole U1591A (Figure **F52**). Ethane, propane, butane, and other heavier hydrocarbons were either present in low concentrations or below the detection limit.

Headspace gas analyses were resumed on Hole U1591B when coring progressed deeper than Hole U1591A (100.3 mbsf). Below this depth, headspace gas analyses were performed at a resolution of one sample per core or one sample every other core for half-length cores to the base of the hole. A total of 26 headspace gas samples were analyzed using GC. No elevated methane concentrations were noted in the core except a concentration of 51.8 ppmv at 385.82 mbsf (Figure **F52**).

Headspace gas analyses were resumed on Hole U1591C when coring progressed deeper than Hole U1591B (389.9 mbsf). Below this depth, 53 headspace gas analyses were performed at a resolution of one sample per core to the base of the hole. Methane values were low to 559 mbsf and then gradually increased to 612 mbsf, where the maximum value of 883 ppmv was reached. Below this depth, methane values decreased to 868 mbsf, below which depth values again increased to 168 ppmv. Ethane concentrations are low or below the detection limit except in intervals with elevated methane concentrations. The highest ethane concentration observed was 9 ppmv at 660 mbsf (Figure **F52**).
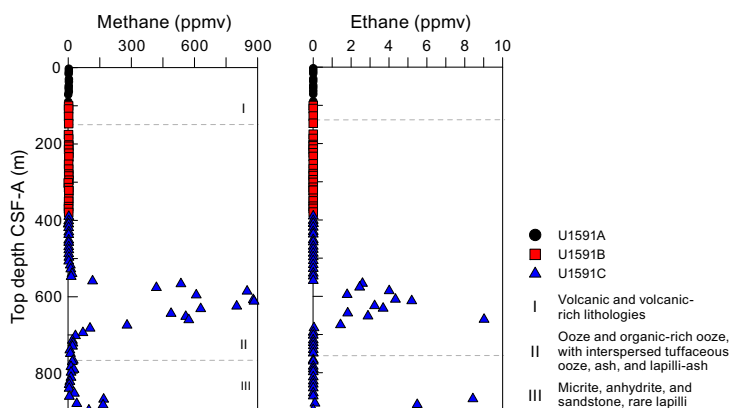
Figure F52. Headspace gas analyses of methane, Site U1591. Dashed lines = unit boundaries.

Table T19. Microbiology samples, Site U1591. **Download table in CSV format.**

10. Microbiology

For Site U1591, two whole-round core samples were collected for microbial community composition analysis (Table **T19**).

References

Aarburg, S., and Frechen, M., 1999. Die pyroklastischen Abfolgen der Christiana-lnseln (Süd-Ägäis, Griechenland). In Becker-Haumann, R., and Frechen, M. (Eds.) Terrestrische Quartargeologie. 260–276.

Abu-Zied, R.H., Rohling, E.J., Jorissen, F.J., Fontanier, C., Casford, J.S.L., and Cooke, S., 2008. Benthic foraminiferal response to changes in bottom-water oxygenation and organic carbon flux in the eastern Mediterranean during LGM to Recent times. Marine Micropaleontology, 67(1–2):46–68. **https://doi.org/10.1016/j.marmicro.2007.08.006**

Backman, J., Raffi, I., Rio, D., Fornaciari, E., and Pälike, H., 2012. Biozonation and biochronology of Miocene through Pleistocene calcareous nannofossils from low and middle latitudes. Newsletters on Stratigraphy, 45(3):221–244. **https://doi.org/10.1127/0078-0421/2012/0022**

Brothers, R.J., Kemp, A.E.S., and Maltman, A.J., 1996. Mechanical development of vein structures due to the passage of earthquake waves through poorly-consolidated sediments. Tectonophysics, 260(4):227–244. **https://doi.org/10.1016/0040-1951(96)00088-1**

Di Stefano, A., and Sturiale, G., 2010. Refinements of calcareous nannofossil biostratigraphy at the Miocene/Pliocene Boundary in the Mediterranean region. Geobios, 43(1):5–20. **https://doi.org/10.1016/j.geobios.2009.06.007**

Druitt, T., Kutterolf, S., and Höfig, T.W., 2022. Expedition 398 Scientific Prospectus: Hellenic Arc Volcanic Field. International Ocean Discovery Program. https://doi.org/10.14379/iodp.sp.398.2022

Druitt, T.H., Kutterolf, S., Ronge, T.A., Beethe, S., Bernard, A., Berthod, C., Chen, H., Chiyonobu, S., Clark, A., DeBari, S., Fernandez Perez, T.I., Gertisser, R., Hübscher, C., Johnston, R.M., Jones, C., Joshi, K.B., Kletetschka, G., Kouk-ousioura, O., Li, X., Manga, M., McCanta, M., McIntosh, I., Morris, A., Nomikou, P., Pank, K., Peccia, A., Poly-menakou, P.N., Preine, J., Tominaga, M., Woodhouse, A., and Yamamoto, Y., 2024. Site U1589. In Druitt, T.H., Kutterolf, S., Ronge, T.A., and the Expedition 398 Scientists, Hellenic Arc Volcanic Field. Proceedings of the International Ocean Discovery Program, 398: College Station, TX (International Ocean Discovery Program). **https://doi.org/10.14379/iodp.proc.398.103.2024**

Expedition 334 Scientists, 2012. Expedition 334 summary. In Vannucchi, P., Ujiie, K., Stroncik, N., and the Expedition 334 Scientists, Proceedings of the Integrated Ocean Drilling Program. 334: Tokyo (Integrated Ocean Drilling Program Management International, Inc.). **https://doi.org/10.2204/iodp.proc.334.101.2012**

Fisher, R.V., and Schmincke, H.-U., 1984. Pyroclastic Rocks: Berlin (Springer). **https://doi.org/10.1007/978-3-642-74864-6**

Gradstein, F.M., Ogg, J.G., Schmitz, M.D., and Ogg, G.M. (Eds.), 2020. The Geologic Time Scale 2020: Amsterdam (Elsevier BV). **https://doi.org/10.1016/C2020-1-02369-3**

Hanamura, Y., and Ogawa, Y., 1993. Layer-parallel faults, duplexes, imbricate thrusts and vein structures of the Miura Group: keys to understanding the Izu fore-arc sediment accretion to the Honshu fore arc. Island Arc, 2(3):126–141. **https://doi.org/10.1111/j.1440-1738.1993.tb00081.x**

Hayward, B.W., Grenfell, H.R., Reid, C.M., and Hayward, K.A., 1999. Recent New Zealand shallow-water benthic fora-minifera: taxonomy, ecologic distribution, biogeography, and use in paleoenvironmental assessment. In Institute of Geological & Nuclear Sciences Monograph, 21: Lower Hutt, NZ.

Jelínek, V., and Kropáček, V., 1978. Statistical processing of anisotropy of magnetic susceptibility measured on groups of specimens. Studia Geophysica et Geodaetica, 22(1):50–62. **https://doi.org/10.1007/BF01613632**

Jutzeler, M., White, J.D.L., Talling, P.J., McCanta, M., Morgan, S., Le Friant, A., and Ishizuka, O., 2014. Coring distur-bances in IODP piston cores with implications for offshore record of volcanic events and the Missoula megafloods. Geochemistry, Geophysics, Geosystems, 15(9):3572–3590. **https://doi.org/10.1002/2014GC005447**

Keller, J., Dietrich, V., Reusser, E., Gertisser, R., and Aarburg, S., 2010. Recognition of a major ignimbrite in the early evolution of the Santorini Group: the Christiani ignimbrite. Presented at the Cities on Volcanoes Conference, Tenerife, Spain, January 2010.

Kidd, R.B., Cita, M.B., and Ryan, W.B.F., 1978. Stratigraphy of eastern Mediterranean sapropel sequences recovered during DSDP Leg 42A and their paleoenvironmental significance. In Hsü, K., Montadert, L., et al., Initial Reports of the Deep Sea Drilling Project. 42(1): Washington, DC (US Government Printing Office), 421–443. **https://doi.org/10.2973/dsdp.proc.42-1.113-1.1978**

Kletetschka, G., and Wieczorek, M.A., 2017. Fundamental relations of mineral specific magnetic carriers for paleointensity determination. Physics of the Earth and Planetary Interiors, 272:44–49. **https://doi.org/10.1016/j.pepi.2017.09.008**

Krijgsman, W., Hilgen, F.J., Meijer, P.T. and Briand, F., 2007. Chronological constraints and consequences for the Mes-sinian Salinity Crisis. In CIESM, The Messinian Salinity Crisis from Mega-deposits to Microbiology - a Consensus Report: Almeria, 7–10 November 2007. CIESM Workshop Monographs, 33.

Kutterolf, S., Druitt, T.H., Ronge, T.A., Beethe, S., Bernard, A., Berthod, C., Chen, H., Chiyonobu, S., Clark, A., DeBari, S., Fernandez Perez, T.I., Gertisser, R., Hübscher, C., Johnston, R.M., Jones, C., Joshi, K.B., Kletetschka, G., Koukousioura, O., Li, X., Manga, M., McCanta, M., McIntosh, I., Morris, A., Nomikou, P., Pank, K., Peccia, A., Polymenakou, P.N., Preine, J., Tominaga, M., Woodhouse, A., and Yamamoto, Y., 2024. Expedition 398 methods. In Druitt, T.H., Kutterolf, S., Ronge, T.A., and the Expedition 398 Scientists, Hellenic Arc Volcanic Field. Proceedings of the International Ocean Discovery Program, 398: College Station, TX (International Ocean Discovery Program). **https://doi.org/10.14379/iodp.proc.398.102.2024**

Kutterolf, S., Freundt, A., Hansteen, T.H., Dettbarn, R., Hampel, F., Sievers, C., Wittig, C., Allen, S.R., Druitt, T.H., McPhie, J., Nomikou, P., Pank, K., Schindlbeck-Belo, J.C., Wang, K.-L., Lee, H.-Y., and Friedrichs, B., 2021. The medial offshore record of explosive volcanism along the central to eastern Aegean Volcanic Arc: 1. tephrostratigraphic correlations. Geochemistry, Geophysics, Geosystems, 22(12):e2021GC010010. **https://doi.org/10.1029/2021GC010010**

Le Maitre, R.W., Steckeisen, A., Zanettin, B., Le Bas, M.J., Bonin, B., and Bateman, P. (Eds.), 2002. Igneous Rocks: A Classification and Glossary of Terms (Second edition): Cambridge, UK (Cambridge University Press). **https://doi.org/10.1017/CBO9780511535581**

Lirer, F., Foresi, L.M., Iaccarino, S.M., Salvatorini, G., Turco, E., Cosentino, C., Sierro, F.J., and Caruso, A., 2019. Mediterranean Neogene planktonic foraminifer biozonation and biochronology. Earth-Science Reviews, 196:102869. **https://doi.org/10.1016/j.earscirev.2019.05.013**

Lourens, L., Hilgen, F., Shackleton, N.J., Laskar, J., and Wilson, D., 2004. The Neogene period. In Smith, A.G., Gradstein, F.M. and Ogg, J.G., A Geologic Time Scale 2004. Cambridge, UK (Cambridge University Press), 409–440. **https://doi.org/10.1017/CBO9780511536045.022**

Lourens, L.J., Hilgen, F.J., and Raffi, I., 1998. Base of large Gephyrocapsa and astronomical calibration of early Pleistocene sapropels in Site 967 and Hole 969D: solving the chronology of the Vrica Section (Calabria, Italy). In Robertson, A.H.F., Emeis, K.-C., Richter, C., and Camerlenghi, A. (Eds.), Proceedings of the Ocean Drilling Program, Scientific Results. 160: College Station, TX (Ocean Drilling Program), 191. **https://doi.org/10.2973/odp.proc.sr.160.017.1998**

Maltman, A.J., Byrne, T., Karig, D.E., and Lallemant, S., 1993. Deformation at the toe of an active accretionary prism: synopsis of results from ODP Leg 131, Nankai, SW Japan. Journal of Structural Geology, 15(8):949–964. **https://doi.org/10.1016/0191-8141(93)90169-B**

Martini, E., 1971. Standard Tertiary and Quaternary calcareous nannoplankton zonation. Proceedings of the Second Planktonic Conference, Roma, 1970:739–785.

Okada, H., and Bukry, D., 1980. Supplementary modification and introduction of code numbers to the low-latitude coccolith biostratigraphic zonation (Bukry, 1973; 1975). Marine Micropaleontology, 5(3):321–325. **https://doi.org/10.1016/0377-8398(80)90016-X**

Pimmel, A., and Claypool, G., 2001. Introduction to shipboard organic geochemistry on the JOIDES Resolution. Ocean Drilling Program Technical Note, 30. **https://doi.org/10.2973/odp.tn.30.2001**

Preine, J., Karstens, J., Hübscher, C., Crutchley, G.J., Druitt, T.H., Schmid, F., and Nomikou, P., 2022a. The hidden giant: how a rift pulse triggered a cascade of sector collapses and voluminous secondary mass-transport events in the early evolution of Santorini. Basin Research, 34(4):1465–1485. **https://doi.org/10.1111/bre.12667**

Preine, J., Karstens, J., Hübscher, C., Nomikou, P., Schmid, F., Crutchley, G.J., Druitt, T.H., and Papanikolaou, D., 2022b. Spatio-temporal evolution of the Christiana-Santorini-Kolumbo volcanic field, Aegean Sea. Geology, 50(1):96–100. **https://doi.org/10.1130/G49167.1**

Rio, D., Raffi, I., and Villa, G., 1990. Pliocene-Pleistocene calcareous nannofossil distribution patterns in the western Mediterranean. In Kastens, K.A., Mascle, J., et al., Proceedings of the Ocean Drilling Program, Scientific Results. 107: College Station, TX (Ocean Drilling Program), 513–533. **https://doi.org/10.2973/odp.proc.sr.107.164.1990**

Schacht, U., Wallmann, K., Kutterolf, S., and Schmidt, M., 2008. Volcanogenic sediment–seawater interactions and the geochemistry of pore waters. Chemical Geology, 249(3):321–338. **https://doi.org/10.1016/j.chemgeo.2008.01.026**

Shipboard Scientific Party, 2001. Leg 190 summary. In Moore, G.F., Taira, A., Klaus, A., et al., Proceedings of the Ocean Drilling Program, Initial Reports, 190. College Station, TX (Ocean Drilling Program), 1–87. **https://doi.org/10.2973/odp.proc.ir.190.101.2001**

Tarling, D.H., 1983. Paleomagnetism: Principles and Applications in Geology, Geophysics and Archaeology: Dordrecht, Netherlands (Springer). **https://doi.org/10.1007/978-94-009-5955-2**

Tsampouraki-Kraounaki, K., and Sakellariou, D., 2018. Seismic stratigraphy and geodynamic evolution of Christiana Basin, South Aegean Arc. Marine Geology, 399:135–147. **https://doi.org/10.1016/j.margeo.2018.02.012**

Wallace, L.M., Saffer, D.M., Barnes, P.M., Pecher, I.A., Petronotis, K.E., LeVay, L.J., Bell, R.E., Crundwell, M.P., Engelmann de Oliveira, C.H., Fagereng, A., Fulton, P.M., Greve, A., Harris, R.N., Hashimoto, Y., Hüpers, A., Ikari, M.J., Ito, Y., Kitajima, H., Kutterolf, S., Lee, H., Li, X., Luo, M., Malie, P.R., Meneghini, F., Morgan, J.K., Noda, A., Rabinowitz, H.S., Savage, H.M., Shepherd, C.L., Shreedharan, S., Solomon, E.A., Underwood, M.B., Wang, M., Woodhouse, A.D., Bourlange, S.M., Brunet, M.M.Y., Cardona, S., Clennell, M.B., Cook, A.E., Dugan, B., Elger, J., Gamboa, D., Georgiopoulou, A., Han, S., Heeschen, K.U., Hu, G., Kim, G.Y., Koge, H., Machado, K.S., McNamara, D.D., Moore, G.F., Mountjoy, J.J., Nole, M.A., Owari, S., Paganoni, M., Rose, P.S., Screaton, E.J., Shankar, U., Torres, M.E., Wang, X., and Wu, H.-Y., 2019. Expedition 372B/375 methods. In Wallace, L.M., Saffer, D.M., Barnes, P.M., Pecher, I.A., Petronotis, K.E., LeVay, L.J., and the Expedition 372/375 Scientists, Hikurangi Subduction Margin Coring, Logging, and Observatories. Proceedings of the International Ocean Discovery Program, 372B/375: College Station, TX (International Ocean Discovery Program). **https://doi.org/10.14379/iodp.proc.372B375.102.2019**